

合縫與中穿通途徑對齒狀迴中間神經元之特異性活化  
Differential Recruitment of Dentate Gyrus Interneuron Types by  
Commissural Versus Perforant Pathways

研究生：許臻庭 (Tsan-Ting Hsu)

指導教授：連正章 博士 (Cheng-Chang Lien, M.D., Ph.D.)

孫興祥 博士 (Synthia H. Sun, Ph.D.)

國立陽明大學

神經科學研究所

博士論文

Institute of Neuroscience

National Yang-Ming University

Doctoral Dissertation

中華民國一〇四年七月

July, 2015

合縫與中穿通途徑對齒狀迴中間神經元之特異性活化  
Differential Recruitment of Dentate Gyrus Interneuron Types by  
Commissural Versus Perforant Pathways

研究生：許臻庭 (Tsan-Ting Hsu)

指導教授：連正章 博士 (Cheng-Chang Lien, M.D., Ph.D.)

孫興祥 博士 (Synthia H. Sun, Ph.D.)



國立陽明大學

神經科學研究所

博士論文

Institute of Neuroscience

National Yang-Ming University

Doctoral Dissertation

中華民國一〇四年七月

July, 2015

# 國立陽明大學博士學位論文審定同意書

神經科學 研究所 許璨庭 君 (學號：39501005)

所提之論文

題目：(中文)

合縫與中穿通途徑對齒狀迴中間神經元之特異性活化

(英文)

Differential Recruitment of Dentate Gyrus Interneuron  
Types by Commissural Versus Perforant Pathways

經學位考試委員會審查通過，特此證明。

學位考試委員會 (簽名)

召集人

焦傳金

口試委員

焦傳金

林惠菁

戴月娥

連正章

周明祥

林貝容

孫興祥

陳柏文

陳右毅

論文已修改完成

指導教授

連正章

孫興祥

(簽名)

所長

神經科學  
研究所所長郭文瑞

(簽名)

中華民國 104 年 7 月 21 日

## 國立陽明大學學位論文電子檔授權書

本授權書所授權之學位論文全文電子檔，為本人於國立陽明大學神經科學研究所 甲 組，103 學年度第 二 學期取得博士學位之論文。

論文題目：合縫與中穿通途徑對齒狀迴中間神經元之特異性活化  
指導教授：連正章,孫興祥

### ■ 同意

本人茲將本著作，以非專屬、無償授權國立陽明大學與台灣聯合大學系統圖書館：基於推動讀者間「資源共享、互惠合作」之理念，及回饋社會與學術研究之目的，國立陽明大學及台灣聯合大學系統圖書館得不限地域、時間與次數，以紙本、光碟或數位化等各種方法收錄、重製與利用；於著作權法合理使用範圍內，讀者得進行線上檢索、閱讀、下載或列印。

論文全文電子檔之公開網域範圍及時間：

校內區域網路	■ 立即公開
台灣聯合大學網際網路	■ 中華民國 105 年 7 月 20 日公開
校外網際網路	■ 中華民國 105 年 7 月 20 日公開

### ■ 同意全文電子檔送交國家圖書館

授權人：許璨庭

親筆簽名： 許璨庭

指導教授簽名： 連正章 孫興祥

中華民國 104 年 7 月 21 日

## 致謝

終於完成了論文，即將畢業離開這個待了九年的陽明。這真是一段”轉大人”的過程，不管是工作，生活還是興趣，往後一輩子生活的一切，都在這段時期奠定了基礎。首先，我要感謝我的指導教授-連正章老師, 孫興祥老師以及中山大學的戴明泓老師。連正章老師引領我進入神經電生理的研究領域，且在我的研究上不遺餘力的指導，才能使論文能順利被期刊接受。孫興祥老師是我神經科學的啟蒙老師，在一開始碩士班階段總是不遺餘力的給我們最好的研究資源，生活上也受到諸多的照顧。在戴明泓老師實驗室的日子，是我博士班生涯從低谷爬起來的階段，感謝戴老師的指導與照顧。另外也要感謝李政欣博士提供腺相關病毒製作方法與材料，讓我的研究可以順利的發展起來。再來要感謝口試委員焦傳金老師，閔明源老師，陳右穎老師，林惠菁老師，陳摘文老師與林貝容老師對論文的指正與建議，讓這份論文更加完備。

在陽明生活了九年，遇到了許多人，經歷了許多的事情。感謝一起進來神研所的同窗，在開始的兩年有許多回憶。感謝不同階段的實驗室大夥，一開始在孫老師家的成員，後來連老師家的成員，以及到中山大學戴老師家的成員，謝謝你們和我一起度過實驗室生活，在實驗以及生活上互相幫忙，希望還留在實驗室打拼的夥伴們都能快點有好的成果可以畢業。還要感謝在校園裡的眾多貓狗們，尤其是大母貓，小黃以及他們不幸或幸運的小孩，從沒想過自己會有這麼一段經歷，為了改變你們的命運而勞心勞力。會懷念每次拖著疲憊身體回到宿舍時，看到你們跑過來在腳邊打轉的場景，希望你們都可以平靜快樂的度過一輩子。

僅以此論獻給我摯愛的家人，爸媽總是無條件的付出與關心，讓我在生活上過的很好，我終於可以畢業，你們的擔心可以放下了。還有哥哥一家人以及妹妹，這份畢業的喜悅與你們共享。最後要感謝韋均，在過去這幾年一直有妳的陪伴，我們一起經歷了許多難熬的日子，沒有妳，我不可能順利完成學業，未來我們還要一起度過，过上我們期望的生活。



許璨庭 謹致於

國立陽明大學神經科學研究所

中華民國一百零四年七月

## 中文摘要

在海馬齒狀迴中， $\gamma$ -氨基丁酸生成中間神經元可抑制性調控顆粒細胞活性，故可作為海馬迴訊息輸入之控管閘門。然而不同種類之中間神經元如何對興奮性輸入途徑產生反應，對顆粒細胞活性調控又有何差異；諸如此類細節，皆有待釐清。本研究以電生理與光遺傳學技術探索活體鼠腦切片門區合縫途徑 (hilar commissural pathway) 以及中穿通途徑 (medial perforant pathway) 至齒狀迴之神經突觸傳導。我們發現：若以 theta 頻率 (10 Hz) 連續刺激個別輸入途徑，則此二途徑將對顆粒細胞興奮性突觸產生相似之傳導動態，然而兩者引發之抑制性突觸傳導動態卻大不相同。合縫途徑活化將使顆粒細胞抑制性突觸傳導相對於興奮性突觸傳導之比例上升，而中穿通途徑活化則導致相反結果。深入分析各種中間神經元對輸入途徑的專一性反應後，我們發現：籃狀中間神經元，全分子層中間神經元以及分子層中間神經元接收之門區合縫途徑興奮性輸入傳導強於來自中穿通途徑之興奮性傳導，而門區合縫途徑對這幾類中間神經元的徵召也較為穩定可靠。相對的，門區穿通途徑相關以及門區合縫-聯合途徑相關中間神經元鮮少被這兩條輸入途徑活化。研究結果證實不同來源之齒狀迴輸入途徑將徵召不同種類之中間神經元，並闡明這些中間神經元於門區合縫途徑前饋抑制之相對貢獻。

## Abstract

Gamma-aminobutyric acidergic (GABAergic) interneurons (INs) in the dentate gyrus (DG) provide inhibitory control to granule cell (GC) activity and thus gate incoming signals to the hippocampus. However, how various IN subtypes inhibit GCs in response to different excitatory input pathways remains mostly unknown. By using electrophysiology and optogenetics, we investigated neurotransmission of the hilar commissural pathway (COM) and the medial perforant path (MPP) to the DG in acutely prepared mouse slices. We found that the short-term dynamics of excitatory COM–GC and MPP–GC synapses was similar, but that the dynamics of COM- and MPP-mediated inhibition measured in GCs was remarkably different, during theta-frequency stimulation. This resulted in the increased inhibition–excitation (I/E) ratios in single GCs for COM stimulation, but decreased I/E ratios for MPP stimulation. Further analysis of pathway-specific responses in identified INs revealed that basket cell-like INs, total molecular layer- and molecular layer-like cells, received greater excitation and were more reliably recruited by the COM than by the MPP inputs. In contrast, hilar perforant path-associated and hilar commissural–associational pathway-related-like cells were minimally activated by both inputs. These results demonstrate that distinct IN subtypes are preferentially recruited by different inputs to the DG, and reveal their relative contributions in COM-mediated feedforward inhibition.



# Table of Contents

致謝 .....	i
中文摘要 .....	iii
Abstract .....	iv
Table of Contents .....	v
Abbreviations .....	viii
Introduction .....	1
Hippocampal Formation: the Memory-Forming Unit and Spatial Map in the Brain .....	1
Dentate Gyrus as the Primary Gate of Hippocampus .....	4
PP-Driven Inhibitory Control of GC .....	6
Hilar Commissural Projection from Mossy Cells .....	7
Optogenetics .....	9
Aim of this study .....	11
Materials and Methods .....	12
Animals .....	12
Plasmid Construct for ChR2 Expression and Functional Examination .....	12
AAV Generation .....	13
Stereotaxic Injection .....	16
Optical fiber implantation .....	17
Preparation of Brain Slices .....	18
Slice Electrophysiology and Optical Stimulation .....	18
Immunohistochemistry .....	19
Chemicals and Drugs .....	21

Contextual Fear Conditioning and in vivo Photostimulation.....	21
Data Analysis and Statistics.....	22
<b>Results.....</b>	<b>24</b>
Generation of AAV for cell type-specific targeting of ChR2.....	24
Selective ChR2 Expression in the COM or MPP.....	26
GCs Receive More Inhibition Than Excitation From the COM.....	28
Comparison of COM- and MPP-mediated EPSCs Across Various IN Type.....	30
TML- and ML-Like Cells Were Preferentially Recruited by the COM.....	33
Regulation of MPP Input Efficacy by COM Activation.....	34
Enhancement of contextual fear memory by COM activation.....	35
<b>Discussion.....</b>	<b>37</b>
Summary.....	37
Drawbacks of Optogenetics in Studying Synaptic Transmission.....	37
Correlations between IN Recruitment and the Dynamics of IN-GC Synaptic Transmission	38
IN Diversity.....	39
Pathway-Specific Recruitment of IN Types.....	40
Limitations of COM Targeting in the Present Study.....	41
Discussion on the Functional Role of COM in Cognitive Level.....	42
<b>References.....</b>	<b>44</b>
<b>Figures and Tables.....</b>	<b>55</b>
Figure 1.....	55
Figure 2.....	57
Figure 3.....	59
Figure 4.....	60

Figure 5.....	62
Figure 6.....	63
Figure 7.....	64
Figure 8.....	65
Figure 9.....	66
Figure 10.....	67
Figure 11.....	68
Figure 12.....	69
Figure 13.....	70
Figure 14.....	71
Figure 15.....	72
Figure 16.....	73
Figure 17.....	74
Figure 18.....	75
Figure 19.....	76
Figure 20.....	77
Figure 21.....	78
Figure 22.....	80
Figure 23.....	82
Figure 24.....	83
Figure 25.....	84
Figure 26.....	85
Figure 27.....	86
Table1.....	87
Table2.....	88
Curriculum Vitae.....	89



## Abbreviations

AAV: adeno-associated virus

AAV5: AAV serotype 5

AMPA:  $\alpha$ -amino-3-hydroxy-5-methyl-4-isoxazolepropionic acid

BC: basket cell

ChR2: channelrhodopsin-2

CNQX: 6-cyano-7-nitroquinoxaline-2,3-dione

COM: commissural pathway

Cre: Cre recombinase

CT: threshold cycle

DG: dentate gyrus

EPSC: excitatory postsynaptic current

eYFP: enhanced yellow fluorescent protein

GABA:  $\gamma$ -aminobutyric acid

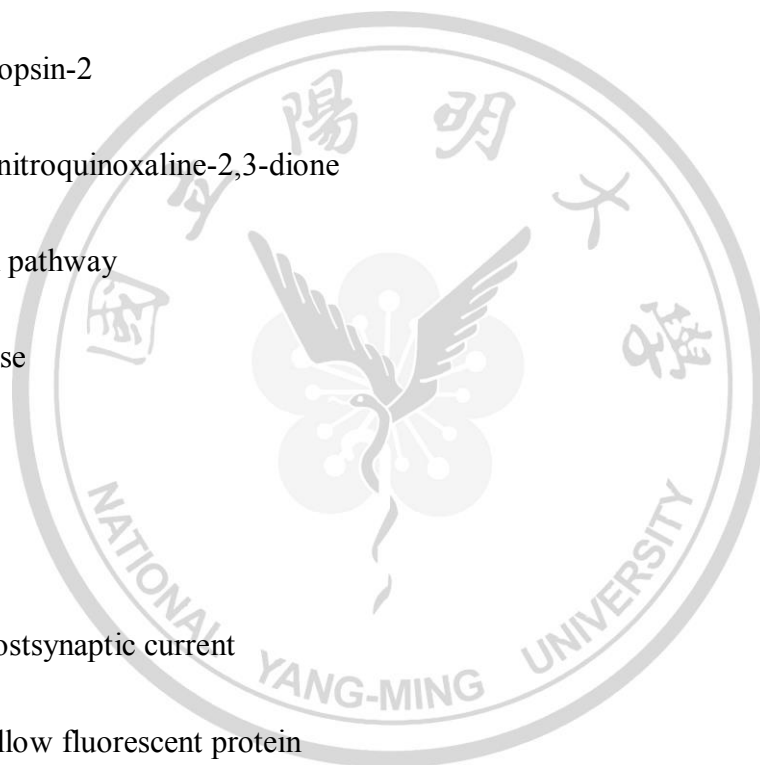
GC: granule cell

GCL: GC layer

HICAP: hilar commissural–associational pathway-related

HIPP: hilar PP-associated

IML: inner one-third molecular layer



IN: interneuron

IPSC: inhibitory postsynaptic current

ITI: inter-trial interval

LTP: long-term potentiation

LV: lentivirus

MC: mossy cell

MEC: medial entorhinal cortex

ML: molecular layer

MML: medial one-third molecular layer

MPP: medial PP

NMDAR: N-methyl-D-aspartate receptor

NP-40: octyl-1-phenoxyethoxyethanol

NpHR: halorhodopsin originated from *Natronomonas pharaonis*

OML: outer one-third molecular layer

PCR: polymerase chain reaction

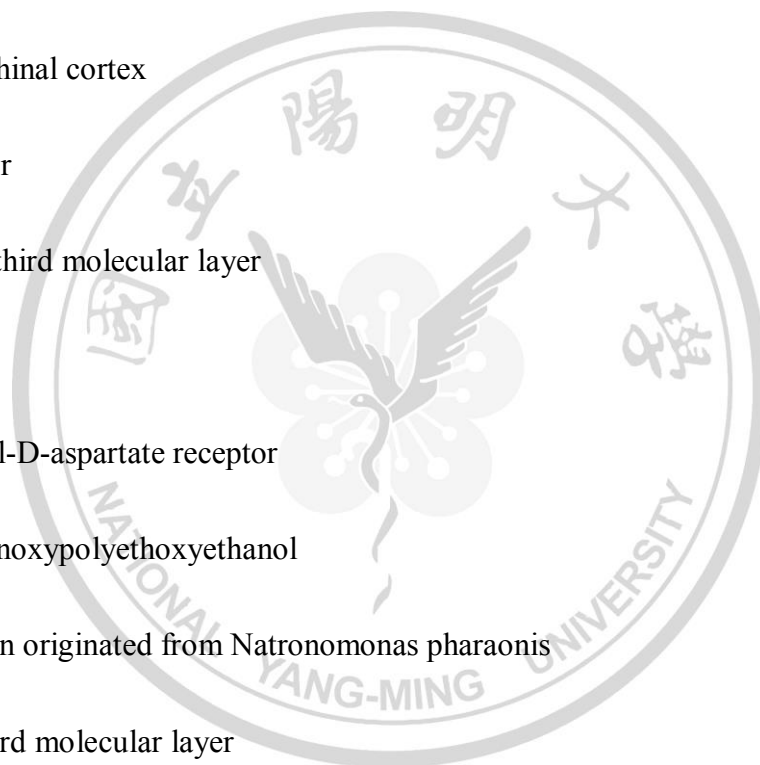
PN: principal neuron

PP: perforant path

pSpike: population spike

SEM: standard error of mean

SuM: supramammillary nucleus



TLE: temporal lobe epilepsy

TML: total molecular layer

TTX: tetrodotoxin citrate



## **Introduction**

### **Hippocampal Formation: the Memory-Forming Unit and Spatial Map in the Brain**

The hippocampus is a brain structure deeply hidden in the temporal lobe. Anatomically, it can be divided into two parts: Dentate gyrus, and the hippocampal proper. The hippocampus extends bilaterally along the septal-temporal axis from rostral septal nuclei to the caudal temporal lobe. The name “hippocampus” was originally inspired by the long, curved appearance of this brain structure, which resembles a seahorse (In Greek: ἵππος hippos means "horses" and κάμπος kampos means "sea monsters"). The hippocampus is intricately interconnected with surrounding areas such as presubiculum, parasubiculum and entorhinal cortex, forming the compound structure “hippocampal formation”. Two major discoveries in the 20th century has enlightened neuroscientists about the functions and importance of hippocampal formation. In 1957, Scoville and Milner reported the severe memory deficit after bilateral medial temporal lobe resection of a patient H.M., who suffered from frequent generalized seizures that were not controlled by antiepileptic drug treatment. The neural surgery, in which bilateral anterior two-thirds of the hippocampus and the surrounding areas (amygdaloid and entorhinal cortex) were removed, was intended to cut off the circuit causing excessive neuronal discharge. However, H.M. exhibited partial retrograde amnesia and severe permanent anterograde amnesia after the surgery, without evidence of other cognitive deficits like perceptual defect, personality change or general intelligence decline (Scoville and Milner 1957). More clinical case studies surfaced after this historic disclosure, reporting that patients with ischemic injuries restricted to the hippocampus also had mild anterograde memory deficit (Zola-Morgan et al. 1986). Hippocampal formation has since been recognized as the key player in memory formation, and elicited intense interests on memory research in the neuroscience society.

Another important finding is the discovery of inner spatial navigating system in the hippocampal formation. In 1971, John O'Keefe discovered the "place cells" in the hippocampus. He recorded the spiking activities of individual hippocampal neurons while the rat explored a room. He found that when the animal was in a particular position of the room, certain neuron was activated, while the others were kept silent. The experiment indicated that different place cells in hippocampus encode different location of the room, thereby forming the internal representation of the absolute spacial coordinate of a particular environment (O'Keefe and Dostrovsky 1971). Intuitively, however, the ability to encode the absolute location of the environment may not be sufficient enough for efficient spatial navigation. Other information, such as the relative spatial orientation and distance between two locations, awareness of large landmarks and the heading directions, is also important. In fact, other modalities associated with spatial information could also be encoded by neurons in the hippocampal formation. More than thirty years after the discovery of place cell, May-Britt and Edvard Moser' group discovered other types of spatial information encoding cells. They recorded the neurons in the medial entorhinal cortex (MEC) while the animal was exploring a space. They found several cell types encoding spatial information. The first characterized cell type is "grid cell", which has firing activities whenever the animal's position coincides with the vertex of a periodic hexagonal grid across the entire space. The grid-like structure of firing field resembles the longitude and latitude of a map, providing the coordinate system for mapping the distance between different locations (Hafting et al., 2005). The second one is "border cell," which is activated when the animal approaches specific physical boundaries in the environment. The firing field of border cell parallels the border of physical boundaries, thereby encoding the vicinity to boundaries (Solstad et al. 2008). Finally, there is a spatial encoding cell type named "head-direction cell", which was first discovered in the postsubiculum (Taube et al. 1990) and later in many areas as well as the MEC (Sargolini et al. 2006). Head-direction cells are fired only when the animal is facing a particular direction, regardless of the animal's position in the space. Different head-direction cells work together to



provide the directional reference frame during navigation through the field. There may still be more cell types in MEC that encode spatial information with unidentified domain features (Zhang et al. 2013). To date, how different types of spatial encoding cells coordinate with each other, and whether spatial navigation is correlated with memory function, is still a hot topic in neuroscience research field.

The anatomical and physiological properties of circuits might provide some hints regarding the memory generation and spatial navigation in the hippocampal formation. Brain slices cut perpendicular to the longitudinal axis of hippocampus and surrounding areas reveals the subfields (entorhinal cortex, subiculum, dentate gyrus and hippocampal proper) and the basic unidirectional circuit organization of hippocampal formation (Ramon y Cajal 1911). The entorhinal cortex is considered to be the origin of the circuits, receiving multiple sensory inputs from other brain areas. The neurons in the layer II of entorhinal cortex send axonal projections called perforant path (PP) through the subiculum and target to the dentate gyrus (DG) in the hippocampus. In the next progression of connections, granule cells (GCs), the principal neurons (PNs) in DG project mossy fibers to innervate the proximal dendrites of CA3 PNs in the hippocampal proper. The third synapses in trisynaptic circuits come from the CA3 Schaffer collaterals, which are axonal projections from CA3 PN and target at the dendrites of CA1 PNs. CA1 PNs are the output neurons of hippocampus, send their axons to subiculum, and deep layers of entorhinal cortex. Therefore, the connections between CA1/subiculum and entorhinal cortex close the circuit loop that starts from the layer II of entorhinal cortex. Among the trisynaptic circuits within hippocampus, PP–DG, DG–CA3 and CA3–CA1 synapses are all reported to have activity-dependent synaptic plasticities, which are considered to be necessary for memory formation (Bliss and Lomo 1973; Harris and Cotman 1986; Collingridge and Singer 1990). Considering the nearly infinite number of random combinations of all the synaptic strength changing possibilities from all three synaptic relays,

hippocampus suits the function of generating new memories. In addition, different subfields of hippocampal formation are interconnected with each other, indicating that geographically separated spatial encoding cells with different modalities might cooperate in a conjunctive way to execute spatial navigating function. In fact, almost all the functionally identified cell types involving spatial navigation (grid cells, border cells, head-direction cells and unknown spatial-encoding cells) in the superficial layers of MEC could send their axons to hippocampus (Zhang et al. 2013).

### **Dentate Gyrus as the Primary Gate of Hippocampus**

As a memory-forming unit, it is necessary to generate distinguishable representations for events with similar features, thus increasing the memory capacity suitable for adapting the ever changing world. Hippocampus has some attributes that meet this requirement. A well-characterized feature of hippocampal place cells is the dramatic change of their firing field or firing rate in response to slight environmental fluctuations encountered by the animal (Muller et al. 1991). The ability to amplify the differences between similar events is called “pattern separation”, and DG is considered to be the first key station for this function among hippocampal circuits. Histologically, DG can be viewed as being composed of three layers of neuronal tissue constituted by polarized principal neuron GCs. GCs have small, round cell bodies that are localized to the GC layer (GCL), and extend their dendrites into molecular layer (ML), where they receive laminated axonal projections from distant sources. Once the GCs are depolarized by excitatory inputs, there is a possibility that GCs can be recruited and propagate action potentials by mossy fibers through the inner layer hilus, which is located on the opposite side of ML. However, GCs fire sparsely both *in vivo* and *ex vivo* compared to the upstream cortical areas (Alme et al. 2010; Pernía-Andrade and Jonas 2014). The sparse firing characteristic of GCs makes DG a suitable gate to transform massive overlapping cortical information into distinct representations. The direct evidence was presented by Leutgeb et al. (2007). They recorded neuronal activities when rats were exploring an environment with stepped,

gradual shape transformations (from the square shape to the round shape or *vice versa*). They found that grid-like firing fields and rates (neuronal activities come from individual grid cells in MEC or local interneuron activities recruited by PP) in the PP-termination area within hippocampus were similar across different levels of transformation. However, place cell-like firing fields recorded from single GCs changed non-coherently with progressive transformation of the environment. Even a small difference of the environmental shape could cause extensive firing field change in the recorded GC. McHugh et al. (2007) provided more insights about how DG contributes to pattern separation during memory encoding. They specifically abolished the plasticity forming on PP-GC synapse by genetic method, while other synapses were left undisturbed. They found that the mutant mice had impairment of discriminating two similar contexts. The experiment suggested that DG participated in rapid discrimination of similar events. In addition to pattern separation, sparse firing characteristic of GCs also serve as the protecting shield to protect hippocampal circuits against runaway excitation (Behr et al. 1998; Coulter and Carlson 2007). This point of view has been demonstrated in many studies. In one experiment, when the upstream circuits of DG are elicited pharmacologically to have epileptiform activities, these rampant activities don't propagate through DG to the downstream hippocampal circuits. However, the DG gating would breakdown during the latent period of temporal lobe epilepsy (TLE) development (Pathak et al. 2007). There were anatomical and physiological alternations of DG, including dispersion of GCs, abnormal GC neurogenesis, the appearance of GCs in ectopic locations, and the hyperexcitability in response to PP stimulation. The transient DG dysfunction would cause over excitation of downstream circuits, and led to the formation of TLE.

Multiple cellular mechanisms are coordinated for sparse activation of GCs. First, GC dendrites act as a strong voltage attenuator. Synaptic input from the entorhinal cortex strongly attenuates along GC dendrites (Schmidt-Hieber et al. 2007; Krueppel et al. 2011). Second, GC

dendrites are a linear integrator. GC dendrites summate synaptic inputs linearly and are not designed for highly efficient synchrony detection (Krueppel et al., 2011). Third, GC dendrites lack mechanisms for dendritic spike generation that allow them to be more efficiently to bring excitatory postsynaptic potentials to AP threshold (Krueppel et al., 2011). Finally, GCs have a more hyperpolarized resting potential relative to other types of neurons (Schmidt-Hieber et al. 2007; Chiang et al. 2012). Beyond the cellular level, circuit mechanisms may contribute to the quiescent nature of GCs.

### **PP-Driven Inhibitory Control of GC**

Cortical information transmission and processing rely on the interplay between synaptic excitation and synaptic inhibition. Synaptic excitation is mainly mediated by glutamatergic neurons, whereas synaptic inhibition is contributed by  $\gamma$ -aminobutyric acidergic (GABAergic) neurons, especially the interneurons (INs) that ramify their axons within a specific regions. GABAergic INs are highly diverse in anatomical, biochemical, and physiological properties. They can form reciprocal local circuits with PNs, and exert multiple functions to shape neuronal activities and synaptic transmissions. In general, there are two forms of IN-mediated actions on PNs. The first one is feedback inhibition. When PNs are recruited by long-range excitatory inputs, PNs make excitatory transmission on INs, and then the INs send the inhibitory transmission back to PNs. The second one is feedforward inhibition. The long-range excitatory inputs diverge onto both PNs and INs. INs can be recruited by certain long-range afferent, and send inhibitory transmissions on PNs. The effects of feedback or feedforward inhibition are diverse, depending on what kind of INs are recruited by a certain excitatory input, in a specific location and timing. In addition, different types of INs extend their axons to target various locations along the somato-dendritic axis of PNs, thereby exerting the inhibitory power on action potential generation, local electrogenesis or synaptic plasticity.

In the DG, synaptic connections is far from forming simple PP–GC synapses. There are various types of GABAergic INs populating the DG, forming local inhibitory circuits with GCs. Several studies indicated that the GABAergic inhibition contribute to sparse activation of GC. Application of GABA<sub>A</sub> receptor antagonists on DG causes hyperexcitability of GCs, and PP stimulation-evoked depolarization seems to propagate through the DG to the downstream CA3 area more easily under this experimental condition (Coulter and Carlson 2007). It had been known that the fast-spiking basket cells (BCs) form perisomatic inhibitory synapses on GCs. During the PP–GC synaptic transmission, medial PP (MPP) makes stronger excitatory connections onto fast-spiking BCs than GCs, ensuring that even smaller MPP inputs generate feedforward inhibition to GCs, thereby contributing to sparse activation of GCs (Ewell and Jones 2010; Dieni et al. 2013; Liu et al. 2014).

However, several important questions remain unanswered with respect to the circuit-driven inhibition. First, there are multiple classes of INs in the DG (Han et al. 1993; Freund and Buzsáki 1996; Mott et al. 1997; Hosp et al. 2014; Liu et al. 2014); apart from soma-targeting BCs, there are at least 4 class of dendrite-targeting INs, including hilar commissural–associational pathway-related (HICAP)-, hilar PP-associated (HIPP)-, total molecular layer (TML)-, and molecular layer (ML)-like cells. Do other IN subtypes contribute to GC input–output transformations in response to PP inputs? Second, In addition to the excitatory projections from entorhinal cortex, DG also receives long-range excitatory afferents from other brain regions (Soriano and Frotscher 1994; Leranth and Hajszan 2007; Boulland et al. 2009; Vivar et al. 2012). How the repertoire of DG INs respond to different excitatory inputs remains unclear.

## **Hilar Commissural Projection from Mossy Cells**

Mossy cell (MC) is another type of glutamatergic neurons in the DG and have distinct properties that separate them from GCs. First, somata of MCs do not form discernible layers, but scatter within the hilus. Second, MCs have specialized spines on the proximal dendrites, called “thorny excrescences”. The name “mossy cell” comes from the appearance that resembles a cell covered in moss. Third, unlike the quiescent nature of GCs, MCs receive long-lasting excitatory synaptic barrages and less synaptic inhibitions. Such excitatory tendency of synaptic transmission, together with its intrinsic membrane properties (long membrane time constant, small afterhyperpolarization and less action potential accommodation), often trigger persistent firing of MC, making MC highly activated and vulnerable to runaway excitation. Finally, the synaptic outputs of MCs are different from GCs. GCs only send mossy fibers to target downstream CA3 PN, as well as hilus neurons (MCs and INs) ipsilaterally in the same transverse axis. However, MCs have more extended axonal projections. In the same transverse axis, MCs primary target aspiny INs within hilus by local axon collaterals. The majority of MC’s axons (> 90% of ipsilateral synaptic connections) project along the longitudinal axis of hippocampus (associational pathway), and innervate the proximal dendrites of GCs within the inner one-third molecular layer (IML; West et al. 1979; Soriano and Frotscher 1994; Buckmaster et al. 1996; Scharfman and Myers 2013). The longitudinal arrangement of associational pathway prevents the formation of feedback excitation loop from MC to GC. In addition to the associational pathway in the ipsilateral DG, MCs also project through commissural pathway (COM) to contralateral DG, targeting at the same laminar layer (that is IML). Since MCs are highly active and send excitatory outputs on GC’s proximal dendrites, it should be hypothesized that MCs elevate spiking activities of GCs. However, at least one kind of innervation coming from MCs exerts the opposite effect. Previous *in vivo* studies showed that COM activation exerts a suppressive effect on concurrent PP-evoked population spikes in the DG through feedforward inhibition (Buzsáki and Czéh 1981; Buzsáki and Eidelberg 1981; Bilkey and Goddard 1987). The COM–PP inputs thus form a control circuit to regulate patterns of information flow. However, a

direct connection of COM afferents to specific inhibitory IN types remains poorly understood. The COM axonal projections substantially overlap with those from the associational axonal projections originated from contralateral MCs, and the axons of local INs. In addition, supramammillary nucleus (SuM) in the posterior hypothalamic region also send axonal projections to the IML (Boulland et al. 2009; Soussi et al. 2010; Kohara et al. 2014). Therefore, it is not possible to differentially activate these pathways with conventional electrical stimulation, and investigate the circuit-driven inhibitions.

## Optogenetics

Brain circuits are extremely complex. Different kind of cells are intermingled, forming the dynamic and sophisticated connections. It is hard to investigate the function of the circuit originating from one type of cells without the influence of others. Nobel laureate Francis Crick said: *“The major challenge facing neuroscience was the need to control one type of cell in the brain while leaving others unaltered.”* (Crick 1979). A novel technique appearing in 2005, termed “optogenetics”, promotes the progress in understanding circuit functions (Boyden et al. 2005). Its name “optogenetics” refers to the combination of optics and genetics to exert selective control of neuronal activities within defined cell types. To achieve this, the single component type 1 opsins encoded by microbial opsin genes are utilized. Component type 1 opsins can sense light and then conduct ions in the same protein, allowing millisecond-scale precision of activity manipulation. The commonly used type 1 opsin for neuronal excitation is channelrhodopsin-2 (ChR2), which is a light-sensitive cationic channel. By expression of ChR2 on neuronal membrane, fast excitation of neuron can be achieved by shining blue light (~470 nm). In contrast, halorhodopsin originating from *Natronomonas pharaonis* (NpHR) is a light-sensitive chloride pump, which transports the chloride into the cells (Zhang et al. 2007). Neurons with NpHR expression can be silenced by illuminating orange light (~590 nm). Therefore, optogenetics permits researchers to conduct temporally precise, cell-type

specific manipulations within the brain circuits. The application of optogenetics is not just simply excitation or inhibition of targeted cells in *ex vivo* experiments; it enables gain or loss of functions, *in vivo* studies of well-defined events in the brain of freely moving animal, which the electrodes and other traditional methods do not allow.

How are the opsin genes delivered and expressed in the specific cell types *in vivo*? Transgenic technology and viral expression system are the two major methods (Zhang et al. 2010). To date, virus expression system is the most popular strategy to delivery opsin genes into the brain, which has several advantages compared with transgenic method. First, gene delivery by virus can achieve higher expression levels when compared with transgenic method, ensuring robust opsin-mediated responses *in vivo*. Second, it is faster to produce an viral transgene cassette designed for specific targeting strategies than transgenic method, which requires multiple time-consuming steps and animal reproduction (Zhang et al. 2010). Finally and the most crucially, when considering the targeting of single circuit with opsins originating from a specific cell type, only viral expression system can achieve good projection targeting (Zhang et al. 2010; Yizhar et al. 2011). Once the cell bodies in one local brain area are transduced by virus, the opsin gene products can traffic down the dendrites and axons, forming light-sensitive projections. This anatomical specificity provided by virus can allow expression of opsins in one brain area and activate the axons in another, thereby providing a good tool to investigate the functional connectivity of targeted circuit. Among the viral expression system, recombinant adeno-associated virus (AAV; Monahan and Samulski, 2000) and lentivirus (LV; Dittgen et al. 2004) are the two most commonly used viral systems. Each of them has its own niches. AAV is considered to be safer than LV because of its low immunity and the absence of integration into the host genome. LV has larger transgene packing capacity (~10 kb maximum) compared with rAAV (~5 kb maximum), enabling more flexible spaces for genetic engineering. Both rAAV and LV have wide range of infectivity, depending on the pseudotyping



techniques with various serotypes (McFarland et al. 2009) and envelope glycoproteins (Kafri 2004), respectively.

### **Aim of this study**

Early *in vivo* studies revealed the net suppressive effect of COM on concurrent perforant pathway-evoked population spikes in DG (Buzsáki and Czéh 1981; Buzsáki and Eidelberg 1981; Bilkey and Goddard 1987), indicating the existence of circuit-driven inhibitions. However, the cellular targets of COM were largely unknown. In this study, we attempted to compare the MPP and COM-driven GABAergic inhibitions in transverse hippocampal slices. In order to selectively activate COM pathways, we first generated a rAAV serotype 5 (AAV5) carrying Cre-inducible ChR2-enhanced yellow fluorescent protein (eYFP) transgene for hilar MC cell targeting, and then used cell type-specific optogenetic tools to electrophysiologically map the functional connections of COM and MPP to various IN types. We also examined their influence on GC in the DG (Yizhar et al. 2011; Chancey et al. 2014). We found that photostimulation of each of these 2 inputs resulted in distinct inhibition patterns in GCs. Further analysis of pathway-specific responses revealed that BC-like cells were reliably activated by both inputs. However, 2 dendrite targeting IN subtypes, the TML- and ML-like cells, received greater excitation from the COM and were more reliably recruited by the COM than by the MPP inputs. Taken together, our results indicate that in addition to BC-like cells, TML- and ML-like cells substantially contribute to COM-mediated inhibition. Finally, we showed the preliminary results about the functional significance of COM pathway in freely-moving mice. Activation of COM pathway enhanced the contextual fear learning, although further behavior studies are required to elucidate the underlying mechanisms. The results may provide important insights into the local circuits and physiology of the hippocampus.

## Materials and Methods

### Animals

All animals were handled in accordance with the national and institutional guidelines, and protocols were approved by the Animal Care and Use Committee of the National Yang-Ming University. *Grik4-cre* (stock #006474), *Gad65-cre* (stock #010802) and *Pvalb-cre* (stock #008069) mice used for electrophysiology were adult (2–5 months old) transgenic hemizygote mice and obtained from Jackson Laboratory, Bar Harbor, ME, USA. To target excitatory neurons in MEC, we used wild-type mice with a C57BL/6 genetic background. Mice of both sexes of the above strains were included in these studies.

### Plasmid Construct for ChR2 Expression and Functional Examination

In order to express ChR2 in a cell-type specific manner, we utilized a Cre recombinase (Cre)-inducible ChR2 construct pAAV-EF1 $\alpha$ -DIO-hChR2(H134R)-eYFP-WPRE-pA, which was developed and obtained from Dr Karl Deisseroth (Stanford University, Stanford, CA, USA). For functional testing of this transgene construct, primary culture of rat cortical neurons were used. In brief, cortices of embryonic day 18 Sprague Dawley rat were removed, incubated with 2.5% trypsin in 37 °C for 15 minutes. After washing out the trypsin with CMF-HBSS several times, the digestion was stopped with 10 mL plating medium [MEM supplemented with glucose (0.6% wt/vol) and 5 % (vol/vol) fetal bovine serum]. The cortices were dissociated in 3 mL plating medium by pipetting them up and down through a flame-polished Pasteur pipette. Cell density was measured and adjusted for electroporation ( $4 \times 10^6$  cells per sample). In each electroporation, transgene construct pAAV-EF1 $\alpha$ -DIO-hChR2(H134R)-eYFP-WPRE-pA (1.5  $\mu$ g) together with a Cre-expressing construct pOG231 [1.5  $\mu$ g; a gift from Dr Ting-Fen Tsai (National Yang-Ming University, Taipei,

Taiwan)] were electroporated into cell suspensions by Amaxa Mouse Neuron Nucleofector Kit (Lonza, Cologne, Germany). After finishing the electroporation,  $10^6$  cells were seeded in the 60 mm dish containing the polylysine-treated coverslips in the plating medium. 4 hrs later, the plating medium was replaced with neuron maintenance medium [Neurobasal medium supplemented with GlutaMAX-I and B27 (Life Technologies, Grand Island, NY, USA)]. At day *in vitro* (DIV)17, functional examination of ChR2 expression was carried out. Cortical neurons grown on coverslip were transferred to a submerged chamber, perfused with extracellular solution containing (in mM): 150 NaCl, 5 KCl, 25 HEPES, 2 CaCl<sub>2</sub>, 2 MgCl<sub>2</sub>, and 10 glucose. The ChR2-eYFP expression pattern was confirmed by epifluorescence and neurons were visually selected for recordings under infrared Dodt gradient contrast optics (Leica DM6000 CFS, Leica Microsystems, Wetzlar, Germany). For whole-cell patch-clamp recordings, pipettes (4–8 M $\Omega$ ) pulled from borosilicate glass tubing (outer diameter, 1.5 mm; inner diameter, 0.86 mm; Harvard Apparatus, Holliston, MA, USA) were filled with K-gluconate based internal solution containing (in mM): 135 K-gluconate, 20 KCl, 0.1 EGTA, 2 MgCl<sub>2</sub>, 2 Na<sub>2</sub>ATP, 10 HEPES (pH 7.3 with KOH). Neurons expressing ChR2 were stimulated with 450–490 nm light, which was delivered from a mercury lamp coupled with the filter cassette and manually controlled shutter. Data were recorded with Multiclamp 700B amplifiers (Molecular Devices, Sunnyvale, CA, USA), filtered at 4 kHz, and sampled at 10 kHz with a Digidata 1440 interface (Molecular Devices) controlled by pClamp 10.2 software (Molecular Devices). All recordings were conducted in dim light conditions. The recording temperature was  $23 \pm 2$  °C.

## **AAV Generation**

In addition to the transgene construct, the AAV5 packaging (pLT-RC03) and adenoviral helper (pHGTI-Adeno1) constructs are required for AAV production (Fig 2A). These two constructs were gifts from Dr Jeng-Shin Lee (Harvard Gene Therapy Initiative, Harvard Medical School, Boston,

MA, USA). We used the adenoviral gene E1a-transformed human embryonic kidney 293 (HEK293) cells as the virus producing factories. HEK293 cells were cultured in Dulbecco's modified Eagle's medium (Thermo Fisher Scientific, Waltham, MA, USA) containing: 10% fetal calf serum, 2 mM glutamine, 100 mg/mL streptomycin, and 100 U/mL penicillin at 37 °C in a 5% CO<sub>2</sub> incubator. When HEK293 cells grew to 80–90% confluent, the transgene, packaging and adenoviral helper constructs were transfected into HEK293 cells by calcium phosphate method. After transfection for 48 to 56 hours, the medium was discarded, and the cells were dislodged by pipetting up and down with lysis buffer containing (in mM): 150 NaCl, 50 Tris (pH8.5 with HCl). To lysis the cells and release the AAV, cells were lysed by 3 freeze/thaw cycles between dry ice/ethanol bath and 37 °C water bath. The cell debris was pelleted and removed by centrifugation. To minimize the residual amount of cellular and construct DNA in the final viral product, Benzonase (25U/ml, Merck, Darmstadt, Germany) plus MgCl<sub>2</sub> (1 mM) were added into crude AAV soup and incubated for 30 min in 37 °C. The Benzonase treated AAV soup was clarified by centrifugation, and further purified by iodixanol density gradient centrifugation (Fig 2B). The discontinuous density gradient of iodixanol was prepared by OptiPrep Density Gradient Medium and TD buffer containing (in mM): 1 MgCl<sub>2</sub> and 2.5 KCl in phosphate-buffered saline (PBS). In each centrifuge tube (OptiSeal™ Polyallomer, Beckman Coulter, Brea, CA, USA), 15%, 25%, 40%, 60% iodixanol were layered from top to bottom, and clarified AAV soup was overlaid onto the prepared gradient. Tubes were centrifuged at 70,000 rpm for 1 hr at 15 °C in a Type Ti 70 rotor (Beckman Coulter). 4–5 mL of 40% gradient fraction containing the AAV particles was withdrawn by using a 23 Gauge needle and 10 mL syringe after centrifugation. The 40% iodixanol fraction was further purified and concentrated by Q Sepharose column chromatography. The 40% iodixanol fraction containing AAV was diluted 1:5 with low salt buffer containing (in mM): 20 Tris, 15 NaCl (pH8.5 with HCl) and applied to the buffer equilibrated Q Sepharose column (GE Healthcare Life Sciences, Marlborough Hills, MA, USA). The AAV was eluted with high salt buffer (20mM Tris, 500mM NaCl, pH7.5) and

collected into 8 fractions (each 2.5 mL). 1  $\mu$ L of each fraction was taken for quantifying AAV titer (see below), and the eluted fractions with the higher number of AAV were pooled and dialyzed against Dulbecco's PBS with  $\text{CaCl}_2$  and  $\text{MgCl}_2$ . Finally the AAV was concentrated by Amicon spin columns (Merck Millipore, Billerica, MA, USA) to increase the titer. The concentrated AAV was sterilized and stored in  $-70^\circ\text{C}$ . For titering AAV containing Chr2-eYFP transgene, the specific forward primer 5'-ACGATAGTCCCGATGTCTGAG-3' and the reverse primer 5'-ACTTGTCCTGTCATCCTTATCC-3' targeted to Chr2 were used. The viral DNA was isolated (either in-process sample or final AAV). The transgene construct pAAV-EF1 $\alpha$ -DIO-hChr2 (H134R)-eYFP-WPRE-pA served as standards and serial diluted in the range of  $10^1$ – $10^7$  copies/ $\mu$ L. Real-time quantitative polymerase chain reaction (PCR) was performed on an StepOnePlus™ Real-Time PCR System (Thermo Fisher Scientific). Three replicates for each sample or standards were prepared. Reactions were carried out in 20  $\mu$ L containing 1X FastStart Universal SYBR Green Master (Roche Diagnostics Corporation, Indianapolis, IN, USA), 0.2  $\mu$ M primers and 1  $\mu$ L template. Amplification condition was 10 min at  $95^\circ\text{C}$  (polymerase activation/pre-denaturation), followed by 40 cycles of denaturation at  $95^\circ\text{C}$  for 15 seconds and annealing/extension at  $60^\circ\text{C}$  for 60 seconds. In order to validate the PCR specificity, melting curve analysis was performed from 60 to  $95^\circ\text{C}$  at the rate of  $0.3^\circ\text{C}/\text{min}$  after PCR. The data point (three replicates) with the standard deviation  $< 0.167$  was included to calculate PCR efficiency and titer estimation. The PCR efficiency was calculated based on the equation describing exponential amplification of PCR at threshold cycle (CT):

$$C_n = C_i * (1 + E)^{CT}$$

$C_i$  = initial copy number

$C_n$  = copy number at CT

CT = threshold cycle

E = efficiency of target amplification

Log transformation of the equation revealed that the threshold cycle and the log-transformed input material concentration should inversely correlate in a linear fashion.

$$CT = -1/\log(1+E)*\log C_i + \log C_n/\log (1+E)$$

Standard curve was plotted with log-transformed initial construct copy number against CT, and fitted with linear regression. R<sup>2</sup> value of the linear fitting should be larger than 0.99. The slope of the fitting line was used to calculate PCR efficiency. Among all realtime PCR experiments, the PCR efficiency is between 0.96 to 1.05. The equation of the fitting line was used to estimate the titer of AAV. CT value of each sample was converted to “copy number” first (equivalent to construct copy number) and then converted to genome copies/mL.

To target the excitatory neurons in the MEC, we used the AAV5 carrying CaMKII $\alpha$  promoter-driven ChR2 tagged with mCherry [AAV5-CaMKII $\alpha$ -hChR2(H134R)-mCherry-WPRE-pA], which was produced by the University of North Carolina Vector Core Facilities, Chapel Hill, NC, USA.

For the behavior experiments, we used the AAV5 carrying Cre-inducible eYFP transgene AAV5-EF1 $\alpha$ -DIO-eYFP for the control experiment. This virus was produced by the University of North Carolina Vector Core Facilities.

### **Stereotaxic Injection**

Mice (postnatal day >30) were anesthetized with 4% isoflurane (vol/vol; Halocarbon Laboratories, North Augusta, SC, USA) in 100% oxygen in an induction chamber (air flow rate: 4 mL/min), and their heads were shaved for further operation. Mice were placed onto the stereotaxic frame (Stoelting Co., Wood Dale, IL, USA). The mouths and noses of the mice were covered by an

anesthetizing mask, supplied with approximately 1.5% isoflurane air flow (4 mL/min). A homeothermic blanket (Panlab Harvard Apparatus, Barcelona, Spain) was placed below the mice to keep the body temperature constant (34 °C). After securing the head with 2 ear bars, 75% ethanol was used to sterilize the surgical area and the eyes were protected by ophthalmic gel. To target hilar MCs of the dorsal hippocampus, a midline scalp incision (~1 cm) was made with scissors and the skin pulled aside to expose the skull. A small craniotomy [coordinates from Bregma: anteroposterior (AP): -2 mm; mediolateral (ML):  $\pm 1.3$  mm] was made directly over the dorsal hippocampus. The viral vector was delivered through the craniotomy to the 2 locations within the dorsal hippocampus [dorsoventral (DV): -2 and -1.8 mm], using a 10- $\mu$ L NanoFil syringe (World Precision Instruments, Sarasota, FL, USA) and a 35-gauge beveled metal needle. Injection volume (0.5  $\mu$ L at each location) and flow rate (0.1  $\mu$ L/min) were controlled with a nanopump Controller (KD Scientific, Holliston, MA, USA). After viral injection, the needle was left in place 0.2 mm above the injection sites for 10 min before it was withdrawn slowly. Similar procedures were made for targeting excitatory neurons in the MEC except that the craniotomy and subsequent viral injection were delivered to the 2 locations within the MEC (coordinates from Bregma: AP: -4.7 mm; ML:  $\pm 3.3$  mm; DV: -3.5 and -3.3 mm). After viral injection, the incision was closed by suturing and mice were placed back to into the home cage for recovery. All animals were allowed at least 3 weeks of rest before the next experimental stage was commenced, ensuring complete recovery and sufficient gene expression.

### **optical fiber implantation**

The fiber-optic cannula for implantation consisted of a ferrule (1.25 mm in diameter and 6.4 mm long; Precision fiber product, Milpitas, CA, USA) and an optic fiber with flat tip (230  $\mu$ m in diameter). The implantation of fiber-optic cannula into the DG was performed immediately after injection of virus. The site of optical fiber implantation was contralateral to the viral injection site

(coordinates from Bregma: AP:  $-1.8$  mm; ML:  $\pm 1$  mm, contralateral to the viral injection site; DV:  $-1.8$  mm), which allows illumination of ChR2 positive COM pathway. To fix the fiber-optic cannula on the skull, C & B Superbond (Sun Medical, Moriyama, Japan) was applied to the surface of the skull around the cannula for 10 min. After the C & B Superbond was hardened, the cannula was released from the home-made holder. Dental cement (GC corporation, Tokyo, Japan) was applied around the cannulation site. After optic fiber implantation, mice were placed back into the home cage for recovery.

### **Preparation of Brain Slices**

After at least 3 weeks of recovery, virus-injected mice (postnatal day  $>51$ ) were anesthetized with isoflurane and transcardially perfused with cold carbogenated (95% O<sub>2</sub> and 5% CO<sub>2</sub>) sucrose solution ( $\sim 30$  mL) containing (in mM): 87 NaCl, 25 NaHCO<sub>3</sub>, 1.25 NaH<sub>2</sub>PO<sub>4</sub>, 2.5 KCl, 10 glucose, 75 sucrose, 0.5 CaCl<sub>2</sub>, and 7 MgCl<sub>2</sub>. The brain was dissected out and coronal slices (300  $\mu$ m) were prepared in the same carbogenated sucrose solution using a vibrating tissue slicer (DTK-1000; Dosaka, Kyoto, Japan) under a dim red light. Following sectioning, slices were incubated in a holding chamber filled with the carbogenated sucrose solution at 34 °C for about 25 min, then shifted to room temperature for further experiments.

### **Slice Electrophysiology and Optical Stimulation**

For experiments, individual slices were transferred to a submerged chamber and were continuously perfused with carbogenated artificial cerebrospinal fluid (ACSF) containing the following (in mM): 125 NaCl, 25 NaHCO<sub>3</sub>, 1.25 NaH<sub>2</sub>PO<sub>4</sub>, 2.5 KCl, 25 glucose, 2 CaCl<sub>2</sub>, and 1 MgCl<sub>2</sub>. The ChR2-eYFP or ChR2-mCherry expression pattern was confirmed by epifluorescence and neurons were visually selected for recordings under infrared Dodt gradient contrast optics (Leica DM6000 CFS,



Leica Microsystems). Axonal fibers expressing ChR2 were stimulated with 473-nm light, which was delivered from a 200- $\mu\text{m}$  multimode optical fiber (0.39 numerical aperture, Thorlabs, Newton, NJ, USA) coupled with a 473-nm, diode-pumped, solid-state laser (OEM Laser Systems, Midvale, UT, USA). The distance between the tip of optic fiber and the recorded single cell/pair was approximately 100–300  $\mu\text{m}$ , and the distance between the recorded pair was smaller than the tip diameter (200  $\mu\text{m}$ ). The area of photostimulation was large enough to cover the entire DG under this condition. Near-maximum light intensity was also used to avoid the possible difference of light intensity due to displacement of fiber between recorded pair. The onset and duration of light pulses were detected by a GaP Photodiode (wave-length range: 150–550 nm, 1 ns rise time, Thorlabs) placed near the submerged chamber. For cell-attached and whole-cell patch-clamp recordings, pipettes (4–8 M $\Omega$ ) pulled from borosilicate glass tubing (outer diameter, 1.5 mm; inner diameter, 0.86 mm; Harvard Apparatus) were filled with low Cl<sup>-</sup> internal solution, containing the following (in mM): 136.8 K-gluconate, 7.2 KCl, 0.2 EGTA, 4 MgATP, 10 HEPES, 7 Na<sub>2</sub>-phosphocreatine, 0.5 Na<sub>3</sub>GTP (pH 7.3 with KOH), and 0.5% biocytin (wt/vol; Life Technologies). To measure the inhibitory (I)–excitatory (E) conductance ratio, Cs<sup>-</sup> based intracellular solution was used, containing (in mM): 121.5 CsMeSO<sub>3</sub>, 0.1 EGTA, 4 MgCl<sub>2</sub>, 13.5 CsCl<sub>2</sub>, 10 HEPES, 5 QX-314 bromide, 2 Na<sub>2</sub>ATP, 10 Na<sub>2</sub>-phosphocreatine, 0.3 Na<sub>3</sub>GTP, and 0.2% biocytin (wt/vol). Excitatory and inhibitory synaptic responses were evoked by 10 Hz train photostimulation (light pulse duration, 5 ms; intertrain interval, 15 s). Pipette capacitance and series resistance were compensated (100% in current clamp and 70% in voltage clamp). Data were recorded with Multiclamp 700B amplifiers (Molecular Devices), filtered at 4 kHz, and sampled at 10 kHz with a Digidata 1440 interface (Molecular Devices) controlled by pClamp 10.2 software (Molecular Devices). All recordings were conducted in dim light conditions. The recording temperature was  $23 \pm 2$  °C in the majority of experiments and  $34 \pm 2$  °C in subsets.

## Immunohistochemistry

To identify the recorded neurons (filled with 0.2 or 0.5% biocytin), brain slices were fixed overnight with 4% paraformaldehyde (wt/ vol) in phosphate-buffered saline (PBS). After washing with PBS 3 times, slices were incubated with streptavidin-conjugated Alexa Fluor 594 or 488 (1 : 400; Life Technologies) in PBS and 0.3% Triton X-100 (vol/vol; USB Co., Cleveland, OH, USA) overnight at 4 °C. After washing 6 times with PBS, slices were mounted onto slides with mounting medium Vectashield (Vector Laboratories, Burlingame, CA, USA). For nuclear staining, slices were incubated with 4',6-diamidino-2-phenylindole (DAPI; 1 : 5000; Life Technologies) for 15 min before finally washing with PBS 6 times. Labeled cells were imaged using a confocal/two-photon laser excitation microscope (Leica SP5 module, Leica Microsystems). Confocal image stacks were reconstructed with Neuromatic 1.6.5 software (developed by Darren Myatt, University of Reading, Reading, Berkshire, UK). To characterize Cre recombinase expression in the *Grik4-cre* mouse line, the *ROSA26-LacZ* reporter mouse line was crossed with the *Grik4-cre* mouse. The offspring, which contained both *cre* and *lacZ* genes, were used for X-gal staining. In brief, mice were anesthetized with pentobarbital (50µg/mL) and transcardially perfused with PBS, followed by 4% paraformaldehyde in PBS. The fixed brain was removed and post-fixed in 4% paraformaldehyde for an additional 6 hr. After dehydrating with 30% sucrose in PBS, the fixed brain was embedded in optimal cutting temperature compound (Sakura Finetek Japan Co., Tokyo, Japan) for cryosectioning into 30 µm coronal slices. The slices were incubated with X-gal working solution containing (in mM): 10 phosphate buffer, 150 NaCl, 3.5 K<sub>3</sub>Fe(CN)<sub>6</sub>, 3.5 K<sub>4</sub>Fe(CN)<sub>6</sub>, 1 MgCl<sub>2</sub>, 0.3 chloroquine, 0.01% Na-deoxycholate (wt/vol), 0.2% octyl-1-phenoxyethoxyethanol (NP-40, vol/vol), and 0.1% X-gal (wt/vol) at 30 °C for 16 hr, followed by intensifying solution (0.3 mM chloroquine in

PBS) for an additional 8 hr. After washing the slices with PBS 3 times, slices were mounted onto slides with the mounting medium Entellan® new (Merck). X-gal signals were visualized and photographed using a stereoscopic microscope (Leica EZ4D, Leica Microsystems).

## **Chemicals and Drugs**

The N-methyl-D-aspartate receptor (NMDAR) antagonist D-2-amino-5-phosphonopentanoate (D-AP5),  $\alpha$ -amino-3-hydroxy-5-methyl-4-isoxazolepropionic acid (AMPA)/kainate receptor-specific antagonist 6-cyano-7-nitroquinoxaline-2,3-dione (CNQX), and the sodium channel antagonists tetrodotoxin citrate (TTX) and QX-314 bromide were purchased from Ascent Scientific, Avonmouth, UK. X-gal was purchased from GMbiolab Co., Taichung, Taiwan. NP-40 used in X-gal staining was purchased from BioShop Canada, Inc., Burlington, ON, Canada. All other reagents were purchased from Sigma-Aldrich Co., Saint Louis, MO, USA.

## **Contextual Fear Conditioning and *in vivo* Photostimulation**

To reduce anxiety of mice during behavior tests sessions, we familiarize them with human hand contact at least 2 days before the session by gently holding and releasing them several times until they were habituated and stopped struggling (Hurst and West 2010). Contextual fear conditioning was performed in a chamber in the dim light condition. The chamber (17.8 x 17.8 x 30.5 cm; Coulbourn Instruments, Whitehall, PA, USA) was equipped with a floor grid (stainless-steel rods) through which electrical foot shock could be conducted. On the first conditioning day, optic fiber was attached to the patch cable (Precision fiber product). The other side of patch cable contains an FC/PC adaptor and is coupled to a 473-nm, diode-pumped, solid-state laser (OEM Laser Systems). Next, mice were placed into the chamber to habituate for 2 min. After 2-min habituation, mice immediately received 3 trials (inter-trial interval: 1 min) of foot shock (0.6 mA, 2 S) in the following 3 min. The blue light pulse (10-Hz stimulation train, 5 ms light pulse, 10 mW power from

the fiber tip) was delivered through the optic fiber from the 473 nm DPSS laser during the entire training period. The chamber was cleaned with 70 % ethanol before and after each training session. After the last shock, mice were observed for 1 min and then returned to the home cage. 24 hours later, mice with patch cable attached on the fiber optic were placed back into the same chamber for 5 min without foot shock and light to access the contextual fear retention. After removal of the patch cable, mice were sent back to home cage. To evaluate the fear learning in Day 1 conditioning and Day 2 contextual fear retention test, we recorded the freezing time per min when mice were in the chamber. Freezing level is expressed as the percentage of freezing time versus per 1 min observation time. The freezing time was defined as more than 2 s of immobility with crouching posture. Freezing behavior was analyzed *post hoc* by using the instantaneous time sampling.

### **Data Analysis and Statistics**

For analyzing the variabilities of ChR2 expression and axonal projection patterns, *post hoc* fixed slices after electrophysiological recording were used. For each sacrificed animal (with one injection), a coronal section with the anterior-posterior coordinate around 2 mm behind the Bregma was selected for analysis; 11 and 7 sections were analyzed respectively for COM and MPP ChR2 expression. Images were taken by a confocal/two-photon laser excitation microscope (Leica SP5 module, Leica Microsystems), and two different imaging settings (laser wavelength, laser intensity, PMT gain, etc.) were applied for COM targeting (ChR2-eYFP) and MPP targeting (ChR2-mCherry) slices respectively. To analyze the ChR2 expression, a straight, one-pixel wide line drawn from the crest of GCL/hilus border to the edge of lower blade molecular layer defined the region of interest in which the eYFP or mCherry intensity was quantified using ImageJ (National Institute of Health, Bethesda, MD, USA). The intensity was plotted against the normalized distance across different laminar layers of DG.

Electrical data were analyzed using Clampfit 10.2 (Molecular Devices) and Prism 5.0 (GraphPad). The onset of the synaptic response was determined by the intersection of a line through the 20% and 80% points of the rising phase of the excitatory postsynaptic current (EPSC) and the baseline. To calibrate evoked inhibitory postsynaptic currents (IPSCs) during successive 10 Hz photostimulations, a single exponential fit of the decay of the preceding IPSC was subtracted from the subsequent IPSC. The IPSC amplitude after subtraction was used for the conductance calculation. To calculate the conductance, the EPSC and the IPSC were divided by their driving forces, respectively. The input resistance ( $R_{in}$ ) was measured as the ratio of the steady-state (last 100 ms of the 1-s pulse; average of 1–4 traces) voltage response and the 1-s hyperpolarizing current pulse amplitude (100 pA). Spike delay was calculated as the time elapsed from the onset of photostimulation to the peak of action current in cell-attached recordings. Data are presented as mean  $\pm$  standard error of mean (SEM). Error bars in figures also show SEMs. Statistical significance was tested using the Mann–Whitney rank-sum test or two-way repeated-measures ANOVA using GraphPad Prism 5.0. Significance levels were set at  $P < 0.05$  (\*),  $P < 0.01$  (\*\*), and  $P < 0.001$  (\*\*\*) for the entire family of comparisons.

## Results

### Generation of AAV for cell type-specific targeting of ChR2

The first goal of this study is generating a AAV containing Cre-inducible ChR2. Before packaging this transgene construct into AAV, we examined the function of transgene construct pAAV-EF1 $\alpha$ -DIO-hChR2(H134R)-eYFP-WPRE-pA on cultured rat cortical neurons. After co-electroporation of this transgene construct together with a Cre-expressing construct pOG231 for several days, neurons containing both constructs express ChR2-eYFP. As illustrated in Fig. 1A, this genetic strategy relied on Cre-mediated flipping of ChR2-eYFP anti-sense reading frame floxed by two nested pairs of incompatible lox sites (oppositely oriented loxP and lox2722 pairs) into sense reading frame. The first reversible step enables the second irreversible excision of lox site floxed by the other incompatible lox sites (the same orientation). The second irreversible event prevents further inversion, increasing the expression level of ChR2-eYFP. Functional examination of ChR2 expression was performed at DIV 17 (Fig. 1B). When the ChR2-eYFP expressing neuron was illuminated with blue light (420–490 nm), the neuron was depolarized to generate spikes and the ChR2-mediated current together with synaptic responses were induced. Pure ChR2-evoked spikes and inward current could still be observed when the synaptic transmissions were blocked by kynurenic acid (2 mM) and gabazine (1  $\mu$ M). Alternatively, when ChR2-eYFP negative neuron was recorded and illuminated with blue light, the synaptic responses could be observed and abolished by synaptic blockers (Fig. 1C). This data suggests that ChR2 is present in axons and can be activated, resulting in transmitter release and synaptic transmission to downstream targets. Therefore we demonstrate the functional expression of ChR2 in cultured rat cortical neurons by using Cre-inducible ChR2 construct.

The next step is generating AAV for *in vivo* targeting of Cre-inducible ChR2 transgene. To achieve this, the Cre-inducible ChR2 transgene construct together with two AAV vectors were used to produce AAV, and serotyped with AAV5 Caspid (Fig. 2). AAV5 is a commonly used serotype in neuroscience research with panneuronal tropism (McFarland et al. 2009; Yizhar et al. 2011). During the production and purification of AAV (Fig. 2 A,B), we developed the quantitative PCR method for monitoring viral titer of in-process samples. A specific primer pair within ChR2 transgene was designed (corresponding to the nucleotide 379483, 104 base pairs). Primer specificity was confirmed by melting curve analysis, which detected a single peak of fluorescence change, indicating that only one PCR product is present the reaction tube (Fig. 2C). PCR efficiency was also validated by standard curve analysis (Fig. 2 D; also see Materials and Methods). Among all quantitative PCR experiments, the results of PCR efficiency test range from 0.96 to 1.05, providing precise measurement of viral titer from trial to trial. The quantification results were summarized in Fig. 2E. After purification and concentration of AAV5 by Q-sepharose column chromatography, 2 fractions (Q2, Q3) with high titer were pooled together, dialysed and concentrated, yielding the final AAV5-EF1 $\alpha$ -DIO-hChR2(H134R)- eYFP-WPRE-pA with the titer  $3.95 \times 10^{11}$  genomes/mL.

We tested the function of AAV5-EF1 $\alpha$ -DIO-hChR2(H134R)- eYFP-WPRE-pA by injection of this virus into Cre drivers (Fig. 3A). The first tested Cre driver is *Gad65-cre* mice, which express Cre recombinase in all kinds of GABAergic neurons. After injection of virus into the hilar region of the dorsal hippocampus for 3 weeks, ChR2-eYFP was expressed in non-principal neurons in the DG of *Gad65-cre* mouse (Fig. 3B). ChR2 function was confirmed by recording of a ChR2-eYFP positive cells in ML, which was depolarized and generated spikes upon blue light illumination (473 nm; Fig. 3C). We also confirmed the specificity of AAV5-EF1 $\alpha$ -DIO-hChR2(H134R)- eYFP-WPRE-pA by doing the same experiment on another Cre driver mice *Pvalb-cre*, which express Cre recombinase on the fast spiking BC-like cells. After 3 weeks of virus injection, ChR2-eYFP was

expressed on the cells located in the hilus border, which have axon arborization within granule cell layer, a typical characteristic of BC-like cells (Fig. 3D). Immunostaining also showed a subset of Chr2 positive cells expressing parvalbumin (Fig. 3D inset). Furthermore, photostimulation induced fast spiking (> 80 Hz) of a Chr2 expressing cell, indicating the functional expression of Chr2 on BC-like cells (Fig. 3F). Therefore, we successfully generated a AAV containing Cre-inducible Chr2, which can be used as a cell-type specific optogenetic tools to study circuit functions.

### **Selective Chr2 Expression in the COM or MPP**

Since we generated the AAV5-EF1 $\alpha$ -DIO-hChr2(H134R)-eYFP-WPRE-pA, we applied this optogenetic tool together with an AAV5 encoding a CaMKII $\alpha$  promoter driven-Chr2 transgene AAV5-CaMKII $\alpha$ -hChr2(H134R)-mCherry to selectively investigate neurotransmission of the COM and the MPP to the DG. To target the COM, we unilaterally injected AAV5-EF1 $\alpha$ -DIO-hChr2(H134R)-eYFP-WPRE-pA into the hilar region of the dorsal hippocampus of *Grik4-cre* hemizygous mice (Fig. 4A). We first assessed the distribution and efficiency of Cre/loxP recombination in this transgenic line by crossing it with the *ROSA26-LacZ* reporter mouse and analyzing X-gal-stained brain sections from *cre/lacZ* double-transgenic mice (see Materials and Methods). As reported earlier (Nakazawa et al. 2002), Cre recombinase activities were detected in CA3 pyramidal neurons, GCs, and neurons in the hilar region (Fig. 4B, left upper). Three weeks after injection, the Chr2-eYFP fusion protein was expressed in CA3 pyramidal neurons, GCs, putative MCs, and their axonal projections on the ipsilateral side as well as the COM axonal projections across the hippocampal commissure (Fig. 4B, left lower). Notably, Chr2-eYFP was densely expressed along the IML of the contralateral side of the dorsal DG (Fig. 4B), consistent with previous reports that MC axonal bundles primarily target the proximal dendrites of contralateral GCs (West et al. 1979; Buckmaster et al. 1996; Scharfman and Myers 2013). To characterize the putative Chr2-eYFP-labeled MCs in the hilus, we filled them with biocytin during



whole-cell recordings and correlated their morphologies with their intrinsic properties. In the injection site, the biocytin-filled cells that expressed ChR2-eYFP had characteristic MC morphology including thorny excrescences on proximal dendrites (Fig. 4C, arrowhead). When the ChR2-eYFP-labeled MC was illuminated with a blue light pulse in the presence of the AMPA receptor-specific antagonist CNQX (10  $\mu$ M), it depolarized and generated spikes in current clamp (Fig. 4D, upper). Similarly, an inward ChR2-mediated photocurrent (peak amplitude,  $1391 \pm 714$  pA,  $n = 4$ ) was detected in voltage clamp (Fig. 4D, lower). Also, it is worth noting that we did not observe ChR2-eYFP expression in the IML of the contralateral DG when the viral transduction was mainly restricted in the CA3 area of the injection site (Fig. 5), ruling out the possibility that the dorsal CA3 pyramidal neurons project their axons to contralateral IML.

To target the MPP, we injected an AAV5-CaMKII $\alpha$ -hChR2(H134R)-mCherry into the MEC of wild-type mice (Fig. 6A). Three weeks after injection, ChR2-mCherry expressing neurons and their axonal projections were observed around the MEC injection site (Fig. 6B, left upper) and the dorsal hippocampus (Fig. 6B, left lower). Notably, ChR2-mCherry-labeled fibers were clearly demarcated in part of the IML and the medial one-third molecular layer (MML), indicating selective ChR2 expression in the MPP (Fig. 6B, right).

We also analyzed the variabilities of ChR2 expression and axonal projection patterns. We found that ChR2 expression pattern is consistent among different animals. ChR2-eYFP was expressed within the IML in COM-targeting slices, and the ChR2-mCherry expression was found across IML and MML regions in MPP-targeting slices. However, the intensity of ChR2 expression exhibits modest variation. The variability of ChR2 expression may arise from the efficacy of viral infection (Fig. 7).

## GCs Receive More Inhibition Than Excitation From the COM

To determine the proper intensity for photostimulation in subsequent experiments, we varied the light intensities (duration 5 ms) and recorded the optically evoked inward EPSCs in GCs ( $V_{\text{hold}} = -75$  mV, near the IPSC reversal potential;  $[\text{Cl}^-]_i = 7.2$  mM). The GCs were filled with biocytin during recordings and were identified *post hoc* (Fig. 8A). Analysis of the input–output relationship showed that the EPSC amplitude was saturated at high light intensities (Fig. 8B). The near-maximal light intensity (blue area in Fig. 8B; 30–60 mW for COM–GC and 53–60 mW for MPP–GC) was chosen for subsequent experiments to ensure maximum recruitment of INs during light stimulation. In the following experiments, we intended to measure EPSCs and putative circuit-driven IPSCs in single GCs. We used 2 intermediate holding potentials ( $V_{\text{hold}} = -25$  mV, near the experimentally determined IPSC reversal potential and  $V_{\text{hold}} = 10$  mV, near the experimentally EPSC reversal potential; see Fig. 9) with Cs-based internal solution ( $[\text{Cl}^-]_i = 35$  mM; see Materials and Methods) to measure EPSCs and IPSCs, respectively. To avoid contamination of NMDAR-mediated currents, we measured IPSCs and I/E ratios in the presence of the NMDAR blocker  $\text{D-AP5}$  ( $50 \mu\text{M}$ ; Fig. 10A). Because the same driving forces (35 mV) were used for excitation and inhibition, we can thus directly compare excitatory and inhibitory conductances. We recorded optically evoked EPSCs ( $215 \pm 43$  pA;  $n = 13$  in the COM group;  $215 \pm 28$  pA;  $n=12$  in the MPP group;  $V_{\text{hold}} = -25$  mV) and IPSCs ( $277 \pm 55$  pA;  $n=13$  in the COM group;  $327 \pm 41$  pA;  $n=12$  in the MPP group;  $V_{\text{hold}} = 10$  mV). We know that the kinetic properties of EPSCs are related to the electrotonic distance of the synapses, which is dependent on the laminar organization of the inputs. Consistent with this notion, the 20–80% rise time and decay time constant of evoked EPSCs at the COM were significantly shorter than those at the MPP (20–80% rise time, COM,  $1.0 \pm 0.1$  ms,  $n=13$  vs. MPP,  $1.8 \pm 0.1$  ms,  $n=12$ ;  $P < 0.0001$ ; decay time constant, COM,  $4.6 \pm 0.1$  ms,  $n = 13$  vs. MPP,  $5.9 \pm 0.4$  ms,  $n = 12$ ;  $P = 0.006$ ; Table 1). In order to rule out the possibility that the IPSCs may also arise from direct photostimulation of local ChR2 positive interneurons as a result of non-specific genetic targeting,

we performed a subset of experiments. As shown in Fig. 10A–C, bath application of CNQX (10  $\mu$ M) abolished light-evoked EPSCs and IPSCs at both synapses, confirming that the EPSCs are indeed glutamatergic, AMPA/kainate receptor-mediated and that the IPSCs are disinaptic.

We next examined the synaptic delay of the EPSC following photostimulation. Synaptic delay was calculated from the time of the onset of photostimulation to the onset of the EPSC. The average delay of the EPSC at the COM–GC and MPP–GC synapses was  $2.9 \pm 0.1$  ms ( $n = 13$ ) and  $3.9 \pm 0.2$  ms ( $n = 12$ ), respectively (Table 1). Because EPSCs significantly preceded IPSCs, we thus measured the delay ( $\Delta t$ ) of the IPSC relative to the EPSC following photostimulation (Fig. 11A). The average  $\Delta t$  of the IPSC at the COM–GC and MPP–GC synapses was  $3.9 \pm 0.3$  ms ( $n = 13$ ) and  $6.7 \pm 0.5$  ms ( $n = 12$ ), respectively. A significantly longer  $\Delta t$  at the MPP–GC synapse (MPP vs. COM;  $P = 0.0003$ , Mann–Whitney rank-sum test; Fig. 11A) suggests that INs were activated with longer excitatory postsynaptic potential (EPSP)-spike latencies (Maccaferri and Dingledine 2002) or recruited through recurrent excitatory inputs (Bartos et al. 2011).

Dentate GCs have been shown to receive coherent theta (4–10 Hz)-band EPSCs *in vivo* (Pernía-Andrade and Jonas 2014). We finally investigated the synaptic excitation and inhibition during successive inputs coming from either the COM or the MPP. To compare synaptic inhibitory drive across different levels of excitatory drive, we derived their corresponding peak excitatory and inhibitory postsynaptic conductances (i.e., IPSP vs. EPSP) and expressed inhibition relative to excitation [IPSP/EPSP (I/E) ratio]. When 10 brief (5 ms) light pulses at 10 Hz were delivered to the COM, the EPSCs depressed much more than the IPSCs (Fig. 11B), yielding higher I/E ratios in GCs (see Fig. 12 for IPSC calibration). In contrast, the IPSCs significantly depressed, whereas the EPSCs remained relatively constant, during 10 Hz photostimulation of MPP (Fig. 11C). This results in striking facilitation in the I/E ratio at the COM–GC synapse, but depression at the MPP–GC

synapse during repetitive stimulation (Fig. 11D,  $n = 12$  for COM–GC and  $n = 11$  for MPP–GC;  $P = 0.0027$ , two-way repeated-measures ANOVA). When comparing the I/E ratio at the 10th light pulse, the mean I/E ratio at the COM ( $4.2 \pm 0.7$ ,  $n = 12$ ) is about 7-fold greater than that at the MPP ( $0.6 \pm 0.2$ ,  $n = 11$ ). Note that the higher I/E ratios at the COM when compared with the MPP are also observed when recordings are made at physiological temperature (Fig. 13). Collectively, synaptic dynamics of IPSCs at the COM distinct from that at the MPP suggests that activation of COM and MPP pathways may differentially recruit different IN populations.

### **Comparison of COM- and MPP-mediated EPSCs Across Various IN Type**

To dissect afferent-driven GABAergic transmission onto GCs, we directly investigated the excitatory input to different types of INs. Patch-clamp whole-cell recordings were obtained from INs located near the border between the GCL and hilus or in the ML. To normalize ChR2 expression levels between slices, we simultaneously recorded pairs of a local IN and an adjacent GC in the DG in brain slices (Fig. 14A,B). The critical advantage of this simultaneous paired-recording technique is that it enables the direct comparison of synaptic input strength to 2 cells, while stimulating an identical group of axons (Lee et al. 2013). We measured the amplitude of the light-evoked EPSC in both cells ( $V_{\text{hold}} = -75$  mV near the IPSC reversal potential;  $[\text{Cl}^-]_i = 7.2$  mM) and computed its normalized values. To minimize in-group heterogeneity due to differing maturation stages among GCs, only GCs with an  $R_{\text{in}}$  lower than  $600$  M $\Omega$  (corresponding to mature GCs, Schmidt-Hieber et al. 2004; Vivar et al. 2012; Dieni et al. 2013) were included for analysis (Fig. 14C). Overall, the  $R_{\text{in}}$  of GCs showed no difference between COM and MPP photostimulation groups (Fig. 14C;  $279 \pm 14$  M $\Omega$ ;  $n = 35$  in the COM group vs.  $308 \pm 17$  M $\Omega$ ;  $n = 29$  in the MPP group,  $P = 0.1379$ , Mann–Whitney rank-sum test).

We first compared the EPSC events in all INs and GCs in response to COM or MPP photostimulation (Fig. 15). We analyzed the differentiation of EPSCs (plot  $dI/dt$  versus  $t$ ) and showed that effects of optical stimulation are comparable for both inputs. The synaptic responses in all recorded cells revealed single or multiple EPSC events following each light pulse. To investigate monosynaptic connections, we selectively analyzed the first EPSCs for all experiments. The synaptic delays of COM- and MPP- mediated EPSCs in all IN subtypes were similar to those in GCs, which were known to receive monosynaptic transmission from the COM and MPP (Table 2). Note that these synaptic delays were shorter than those measured in the presence of TTX ( $1 \mu\text{M}$ ) and 4-aminopyridine (4-AP,  $1 \text{ mM}$ ); COM,  $3.1 \pm 0.3 \text{ ms}$  and MPP,  $4.9 \pm 0.2 \text{ ms}$  in control vs. COM,  $6.1 \pm 0.7 \text{ ms}$  and MPP,  $9.5 \pm 1.0 \text{ ms}$  in the TTX and 4-AP; Fig. 16), confirming monosynaptic transmission between COM and INs and between MPP and INs.

On the basis of target selectivity of the axon, somatic locations, and physiological properties, 5 different IN subtypes have been distinguished in the DG, including BC-, HICAP-, HIPP-, TML-, and ML-like cells (Fig. 17; Han et al. 1993; Freund and Buzsáki 1996; Mott et al. 1997; Hosp et al. 2014; Liu et al. 2014). BC-like cells were identified by their axonal arborizations being largely confined to the GCL (Fig. 17A, upper, 5/8 cells in the COM group and 3/5 cells in the MPP group were confirmed post hoc, based on morphology) and their characteristic fast-spiking pattern (8/8 cells in the COM group and 5/5 cells in the MPP group had a maximum firing rate of  $> 80 \text{ Hz}$  at  $23 \pm 2 \text{ }^\circ\text{C}$ ). We found that both pathways evoked larger EPSCs in BC-like cells than in GCs during the 10-Hz photostimulation train. On average, the normalized EPSCs evoked by COM stimulation were greater than those by MPP stimulation (Fig. 17A,  $n = 8$  in the COM group vs.  $n = 5$  in the MPP group,  $P = 0.029$ , two-way repeated-measures ANOVA).

We next investigated the response properties of HICAP- and HIPP-like cells to COM and MPP stimulation, respectively. The axonal arborizations of HICAP-like cells were mainly confined

to the IML (Fig. 17B, upper), whereas the arborizations of HIPP-like cells extended from the MML to the outer one-third of the ML (Fig. 17C, upper). Notably, both COM- and MPP-evoked EPSC amplitudes in HICAP- and HIPP-like cells were significantly smaller than in GCs during 10-Hz train photostimulation (Fig. 17B,C, middle). Unlike HICAP- and HIPP-like cells, TML-like cells, as reported previously [Soriano and Frotscher 1993; Mott et al. 1997; Hosp et al. 2014; termed atypical HIPP cells in Liu et al. (2014)], had their cell bodies located at the hilar–GCL border and projected their axons throughout the entire ML (Fig. 17D, upper). Notably, TML-like cells responded differently to COM and MPP stimulation. TML-like cells received stronger input from the COM compared with GCs. However, the input strengths from the MPP to TML-like cells and to GCs were similar (Fig. 17D, middle and bottom). During 10-Hz repetitive stimulation, the normalized COM-evoked EPSCs were significantly greater than the normalized MPP-evoked EPSCs (Fig. 17D, middle,  $n = 10$  in the COM group vs.  $n = 7$  in the MPP group,  $P = 0.0116$ , two-way repeated-measures ANOVA). Finally, we identified a subpopulation of INs, hereafter called ML-like cells, which had their somatic location and axonal arborizations confined to the ML (Fig. 17E, upper). ML-like cells received a larger excitatory input from the COM compared with the MPP. The normalized EPSCs generated by the COM were always significantly larger than those generated by the MPP during 10-Hz train stimulation (Fig. 17E,  $n = 7$  in the COM group vs.  $n = 6$  in the MPP group,  $P = 0.0003$ , two-way repeated-measures ANOVA).

Taken together, COM- and MPP-mediated transmission onto INs is targeting cell-dependent. BC-, TML-, and ML-like cells received significantly stronger inputs from the COM relative to the MPP. In contrast, HICAP- and HIPP-like cells received relatively weak inputs from both afferents. Furthermore, we also analyzed short-term plasticity of EPSCs in all IN-GC pairs. Target cell-specific facilitation and depression were observed in both COM and MPP pathways (Fig. 18). The

heterogeneity of excitatory afferent inputs to INs suggests that the COM and MPP are likely to recruit different IN subpopulations.

### **TML- and ML-Like Cells Were Preferentially Recruited by the COM**

Does the COM versus MPP recruit different IN subtypes? In addition to the heterogeneity of excitatory afferent inputs to INs, other properties such as membrane time constant (Buhl et al. 1996), input resistance (Khurana et al. 2011), EPSP kinetics (Maccaferri and Dingledine 2002), and the strength of inhibitory inputs (Banks et al. 2000) also affect EPSP-spike coupling. Here, we directly addressed spike transmission in 5 identified IN classes in the DG. Recordings were obtained in the cell-attached configuration to avoid interfering with the intracellular ionic composition. The spikes, detected as extracellular action currents, were recorded from the somata of dual-recorded INs and GCs (Fig. 19A,B). Following cell-attached recordings, we made biocytin-filled whole-cell recordings from the same cells and identified cell morphology *post hoc*. We first compared spike timings between GCs and INs in response to COM versus MPP photostimulation. In all sets of dual recordings, GCs exhibited a similar spike delay in response to COM versus MPP photostimulation (COM,  $8.5 \pm 0.9$  ms,  $n = 5$ ; Fig. 19A vs. MPP,  $8.4 \pm 0.7$  ms,  $n = 7$ ; Fig. 19B;  $P=0.7551$ , Mann–Whitney rank-sum test). Relative to GC spike timing, BC-like cells generated spikes with a shorter delay (COM,  $6.2 \pm 0.5$  ms,  $n = 5$ ; Fig. 19A vs. MPP,  $6.3 \pm 0.6$ ms,  $n=4$ ; Fig. 19B;  $P = 1$ ,Mann–Whitney rank-sum test). In contrast, both HICAP- and HIPPI-like cells showed a longer delay in response to either COM or MPP stimulation if they spiked (Fig. 19A,B). Notably, both TML- and ML-like cells showed differential responses to COM versus MPP stimulation. They exhibited a shorter spike delay in response to COM photostimulation (TML-like cell,  $5.2 \pm 0.5$  ms,  $n = 7$ ; Fig. 19A; ML-like cell,  $4.6 \pm 0.9$  ms,  $n = 4$ ; Fig. 19A) compared with that in response to MPP photostimulation (TML-like cell,  $12.8 \pm 1.4$  ms,  $n = 2$ ; Fig. 19B; ML-like cell,  $9.7 \pm 0.2$  ms,  $n = 3$ ; Fig. 19B).

We next compared the spike probabilities between GCs and INs by simultaneously dual recordings from a GC and an adjacent IN during 10-Hz train photostimulation. In all sets of dual recordings, the great majority (~71%) of GCs did not spike in response to 10-Hz train stimulation of either COM or MPP (Fig. 20A–E) and GCs that spiked exhibited a very low spike probability (ranging from 0 to 0.3). In contrast to GCs, BC-like cells (9 of 9 cells) displayed a high spike probability in response to either COM or MPP stimulation (Fig. 20A). Unlike BC-like cells, HICAP- and HIPP-like cells generated significantly less spikes in response to either COM or MPP stimulation (Fig. 20B,C). TML- and ML-like cells showed strikingly different responses to COM versus MPP stimulation. Both TML- and ML-like cells reliably generated spikes with low failure rates in response to repeated COM stimulation (Fig. 20D,E). In contrast, both TML- and ML-like cells exhibited a low spike probability in response to MPP stimulation (TML-like cells,  $n = 7$  in both COM and MPP groups,  $P < 0.0001$ , two-way repeated-measures ANOVA, Fig. 20D; ML-like cells,  $n = 4$  in the COM group vs.  $n = 5$  in the MPP group,  $P < 0.0001$ , two-way repeated-measures ANOVA, Fig. 20E). Note that ML-like cells preferentially responded to the onset of train stimulation (Fig. 20E).

In summary, our data revealed input-specific recruitment of INs, which is a previously uncharacterized property of these cell types. Notably, the shorter spike delay of TML- and ML-like cells in response to COM stimulation (Fig. 19A) may account for the short EPSC–IPSC latency found at COM–GC synapses compared with MPP–GC synapses (Fig. 11A).

### **Regulation of MPP Input Efficacy by COM Activation**

As summarized in Figure 21A, TML-, ML-, and BC-like cells receive stronger excitatory input from the COM than the MPP. Furthermore, preferential recruitment of TML- and ML-like cells by the

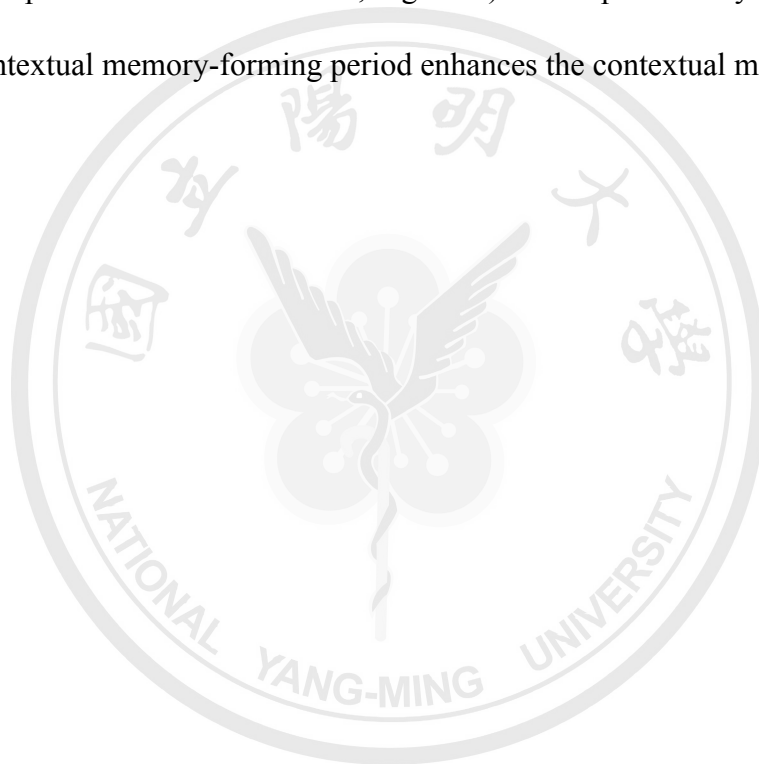


COM, but not by the MPP, likely contributes to the sustained high I/E ratios in GCs during 10-Hz train stimulation of COM (Fig. 11B and Fig. 11D). Here we determined the functional relevance of COM activation on *ex vivo* slice. We performed recordings of field potential in the GCL to monitor the population spike (pSpike) to PP stimulation, the primary excitatory inputs to the DG (containing MPP and lateral PP, Fig. 21B). The pSpike area is regarded as a measure of the number of GCs that spike synchronously to the input stimulus (Temprana et al. 2015). We tested the effect of COM activation at different timing relative to the cortical input on the GC pSpikes at higher temperature. At 34 °C, bursts of 5 electrical shocks at 10 Hz applied to the PP alone elicited pSpikes recorded in the GCL (Fig. 21B, black). Notably, concurrent activation of COM by photostimulation increased the pSpike areas (Fig. 21B, blue and C). In contrast, pSpike areas to PP activation were greatly decreased when the COM was activated 10 ms before the PP (Fig. 21B, light blue and C). Thus, activation of COM at behaviorally relevant frequency can gate cortical information flow, depending on the temporal relationship between the COM and the MPP (Fig. 21C).

### **Enhancement of contextual fear memory by COM activation**

In the final set of experiments, we investigated the functional contribution of COM to the DG in the behavioral aspect. Here we chose a DG-dependent contextual fear memory test (Hernández-Rabaza et al. 2008), which relied on the abilities to recognize a particular environment associated with aversive events that can evoke fear-related responses. *Grik4-cre* mice received AAV5 carrying Cre-inducible ChR2-eYFP (ChR2-eYFP group) or eYFP (eYFP group) injections to one side of DG for targeting COM and an optic fiber implantation in the contralateral DG for subsequent photostimulation of COM (Fig. 22A). At least three weeks later, contextual fear conditioning was conducted. During the entire period of conditioning, 10-Hz photostimulation train was delivered to activate the COM. In the habituation session, both ChR2-eYFP and eYFP groups had no detectable freezing behaviors, suggesting no effect of COM activation to the initial emotional state before foot

shock (Fig. 22B). During 3 trials of foot shock, both 2 groups of mice showed increased freezing levels with repeated foot shocks and had no difference between each other (n =5 in the ChR2-eYFP group vs. n = 3 in the eYFP expressing group,  $P = 0.866$ , two-way repeated-measures ANOVA, Fig. 22B). After 24 hours of fear conditioning, the memory retention test was carry out by placing the mice back to the same contextual chamber and observing the freezing behavior. Interestingly, ChR2-eYFP expressing mice displayed more conditioned freezing than eYFP expressing mice in the 5-min observing time (n =5 in the ChR2-eYFP group vs. n = 3 in the eYFP expressing group,  $P = 0.0132$ , two-way repeated-measures ANOVA, Fig. 22C). These preliminary results suggest COM activation in the contextual memory-forming period enhances the contextual memory expression.



## **Discussion**

### **Summary**

The hilar COM is known to exert a suppressive effect on GC discharge via the activation of local INs in the DG (Buzsáki and Czéh 1981; Buzsáki and Eidelberg 1981; Bilkey and Goddard 1987). To date, the cellular targets of the hilar COM remain mostly unknown. Our study directly addressed this long-lasting question in hippocampal physiology. Using cell type-specific optogenetic tools, we found that COM activation caused substantially greater inhibition in GCs, through preferential recruitment of TML- and ML-like cells compared with MPP activation. We also demonstrated COM can regulate PP input efficacy in recruiting GCs. Finally we showed preliminary results to indicate that COM activation has enhancing effect on contextual memory expression.

### **Drawbacks of Optogenetics in Studying Synaptic Transmission**

The DG integrates information from multiple brain regions, including the entorhinal cortex via the PP, the contralateral hilus via the commissural fibers, the medial septum via the sep- tohippocampal pathway (Bilkey and Goddard 1987), and the SuM via the SuM–hippocampal pathway (Soussi et al. 2010). Relative to input afferents from the entorhinal cortex, investigations of synaptic transmission of hilar MCs and SuM neurons onto GCs are notably scarce. To some extent, the relative neglect of these 2 inputs is explained by the great overlap of their axonal fibers in the IML (Boulland et al. 2009; Soussi et al. 2010; Kohara et al. 2014). It is, therefore, impossible to selectively activate only one of them using conventional electrical stimulation. With selective ChR2 expression in the COM, we were able to stimulate the axonal fibers expressing light-activated channel, ChR2 and dissect its circuit function. However, a potential complication associated with the use of AAV-ChR2 is the artificial synaptic depression reported in some cases (Zhang and Oertner 2007; Cruikshank et al.

2010; Jackman et al. 2014). With our experimental condition, this possibility is minimal and if any, it does not alter the main conclusion. First, we found that synaptic transmission evoked by electrical stimulation at the CA3–CA1 synapse, a well-characterized synapse, exhibits similar dynamics as that evoked by optical stimulation (Fig. 23). These findings are contrary to a recent report by Jackman et al. (2014). Second, fiber volley recordings from the IML showed that 10 Hz photostimulation evokes relatively reliable presynaptic axonal firing with only a transient depression in the initial responses (Fig. 24). Third, the light-evoked, normalized EPSGs (~2-fold) obtained at MPP–ML-like cell synapses (Fig. 17E) in this study are similar to those measured at PP–molecular layer PP-associated cell (MOPP) synapses evoked by electrical stimulation (Li et al. 2013). Finally, if any artificial synaptic depression at COM–IN synapses should be taken into account, our results would rather support the conclusion that the COM, compared with the MPP, can more reliably activate TML- and ML-like cells.

### **Correlations between IN Recruitment and the Dynamics of IN-GC Synaptic Transmission**

Consistent with previous studies using electrical stimulation (Ewell and Jones 2010; Dieni et al. 2013), photostimulation of MPP at 10 Hz caused rapid reduction in IPSGs, resulting in decreases in I/E ratios. Recruitment of specific IN subpopulations by the MPP likely accounts for this depression. As illustrated in Figure 19, photostimulation of MPP reliably recruited BC-like cells, whereas ML-like cells were transiently activated during the onset of 10-Hz train stimulation. Therefore, the initial MPP-driven inhibition onto GCs arises from both IN subpopulations, but the sustained inhibition is solely contributed by BC-like cells. Previous studies (Kraushaar and Jonas 2000; Liu et al. 2014) have shown that the dynamics of BC–GC synapses exhibit frequency-dependent depression. Therefore, those findings explain the rapid reduction in I/E ratios observed in

the present study since BCs are the main contributor to MPP-driven inhibition to GCs under our stimulation paradigm. Contrary to MPP activation, COM stimulation exhibits greater inhibition in GCs, resulting in marked increases in I/E ratios. Notably, COM activation not only recruits BC-like cells, but also reliably recruits TML- and ML-like cells throughout the entire 10-Hz train stimulation. Consistent with the sustained high I/E ratios during spike train, TML-like cell to GC cell synapses exhibited less or no depression at 10 Hz (Fig. 25). Thus, the activation of TML- and ML- like cells during repetitive input activity likely accounts for increasing I/E ratios in COM-driven inhibition.

## **IN Diversity**

It is important to note that not all BC-like cells in this study were identified on the basis of their morphological features. Five of 13 cells were identified as BC-like cells by the characteristic fast-spiking patterns because of incomplete recovery of axonal arborization. Therefore, axo-axonic cells (AACs), which also display high-frequency action potential firing, are likely included in the present study (Weng et al. 2010; Liu et al. 2014). Among all morphological identified fast-spiking INs, we found an AAC-like cell (1/13 cells; see Fig. 26), which displayed the vertical rows of several boutons called “cartridges” along the putative axon initial segment of GCs (Fig. 26B). Likewise, ML-like cells defined here may include MOPP cells and neurogliaform cells. Both of them are shown to form functional synapses with GCs and contribute to feedforward inhibition onto GCs (Armstrong et al. 2011; Li et al. 2013). However, we only identified a single putative neurogliaform cell (1/14 cells), which showed typical axon projections across the fissure into the CA1 region (Armstrong et al. 2011) and was not included in this study. Finally, all INs with their axon projection to the outer ML (OML) in this study were classified as HIPP-like cells. Although original description of HIPP cells found the dendrites restricted in the hilus (Han et al. 1993), our recent study (Liu et al. 2014) showed that a large proportion of HIPP-like cells, which project their axons

to the OML, have the dendritic arbor in the ML [also see Hosp et al. (2014)]. In keeping with this notion, we observed that all HIPP-like cells (10 cells) in this study extend their dendrites outside the hilus to the ML. Furthermore, it is interesting that synaptic efficacy of layer-specific input (COM and MPP) in HIPP-like cells positively correlates with its dendritic distribution in the afferent input layer (Fig. 27)

### **Pathway-Specific Recruitment of IN Types**

Our results show that various IN types (except BC-like cells) are differentially activated by different afferent pathways, suggesting that different IN types selectively mediate segregation of information flow. It seems that reliable recruitment of BC-like cells by both COM and MPP is ascribed to the strong excitatory drive, which overcomes the poor synaptic integration properties (Hu et al. 2014). It is worth noting that HIPP- and HICAP-like cells exert highly dynamic inhibition onto dendritic parts of GCs (Liu et al. 2014). They generate weak inhibition onto GCs when they fire sparsely. However, they generate powerful and reliable inhibitory output when they are switched from the single to the burst spiking mode (Liu et al. 2014). This gives rise to an interesting question: How are HIPP- and HICAP-like cells activated in the context of extrinsic afferent systems? To answer this question, systematic investigations of other subcortical afferents to these INs are indispensable. These systems mainly include afferents originating from the medial septum/diagonal band of Broca GABAergic and cholinergic neurons, neurochemically distinct types of neurons located in the SuM area, serotonergic fibers from the median raphe, noradrenergic afferents from the pontine nucleus and locus coeruleus, dopamine axons originating in the ventral tegmental area, and the commissural projection system (Leranth and Hajszan 2007). Overall, extrahippocampal and intrahippocampal excitatory input-specific recruitment of certain IN subpopulations may underscore a “division of labor” in cortical circuits, where distinct computational functions are implemented by various types of local inhibitory INs.

## Limitations of COM Targeting in the Present Study

It is also important to point out that some limitations exist in the present study for the understanding of COM-mediated neuro- transmission. First, selective COM targeting depends on the efficacy of the *Grik4-cre* mouse line and Cre-dependent expression of AAV-ChR2. Interestingly, a previous study reports that calretinin-negative MCs in the dorsal DG are preferentially manipulated by this method, whereas the ventral calretinin-positive MCs are less affected (Nakazawa et al. 2002). It is also noted that MCs not only exhibit the difference in calretinin immunoreactivity along the dorsoventral axis, but also vary in complexity of thorny excrescences, synaptic responses, and their intrinsic properties (Blasco-Ibáñez and Freund 1997; Fujise et al. 1998; Jinno et al. 2003). These observations suggest that different MC subpopulations along the axis might play various physiological roles. To further elaborate the functional characteristics of the COM, targeting MCs using different Cre lines, for example, the MC/CA3-cre #4688 line (Jinde et al. 2012), may be helpful in further specifying the function of COM-mediated transmission. Second, most of our study focused on COM-mediated transmission to the contralateral dorsal DG, although we noted that the COM projects along the entire longitudinal axis of the contralateral DG. Whether the synaptic transmission of COM–ventral DG and COM–dorsal DG differs functionally remains an interesting question. Moreover, the functions of the hippocampus are not equal along the hippocampal longitudinal axis (Strange et al. 2014). For example, there is a gradual enlargement of place-field scale along the dorsoventral axis (Kjelstrup et al. 2008). Therefore, the role of the COM in coordinating different functional modalities in different hippocampal transverse units demands extensive investigations.

Despite the above-mentioned limitations, our study provides evidence about the source of COM-mediated inhibitory control over GCs and supports the *in vivo* observation that GCs exhibit

hyperexcitability in response to PP stimulation after MCs were ablated extensively throughout the entire longitudinal axis (Jinde et al. 2012). Some functional correlations were associated with hyperexcitable GCs, including increased theta power of DG local field potentials, elevated anxiety, and impaired contextual discrimination (Jinde et al. 2012). Further experiments using temporally precise tools to excite or silence the COM in vivo during behavioral tasks are required.

## **Discussion on the Functional Role of COM in Cognitive Level**

Our preliminary results indicated that COM activation will strengthen contextual memory formation. However, a potential complication associated with *in vivo* optogenetic excitation of COM might happen. Although the implanted optic fiber was used to activate the ChR2 positive COM, there is a certain chance that the depolarizing effect mediated by ChR2 could propagate antidromically back to MC's soma and then activate associational pathway, as well as local axons projected within the same transverse axis. Therefore, the enhancement of contextual memory might be due to the activation of all MC's axonal projections. To specifically study the function of COM pathway in behavioral aspect and rule out the complication mentioned above, the complementary "loss of function" manipulations of COM are required. For example, there are several kinds of inhibitory optogenetic tools which conduct hyperpolarizing or shunting effect on neuronal activity, such as light sensitive-Cl<sup>-</sup> pump enhanced halorhodopsin 3.0 (Gradinaru et al. 2010), proton pump archaerhodopsin-3 (Chow et al. 2010) and Cl<sup>-</sup> channel iClC2 (Berndt et al. 2014). The silencing effect of inhibitory optogenetic tools on COM axon terminals by over-axon or over-bouton photostimulation must be confirmed first. If one kind of inhibitory optogenetic tool can specifically inhibit COM-mediated synaptic transmission without affecting other projections originated from MC, it can be used in studying the function of COM pathways in cognitive level. Alternatively, other kind of "loss of function" approach, the chemogenetic DREADD (designer receptor exclusively activated by designer drug) can also be considered. This chemogenetic approach relies



on selective expression of human mutant M4-muscarinic receptor (hM4Di) on MCs. By local infusion of the hM4Di agonist clozapine N-oxide to the COM, it is possible to selectively silence COM-mediated transmission due to reduction of cyclic adenosine monophosphate level or  $\beta/\gamma$ -G protein-coupled inwardly-rectifying potassium channel activation (Sternson and Roth 2014).

The contextual fear memory test didn't directly reflect some cognitive functions of DG. Therefore, the enhancement of contextual fear memory by activating COM can be explained in a variety of ways. To further clarify the distinct effects of COM, several specific experiments should be done. First, it is possible that COM activation provides more inhibitory control to maintain sparse activities of GCs, thereby enhancing the pattern separation ability of DG. To prove this, the contextual discrimination tasks in which the mice learn to discriminate a pair of very similar contexts could be conducted (Nakashiba et al. 2012; Jinde et al. 2012). Furthermore, the degree of sparse firing of GCs can be examined by c-Fos staining after the mice completed the behavioral tasks (Ramirez et al. 2013). Alternatively, enhancement of contextual fear memory by COM activation could also be explained by increasing "pattern completion" ability, which is mediated by mature GC-CA3 transmission (Nakashiba et al. 2012). Pattern completion is involved in the recall of previously obtained memory by utilizing partial information as recall cues. To test the pattern completion ability, a water maze task with varying degrees of cue availability can be used (Nakashiba et al. 2012). Finally, it is interesting to know whether COM activation potentiates the plasticity change due to contextual conditioning, thereby enhancing the behavior reflecting contextual memory retention. It has been known that the long term potentiation (LTP) between GC-MC and MC-GC synapses enhanced the synaptic transmission from GC to CA3, bypassing the NMDA receptor-independent LTP of local CA3 mossy fiber synapses (Wright and Jackson 2014). By selective knockout of NMDA receptor and delivering optogenetic tools to the MC, this hypothesis could be tested on behavioral aspect.

## References

- Alme CB, Buzzetti RA, Marrone DF, Leutgeb JK, Chawla MK, Schaner MJ, Bohanick JD, Khoboko T, Leutgeb S, Moser EI, et al. 2010. Hippocampal granule cells opt for early retirement. *Hippocampus*. 20:1109–1123.
- Armstrong C, Szabadics J, Tamás G, Soltesz I. 2011. Neurogliaform cells in the molecular layer of the dentate gyrus as feed-forward  $\gamma$ -aminobutyric acidergic modulators of entorhinal-hippocampal interplay. *J Comp Neurol*. 519:1476–1491.
- Banks MI, White JA, Pearce RA. 2000. Interactions between distinct GABAA circuits in hippocampus. *Neuron*. 25:449–457.
- Bartos M, Alle H, Vida I. 2011. Role of microcircuit structure and input integration in hippocampal interneuron recruitment and plasticity. *Neuropharmacology*. 60:730–739.
- Behr J, Lyson KJ, Mody I. 1998. Enhanced propagation of epileptiform activity through the kindled dentate gyrus. *J Neurophysiol*. 79:1726–1732.
- Berndt A, Lee SY, Ramakrishnan C, Deisseroth K. 2014. Structure-guided transformation of a channelrhodopsin into a light-activated chloride channel. *Science*. 344:420–424.
- Bilkey DK, Goddard GV. 1987. Septohippocampal and commissural pathways antagonistically control inhibitory interneurons in the dentate gyrus. *Brain Res*. 405:320–325.

- Blasco-Ibáñez JM, Freund TF. 1997. Distribution, ultrastructure, and connectivity of calretinin-immunoreactive mossy cells of the mouse dentate gyrus. *Hippocampus*. 7:307–320.
- Bliss TV, Lomo T. 1973. Long-lasting potentiation of synaptic transmission in the dentate area of the anaesthetized rabbit following stimulation of the perforant path. *J Physiol*. 232:331–356.
- Boulland JL, Jenstad M, Boekel AJ, Wouterlood FG, Edwards RH, Storm-Mathisen J, Chaudhry FA. 2009. Vesicular glutamate and GABA transporters sort to distinct sets of vesicles in a population of presynaptic terminals. *Cereb Cortex*. 19:241–248.
- Boyden ES, Zhang F, Bamberg E, Nagel G, Deisseroth K. 2005. Millisecond-timescale, genetically targeted optical control of neural activity. *Nat Neurosci*. 8:1263–1268.
- Buckmaster PS, Wenzel HJ, Kunkel DD, Schwartzkroin PA. 1996. Axon arbors and synaptic connections of hippocampal mossy cells in the rat in vivo. *J Comp Neurol*. 366:271–292.
- Buhl EH, Szilágyi T, Halasy K, Somogyi P. 1996. Physiological properties of anatomically identified basket and bistratified cells in the CA1 area of the rat hippocampus in vitro. *Hippocampus*. 6:294–305.
- Buzsáki G, Czéh G. 1981. Commissural and perforant path interactions in the rat hippocampus. Field potentials and unitary activity. *Exp Brain Res*. 43:429–438.
- Buzsáki G, Eidelberg E. 1981. Commissural projection to the dentate gyrus of the rat: evidence for feed-forward inhibition. *Brain Res*. 230:346–350.

- Chancey JH, Poulsen DJ, Wadiche JI, Overstreet-Wadiche L. 2014. Hilar mossy cells provide the first glutamatergic synapses to adult-born dentate granule cells. *J Neurosci.* 34:2349–2354.
- Chiang PH, Wu PY, Kuo TW, Liu YC, Chan CF, Chien TC, Cheng JK, Huang YY, Chiu CD, Lien CC. 2012. GABA is depolarizing in hippocampal dentate granule cells of the adolescent and adult rats. *J Neurosci.* 32:62–67.
- Chow BY1, Han X, Dobry AS, Qian X, Chuong AS, Li M, Henninger MA, Belfort GM, Lin Y, Monahan PE, et al. 2010. High-performance genetically targetable optical neural silencing by light-driven proton pumps. *Nature.* 463:98–102.
- Collingridge GL, Singer W. 1990. Excitatory amino acid receptors and synaptic plasticity. *Trends Pharmacol Sci.* 11:290–296.
- Coulter DA, Carlson GC. 2007. Functional regulation of the dentate gyrus by GABA-mediated inhibition. *Prog Brain Res.* 163:235–243.
- Crick FH. 1979. Thinking about the brain. *Sci. Am.* 241:219–232.
- Cruikshank SJ, Urabe H, Nurmikko AV, Connors BW. 2010. Pathway-specific feedforward circuits between thalamus and neocortex revealed by selective optical stimulation of axons. *Neuron.* 65:230–245.
- Dieni CV, Nietz AK, Panichi R, Wadiche JI, Overstreet-Wadiche L. 2013. Distinct determinants of sparse activation during granule cell maturation. *J Neurosci.* 33:19131–19142.

- Dittgen T, Nimmerjahn A, Komai S, Licznarski P, Waters J, Margrie TW, Helmchen F, Denk W, Brecht M, Osten P. 2004. Lentivirus- based genetic manipulations of cortical neurons and their optical and electro- physiological monitoring *in vivo*. *Proc. Natl. Acad. Sci. USA.* 101:18206–18211.
- Ewell LA, Jones MV. 2010. Frequency-tuned distribution of inhibition in the dentate gyrus. *J Neurosci.* 30:12597–12607.
- Freund TF, Buzsáki G. 1996. Interneurons of the hippocampus. *Hippocampus.* 6:347–470.
- Fujise N, Liu Y, Hori N, Kosaka T. 1998. Distribution of calretinin immunoreactivity in the mouse dentate gyrus: II. Mossy cells, with special reference to their dorsoventral difference in calretinin immunoreactivity. *Neuroscience.* 82:181–200.
- Gradinaru V, Zhang F, Ramakrishnan C, Mattis J, Prakash R, Diester I, Goshen I, Thompson K, Deisseroth K. 2010. Molecular and Cellular Approaches for Diversifying and Extending Optogenetics. *Cell.* 141:154–165.
- Hafting T, Fyhn M, Molden S, Moser MB, Moser EI. 2005. Microstructure of a spatial map in the entorhinal cortex. *Nature.* 436:801–806.
- Han ZS, Buhl EH, Lörinczi Z, Somogyi P. 1993. A high degree of spatial selectivity in the axonal and dendritic domains of physiologically identified local-circuit neurons in the dentate gyrus of the rat hippocampus. *Eur J Neurosci.* 5:395–410.

- Harris EW, Cotman CW. 1986. Long-term potentiation of guinea pig mossy fiber responses is not blocked by N-methyl D-aspartate antagonists. *Neurosci Lett.* 25:132–137.
- Hernández-Rabaza V, Hontecillas-Prieto L, Velázquez-Sánchez C, Ferragud A, Pérez-Villaba A, Arcusa A, Barcia JA, Trejo JL, Canales JJ. 2008. The hippocampal dentate gyrus is essential for generating contextual memories of fear and drug-induced reward. *Neurobiol Learn Mem.* 90:553–559.
- Hosp JA, Strüber M, Yanagawa Y, Obata K, Vida I, Jonas P, Bartos M. 2014. Morpho-physiological criteria divide dentate gyrus interneurons into classes. *Hippocampus.* 24:189–203.
- Hu H, Gan J, Jonas P. 2014. Interneurons. Fast-spiking, parvalbumin<sup>+</sup> GABAergic interneurons: from cellular design to microcircuit function. *Science.* 345:1255–1263.
- Hurst JL, West RS. 2010. Taming anxiety in laboratory mice. *Nat Methods.* 7:825–826.
- Jackman SL, Beneduce BM, Drew IR, Regehr WG. 2014. Achieving high-frequency optical control of synaptic transmission. *J Neurosci.* 34:7704–7714.
- Jinde S, Zsiros V, Jiang Z, Nakao K, Pickel J, Kohno K, Belforte JE, Nakazawa K. 2012. Hilar mossy cell degeneration causes transient dentate granule cell hyperexcitability and impaired pattern separation. *Neuron.* 76:1189–1200.
- Jinno S, Ishizuka S, Kosaka T. 2003. Ionic currents underlying rhythmic bursting of ventral mossy cells in the developing mouse dentate gyrus. *Eur J Neurosci.* 17:1338–1354.

- Kafri T. 2004. Gene delivery by lentivirus vectors an overview. *Methods Mol Biol.* 246:367–90.
- Khurana S, Remme MW, Rinzel J, Golding NL. 2011. Dynamic interaction of Ih and IK-LVA during trains of synaptic potentials in principal neurons of the medial superior olive. *J Neurosci.* 31:8936–8947.
- Kjelstrup KB, Solstad T, Brun VH, Hafting T, Leutgeb S, Witter MP, Moser EI, Moser MB. 2008. Finite scale of spatial representation in the hippocampus. *Science.* 321:140–143.
- Kohara K, Pignatelli M, Rivest AJ, Jung HY, Kitamura T, Suh J, Frank D, Kajikawa K, Mise N, Obata Y, et al. 2014. Cell type-specific genetic and optogenetic tools reveal hippocampal CA2 circuits. *Nat Neurosci.* 17:269–279.
- Kraushaar U, Jonas P. 2000. Efficacy and stability of quantal GABA release at a hippocampal interneuron-principal neuron synapse. *J Neurosci.* 20:5594–5607.
- Krueppel R, Remy S, Beck H. 2011. Dendritic integration in hippocampal dentate granule cells. *Neuron.* 71:512–528
- Lee S, Kruglikov I, Huang ZJ, Fishell G, Rudy B. 2013. A disinhibitory circuit mediates motor integration in the somatosensory cortex. *Nat Neurosci.* 16:1662–1670.
- Leranth C, Hajszan T. 2007. Extrinsic afferent systems to the dentate gyrus. *Prog Brain Res.* 163:63–84.

- Leutgeb JK, Leutgeb S, Moser MB, Moser EI. 2007. Pattern separation in the dentate gyrus and CA3 of the hippocampus. *Science*. 315:961–966.
- Li Y, Stam FJ, Aimone JB, Goulding M, Callaway EM, Gage FH. 2013. Molecular layer perforant path-associated cells contribute to feed-forward inhibition in the adult dentate gyrus. *Proc Natl Acad Sci USA*. 110:9106–9111.
- Liu YC, Cheng JK, Lien CC. 2014. Rapid dynamic changes of dendritic inhibition in the dentate gyrus by presynaptic activity patterns. *J Neurosci*. 34:1344–1357.
- Maccaferri G, Dingledine R. 2002. Control of feedforward dendritic inhibition by NMDA receptor-dependent spike timing in hippocampal interneurons. *J Neurosci*. 22:5462–5472.
- McFarland NR, Lee JS, Hyman BT, McLean PJ. 2009. Comparison of transduction efficiency of recombinant AAV serotypes 1, 2, 5, and 8 in the rat nigrostriatal system. *J Neurochem*. 109:838–845.
- McHugh TJ, Jones MW, Quinn JJ, Balthasar N, Coppari R, Elmquist JK, Lowell BB, Fanselow MS, Wilson MA, Tonegawa S. 2007. Dentate gyrus NMDA receptors mediate rapid pattern separation in the hippocampal network. *Science*. 317:94–99.
- Monahan PE, Samulski RJ. 2000. Adeno-associated virus vectors for gene therapy: more pros than cons? *Mol. Med. Today* 6:433–440.



- Mott DD, Turner DA, Okazaki MM, Lewis DV. 1997. Interneurons of the dentate-hilus border of the rat dentate gyrus: morphological and electrophysiological heterogeneity. *J Neurosci.* 17:3990–4005.
- Muller RU, Kubie JL, Bostock EM, Taube JS, Quirk GJ. 1991. In *Brain and Space* (Oxford: Oxford University Press). 296–333.
- Nakazawa K, Quirk MC, Chitwood RA, Watanabe M, Yeckel MF, Sun LD, Kato A, Carr CA, Johnston D, Wilson MA, et al. 2002. Requirement for hippocampal CA3 NMDA receptors in associative memory recall. *Science.* 297:211–218.
- O'Keefe J, Dostrovsky J. 1971. The hippocampus as a spatial map. Preliminary evidence from unit activity in the freely-moving rat. *Brain Res.* 34:171–175.
- Pathak HR, Weissinger F, Terunuma M, Carlson GC, Hsu FC, Moss SJ, Coulter DA. 2007. Disrupted dentate granule cell chloride regulation enhances synaptic excitability during development of temporal lobe epilepsy. *J Neurosci.* 27:14012–14022.
- Pernía-Andrade AJ, Jonas P. 2014. Theta-gamma-modulated synaptic currents in hippocampal granule cells in vivo define a mechanism for network oscillations. *Neuron.* 81:140–152.
- Ramon y Cajal, S. 1911. *Histologie du Système Nerveux de l'Homme et des Vertébrés, Volume II.* Paris: Maloine.

- Sargolini F, Fyhn M, Hafting T, McNaughton BL, Witter MP, Moser MB, Moser EI. 2006. Conjunctive representation of position, direction, and velocity in entorhinal cortex. *Science*. 312:758–762.
- Scharfman HE, Myers CE. 2013. Hilar mossy cells of the dentate gyrus: a historical perspective. *Front Neural Circuits*. 6:106.
- Schmidt-Hieber C, Jonas P, Bischofberger J. 2004. Enhanced synaptic plasticity in newly generated granule cells of the adult hippocampus. *Nature*. 429:184–187.
- Schmidt-Hieber C, Jonas P, Bischofberger J. 2007. Subthreshold dendritic signal processing and coincidence detection in dentate gyrus granule cells. *J Neurosci*. 27:8430–8441.
- Scoville WB, Milner B. 1957. Loss of recent memory after bilateral hippocampal lesions. *J Neurol Neurosurg Psychiatry*. 20:11–21.
- Solstad T, Boccara CN, Kropff E, Moser MB, Moser EI. 2008. Representation of geometric borders in the entorhinal cortex. *Science*. 322:1865–1868.
- Soriano E, Frotscher M. 1993. GABAergic innervation of the rat fascia dentata: a novel type of interneuron in the granule cell layer with extensive axonal arborization in the molecular layer. *J Comp Neurol*. 334:385–396.
- Soriano E, Frotscher M. 1994. Mossy cells of the rat fascia dentata are glutamate-immunoreactive. *Hippocampus*. 4:65–69.

- Soussi R, Zhang N, Tahtakran S, Houser CR, Esclapez M. 2010. Heterogeneity of the supramammillary-hippocampal pathways: evidence for a unique GABAergic neurotransmitter phenotype and regional differences. *Eur J Neurosci.* 32:771–785.
- Sternson SM, Roth BL. 2014. Chemogenetic tools to interrogate brain functions. *Annu Rev Neurosci.* 37:387–407.
- Strange BA, Witter MP, Lein ES, Moser EI. 2014. Functional organization of the hippocampal longitudinal axis. *Nat Rev Neurosci.* 15:655–669.
- Taube JS, Muller RU, Ranck JB Jr. 1990. Head-direction cells recorded from the postsubiculum in freely moving rats. II. Effects of environmental manipulations. *J Neurosci.* 10:436–447.
- Temprana SG, Mongiat LA, Yang SM, Trincherro MF, Alvarez DD, Kropff E, Giacomini D, Beltramone N, Lanuza GM, Schinder AF. 2015. Delayed coupling to feedback inhibition during a critical period for the integration of adult-born granule cells. *Neuron.* 85:116–130.
- Vivar C, Potter MC, Choi J, Lee JY, Stringer TP, Callaway EM, Gage FH, Suh H, van Praag H. 2012. Monosynaptic inputs to new neurons in the dentate gyrus. *Nat Commun.* 3:1107.
- Weng JY, Lin YC, Lien CC. 2010. Cell type-specific expression of acid-sensing ion channels in hippocampal interneurons. *J Neurosci.* 30:6548–6558.
- West JR, Nornes HO, Barnes CL, Bronfenbrenner M. 1979. The cells of origin of the commissural afferents to the area dentata in the mouse. *Brain Res.* 160:203–215.

- Wright BJ, Jackson MB. 2014. Long-term potentiation in hilar circuitry modulates gating by the dentate gyrus. *J neurosci.* 34:9743–9753.
- Yizhar O, Fenno LE, Davidson TJ, Mogri M, Deisseroth K. 2011. Optogenetics in neural systems. *Neuron.* 71:9–34.
- Zhang F, Wang LP, Brauner M, Liewald JF, Kay K, Watzke N, Wood PH, Bamberg E, Nagel G, Gottschalk A, et al. 2007. Multimodal fast optical interrogation of neural circuitry. *Nature.* 446:633–639.
- Zhang F, Gradinaru V, Adamantidis AR, Durand R, Airan RD, de Lecea L, Deisseroth K. 2010. Optogenetic interrogation of neural circuits: technology for probing mammalian brain structures. *Nat Protoc.* 5:439–456.
- Zhang SJ, Ye J, Miao C, Tsao A, Cerniauskas I, Ledergerber D, Moser MB, Moser EI. 2013. Optogenetic dissection of entorhinal-hippocampal functional connectivity. *Science.* 340:1232627.
- Zhang YP, Oertner TG. 2007. Optical induction of synaptic plasticity using a light-sensitive channel. *Nat Methods.* 4:139–141.
- Zola-Morgan S, Squire LR, Amaral DG. 1986. Human amnesia and the medial temporal region: enduring memory impairment following a bilateral lesion limited to field CA1 of the hippocampus. *J Neurosci.* 6:2950–2967.

## Figures and Tables

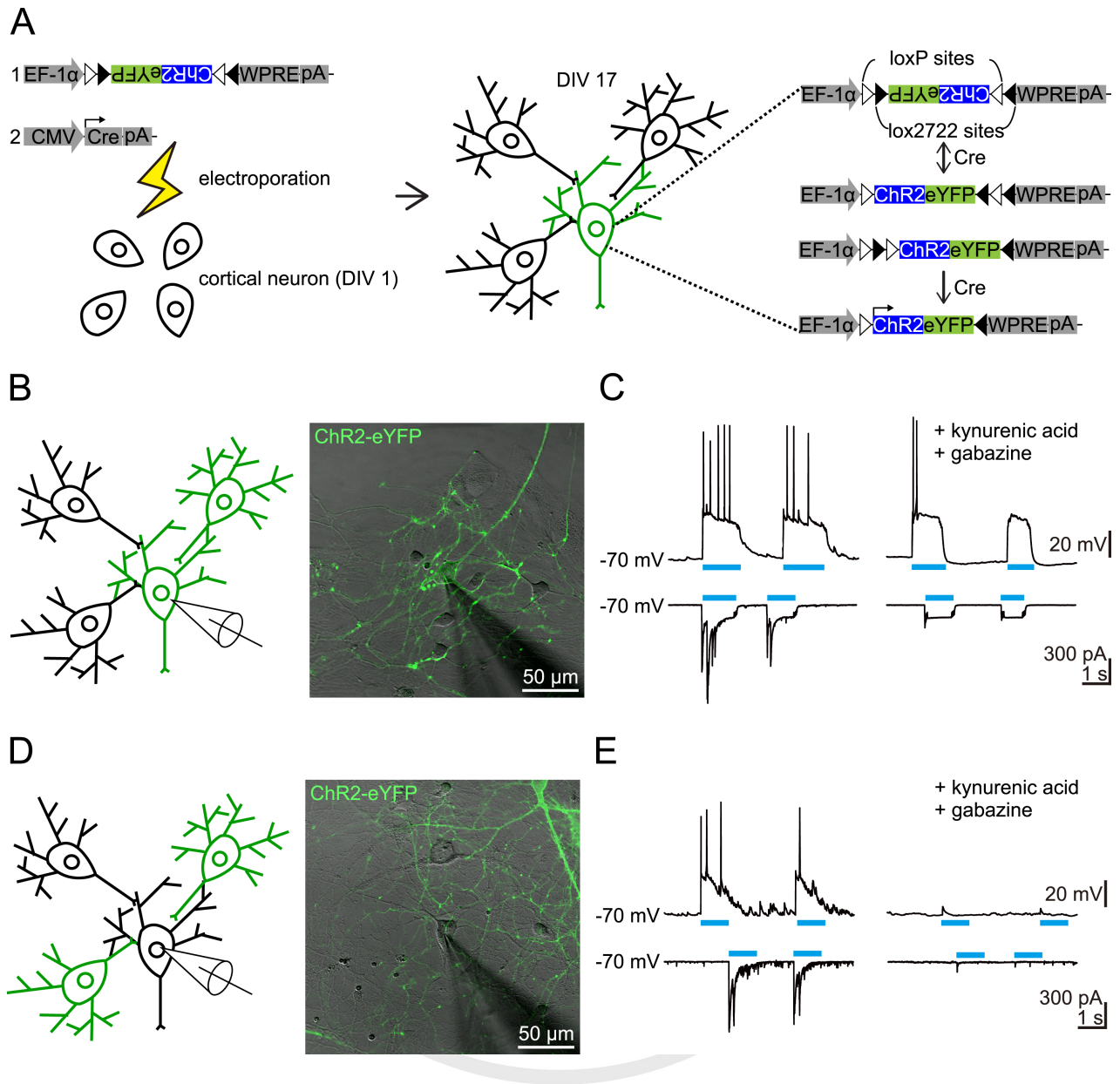


**Figure 1. Functional examination of Cre-inducible ChR2 construct on cultured rat cortical neurons.**

(A) Schematic of experiment configuration: co-electroporation of transgene construct (1) together with a Cre-expressing construct (2) into rat cortical neurons at DIV1 (left). Examination of ChR2 function was carried out on DIV17 (middle), when the Cre-mediated activation of the double-

floxed-inverse ChR2-EYFP transgene has happened on ChR2-eYFP expressing neuron (green, right).

(B) Schematic (left) and image (right) depict recording of a ChR2-eYFP positive neuron (green).

(C) Light illumination (blue bars) evoked spikes in the ChR2-eYFP positive neuron (shown in B) in current clamp mode, membrane voltage is indicated (top left). ChR2-mediated photocurrent together with synaptic responses were recorded in voltage clamp (held at  $-70$  mV) upon light illumination (bottom left). Blocking of synaptic activities by kynurenic acid (2 mM) and gabazine (1  $\mu$ M) revealed pure ChR2-mediated depolarization (top right) and inward current (bottom right).

(D) Schematic (left) and image (right) depict recording of a ChR2-eYFP negative neuron.

(E) Light illumination (blue bars) evoked synaptic depolarization and generate spikes in the ChR2-eYFP negative neuron (shown in D) in current clamp mode (top left), as well as synaptic currents (bottom right) recorded in voltage clamp (held at  $-70$  mV). Synaptic responses were abolished by synaptic blockers.

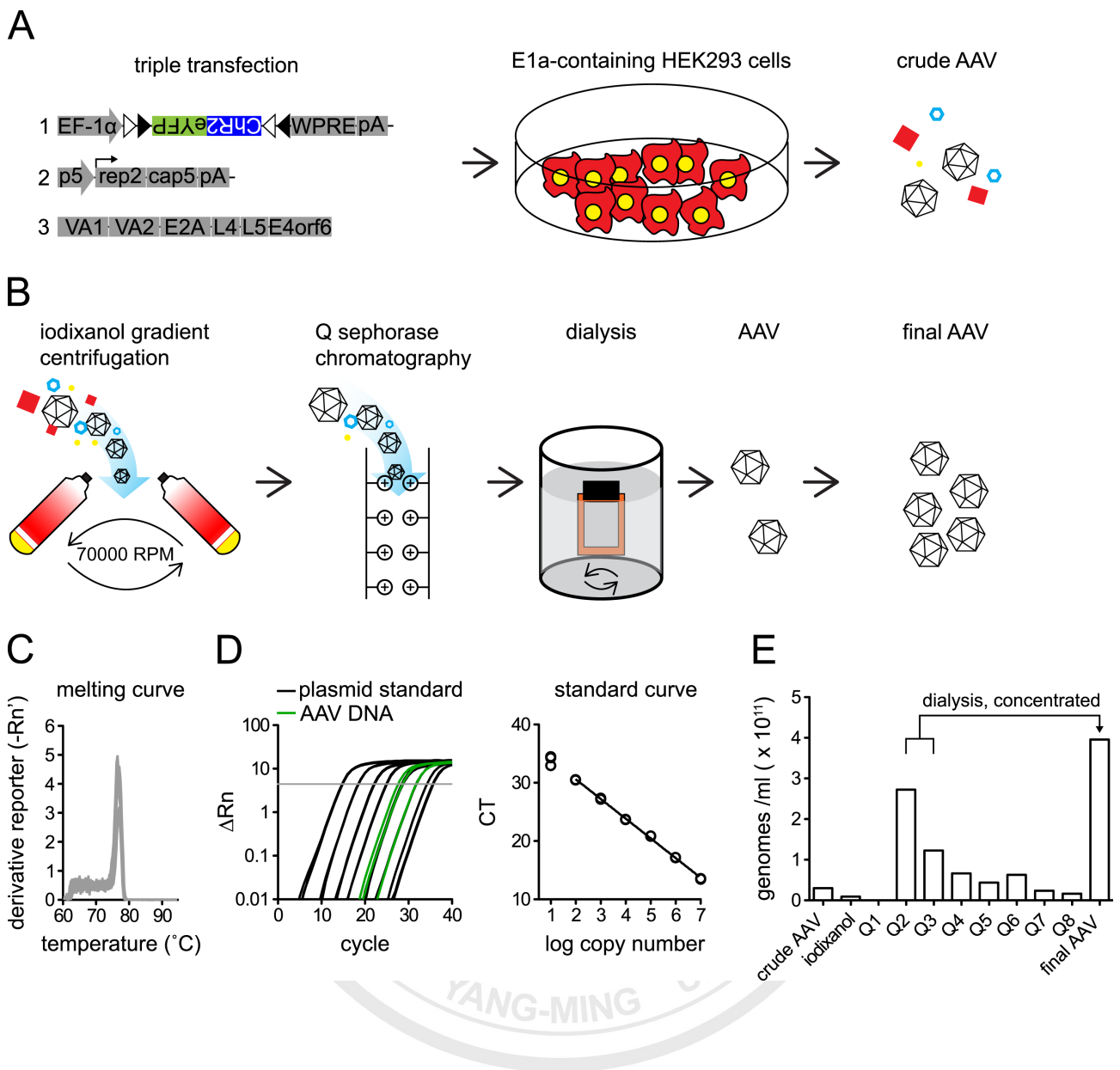


**Figure 2. Generation of AAV5.**

(A) Schematic depicts production of AAV5. Transgene construct (1), AAV5 packaging construct (2) and adenoviral helper construct (3) were triple-transfected into E1a-containing HEK293 cells. After 48-56 hrs, crude AAV soup was obtained by breaking down the E1a-containing HEK293 cells.

(B) Schematic depicts purification and concentration of AAV5. The process started from iodixanol gradient centrifugation, followed by Q sepharose chromatography. After dialysis of processed

AAV5 against PBS with  $\text{CaCl}_2$  and  $\text{MgCl}_2$ , a concentrating step was conducted to yield the final AAV5.

(C) Melting curve analysis of quantitative realtime PCR product using plasmid standard and AAV DNA as templates.

(D) Left, an amplification plot of plasmid standards (black) and AAV DNA (green). The fluorescence threshold was set in the exponential phase of the amplification curve by the software, and the threshold cycle (CT) was determined by the intersection of the amplification curve with the fluorescence threshold. The precision of realtime PCR was estimated by the standard deviation of CT in each data set (with 3 replicates). The data would be excluded if the standard deviation  $> 0.167$  CT. Right, Standard curve was plotted with log-transformed initial plasmid copy number against CT, and fitted with linear regression.  $R^2$  value of the linear fitting should be larger than 0.99. The slope of the fitting line was used to calculate PCR efficiency. The equation of the fitting line was used to estimate the AAV titer.

(E) Summary bar graph showed viral titer of in-process and final AAV. Note the 2 fractions (Q2, Q3) eluted from Q sepharose chromatography with high titer were pooled together, dialyzed and concentrated, yielding the final AAV5.



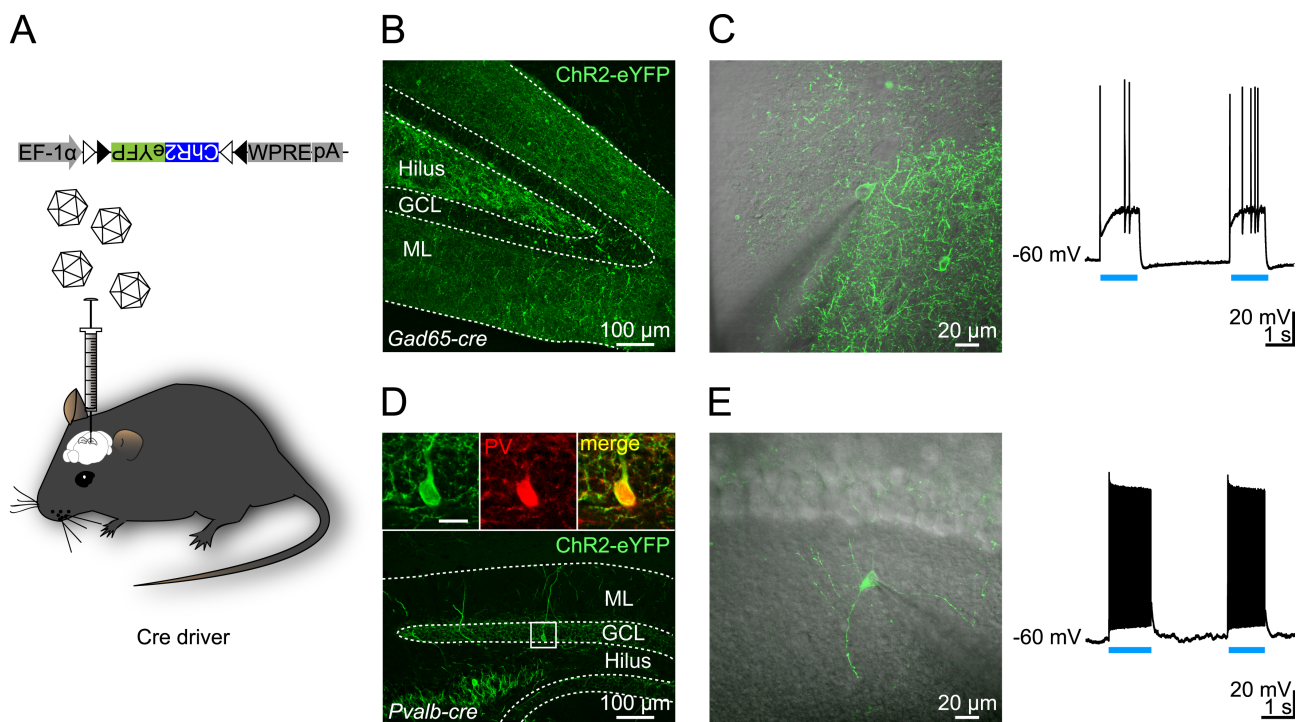


**Figure 3. Functional examination of AAV5 carrying Cre-inducible ChR2-eYFP.**

(A) Injection of AAV5-EF1 $\alpha$ -DIO-ChR2-eYFP into dorsal hippocampus of Cre drivers.

(B–C) Functional expression of ChR2-eYFP on INs of *Gad65-cre* mouse. (B) Fluorescence image of ChR2-eYFP expression (green) in the dorsal hippocampus of *Gad65-cre* mouse. (C) Whole-cell recording of a ChR2-eYFP positive IN in the ML of DG. Light illumination (blue bars) elicited spikes of recorded IN.

(D–E) Functional expression of ChR2-eYFP on fast spiking INs of *Pvalb-cre* mouse. (D) Fluorescence image of ChR2-eYFP expression (green) in the dorsal hippocampus of *Pvalb-cre* mouse. The boxed area is shown at a higher magnification in the inset, indicating coexpression of ChR2-eYFP and PV (red). (E) Whole-cell recording of a ChR2-eYFP positive IN in the CA1 Stratum radiatum. Light illumination (blue bars) evoked fast spiking of recorded IN.

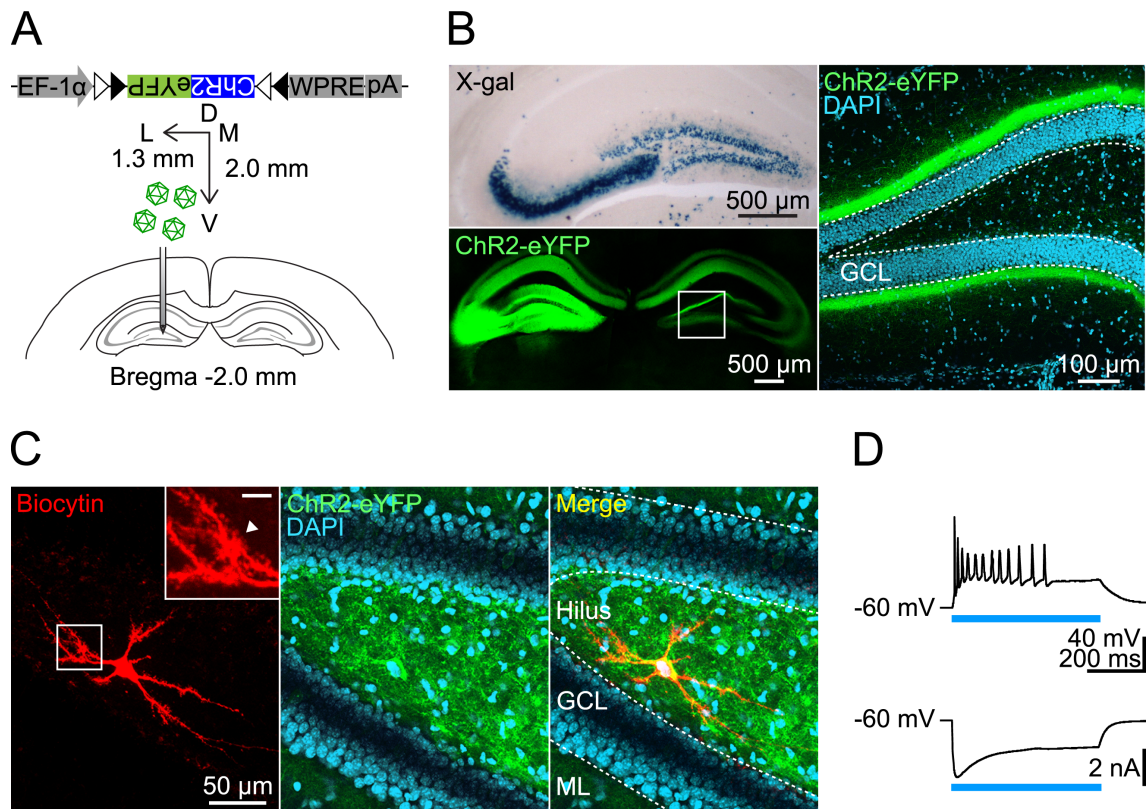


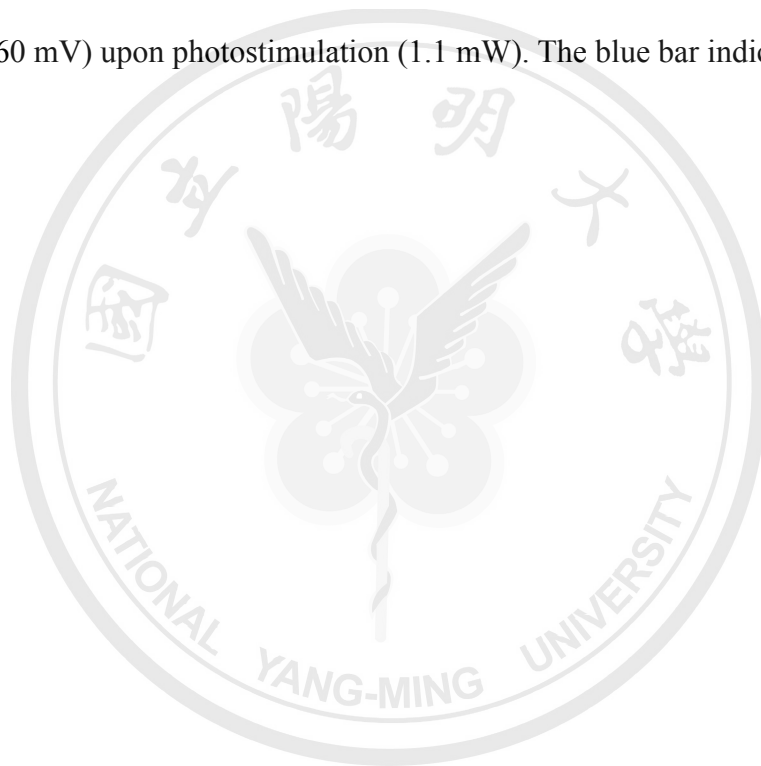
**Figure 4. ChR2 expression in the COM to the DG.**

(A) Schematic diagram illustrates a coronal section from a *Grik4-cre* mouse injected unilaterally with a viral vector AAV5-EF1 $\alpha$ -DIO-ChR2-eYFP into the hilar region of the dorsal hippocampus. Axis: L, lateral; V, ventral; M, medial; D, dorsal.

(B) Left upper, coronal section stained with X-gal from the dorsal hippocampus of *Grik4-cre* mice crossed with the loxP-flanked *Rosa26LacZ* reporter line. Left lower, fluorescence image of ChR2-eYFP expression in the dorsal hippocampus; the boxed area is shown at a higher magnification on the right. The borders of the GCL are outlined. Note the laminated ChR2-eYFP expression in the IML of the contralateral DG. DAPI staining defines the area of the GCL.

(C) Left, the morphology of a biocytin-filled MC. The boxed area is shown at a higher magnification in the inset; arrowhead indicates the thorny excrescences; scale bar in the inset: 10  $\mu\text{m}$ . Middle, fluorescence image of ChR2-eYFP expression in the hilar region. Right, the merged image. DAPI staining defines the area of the GCL.

(D) Top, photostimulation (0.8 mW) evoked spikes in an MC (shown in C) in current clamp. Membrane voltage is indicated. Bottom, ChR2-mediated photocurrent was recorded in voltage clamp (held at  $-60$  mV) upon photostimulation (1.1 mW). The blue bar indicates the light pulse.



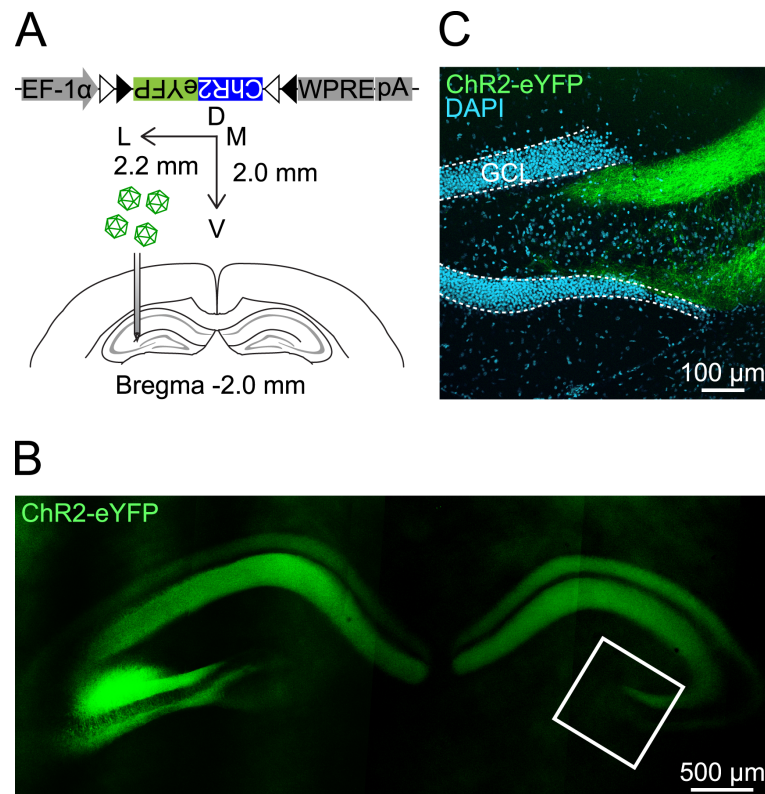


### Figure 5. Selective ChR2 expression in CA3 neurons.

(A) Schematic diagram illustrates unilateral injection of a viral vector AAV5-EF1 $\alpha$ -DIO-ChR2-eYFP into the CA3 region of the dorsal hippocampus.

(B–C) Fluorescence image of ChR2-eYFP expression in the dorsal hippocampus. (B) The injection site is restricted in the CA3 region of the left dorsal hippocampus. The boxed area is shown at a higher magnification in (C) ChR2-eYFP expression (green) in the strata radiatum and oriens of the CA3 region and GCs are labeled with DAPI. The borders of the GCL are outlined. Note the lack of ChR2-eYFP expression in the IML of the contralateral DG.

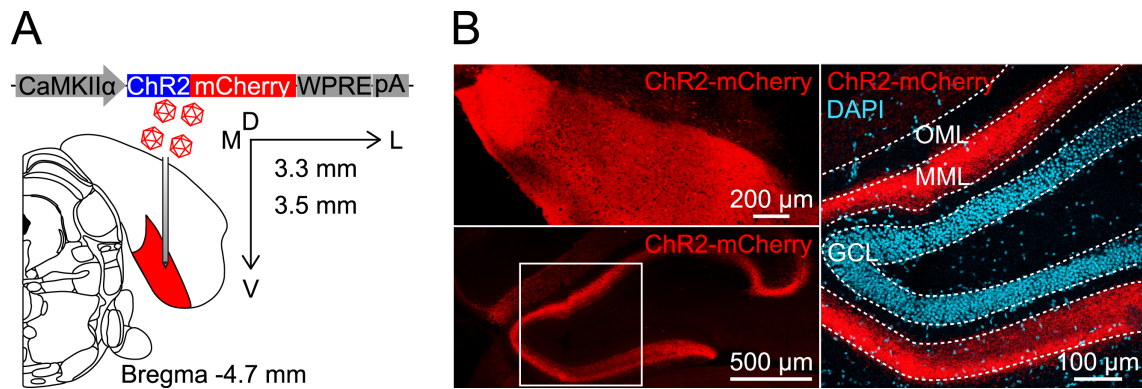


**Figure 6. ChR2 expression in the MPP to the DG.**

- (A) Schematic diagram illustrates a coronal section from a wild-type mouse injected with a viral vector AAV5-CaMKII $\alpha$ -ChR2-mCherry into the MEC. Axis: L, lateral; V, ventral; M, medial; D, dorsal.
- (B) Left upper, ChR2-mCherry expression at the injection site MEC. Left lower, ChR2-mCherry expression in the hippocampus; the boxed area is shown at a higher magnification on the right. Right, fluorescent image reveals the laminated ChR2-mCherry expression in the MML of the DG. DAPI staining defines the area of the GCL. OML: outer one-third of ML.

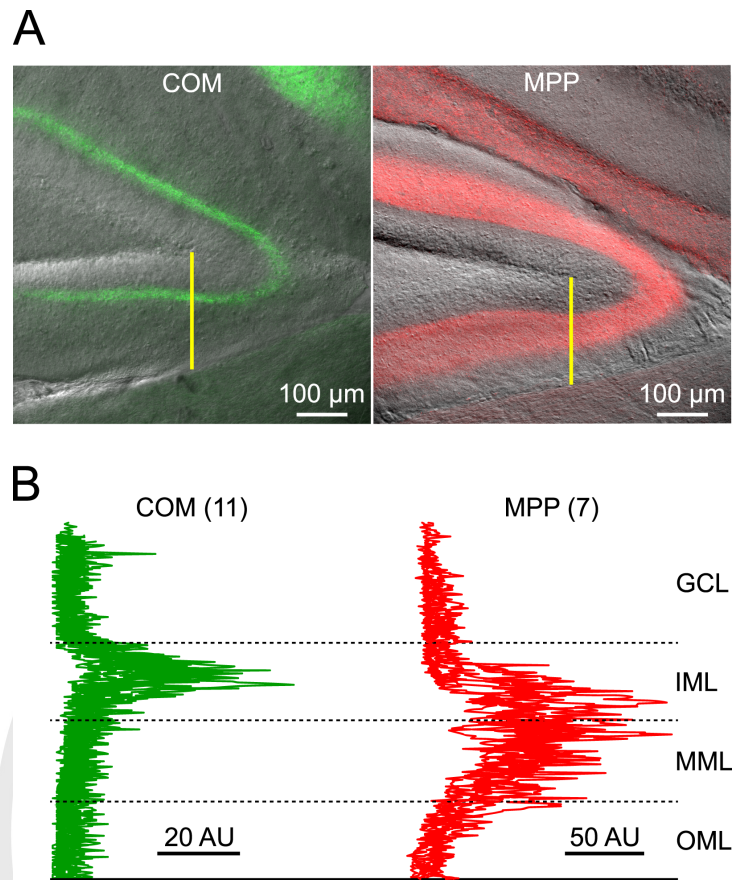


**Figure 7. ChR2 expression in the COM or MPP.**

(A) Analysis of ChR2-eYFP in the COM (green) or ChR2-mCherry (red) in the MPP in fixed slices.

A straight, one-pixel wide yellow line drawn from the crest of GCL/hilus border to the edge of lower blade of molecular layer defined the region of interest in which the fluorescent intensity was quantified.

(B) The fluorescence intensity was plotted against the normalized distance across different layers of the DG. Green and red traces: intensity profiles of selected ROIs. Numbers of analyzed slices are given in parentheses. AU: arbitrary unit, intensity value ranging from min-max is 0 to 255 in 8-bit image.

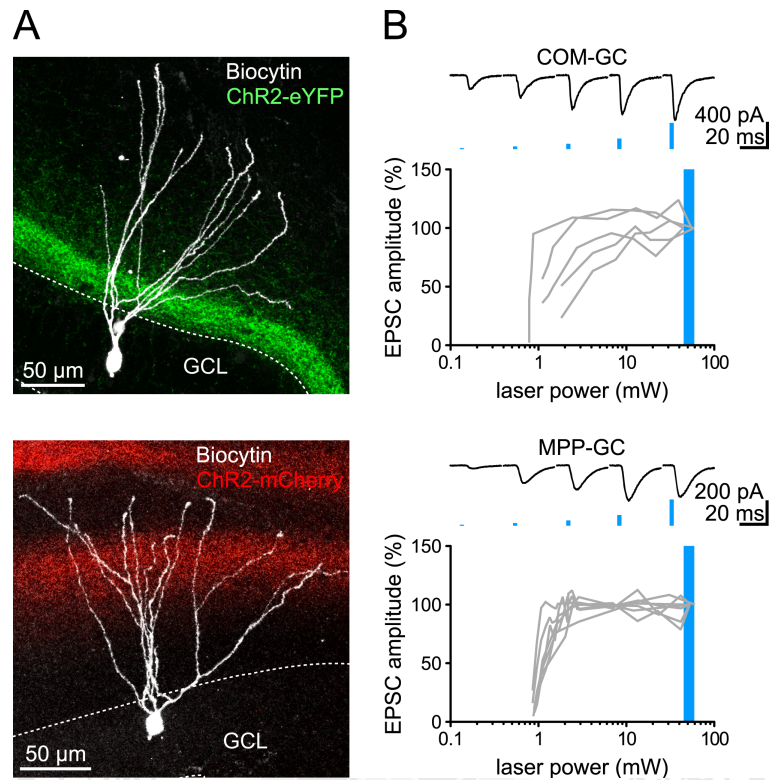


**Figure 8. Input–output relationship of COM– and MPP–GC excitatory synaptic transmission.**

(A) Confocal image stacks show selective ChR2-eYFP (upper, green) and ChR2- mCherry (lower, red) expression in the COM and MPP, respectively. Images were superimposed with biocytin-labeled GCs (white).

(B) Photostimulation of COM (upper) or MPP (lower) with increasing light intensities corresponding to the increments of EPSCs ( $V_{\text{hold}} = -75 \text{ mV}$ ) in GCs. Photostimulation was applied every 15 s. The maximal light intensity in the blue area was used for subsequent experiments. Representative traces of averaged EPSCs evoked by blue light at 5 levels of laser intensity were shown above the input–output curves.

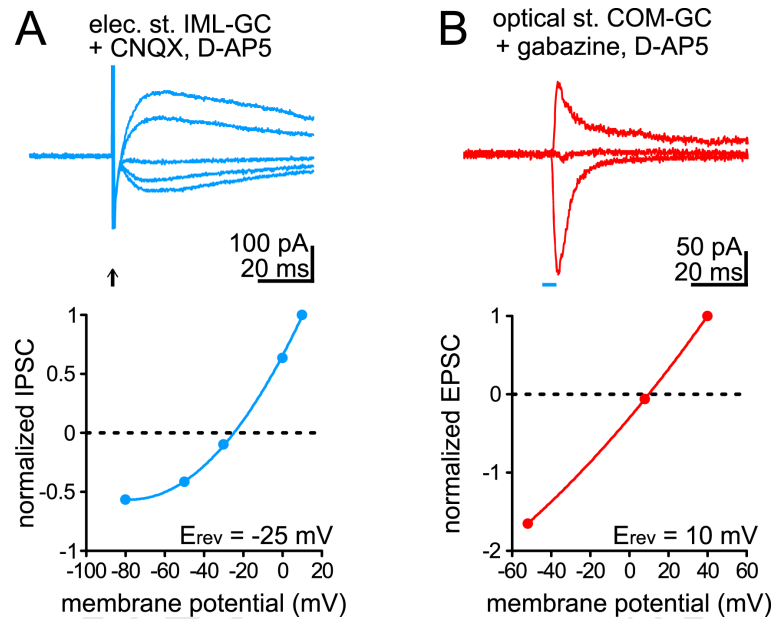


### Figure 9. Reversal potentials of EPSCs and IPSCs.

(A) Electrically evoked IPSCs recorded in the presence of the AMPA receptor antagonist CNQX (10  $\mu\text{M}$ ) and NMDAR antagonist D-AP5 (50  $\mu\text{M}$ ) had a reversal potential near  $-25 \text{ mV}$ .

(B) Optically evoked EPSCs recorded in the presence of the GABA<sub>A</sub> receptor antagonist gabazine (1  $\mu\text{M}$ ) and NMDAR antagonist D-AP5 (50  $\mu\text{M}$ ) had a reversal potential near  $10 \text{ mV}$ . Data points were fitted with second order polynomials.



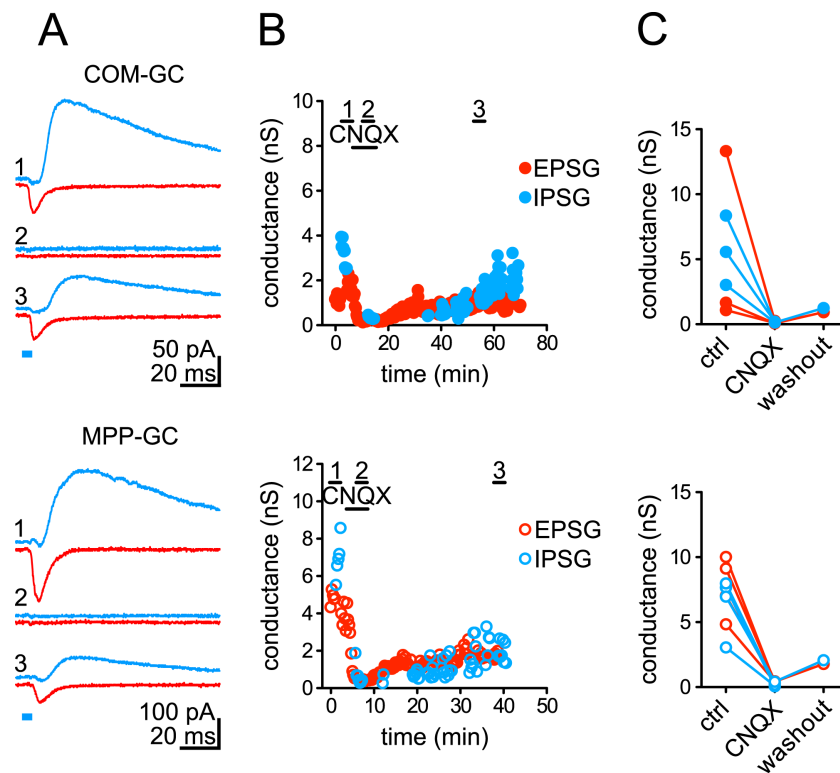


**Figure 10. Light-evoked monosynaptic EPSCs and disynaptic IPSCs.**

(A) Example traces of light-evoked EPSC (red,  $V_{\text{hold}} = -25 \text{ mV}$ ) and IPSC (blue,  $V_{\text{hold}} = 10 \text{ mV}$ ) recorded in a GC in the continuous presence of the NMDAR blocker  $D$ -AP5 ( $50 \mu\text{M}$ ). Photostimulation was applied every 15 s. (1) ACSF; (2) application of the AMPA receptor blocker CNQX ( $10 \mu\text{M}$ ); and (3) washout. Upper: COM-GC synapse. Lower: MPP-GC synapse.

(B) Plots of experiments shown in (A). Application of CNQX and the sample traces shown in (A) are indicated by bars. Upper, COM-GC EPSC: red-filled circles; COM-GC IPSC: blue-filled circles. Lower, MPP-GC EPSC: red open circles; MPP-GC IPSC: blue open circles.

(C) Summary plots of CNQX effect on light-evoked EPSC and IPSC at the COM (upper) or MPP (lower). Symbols are the same as in (B).

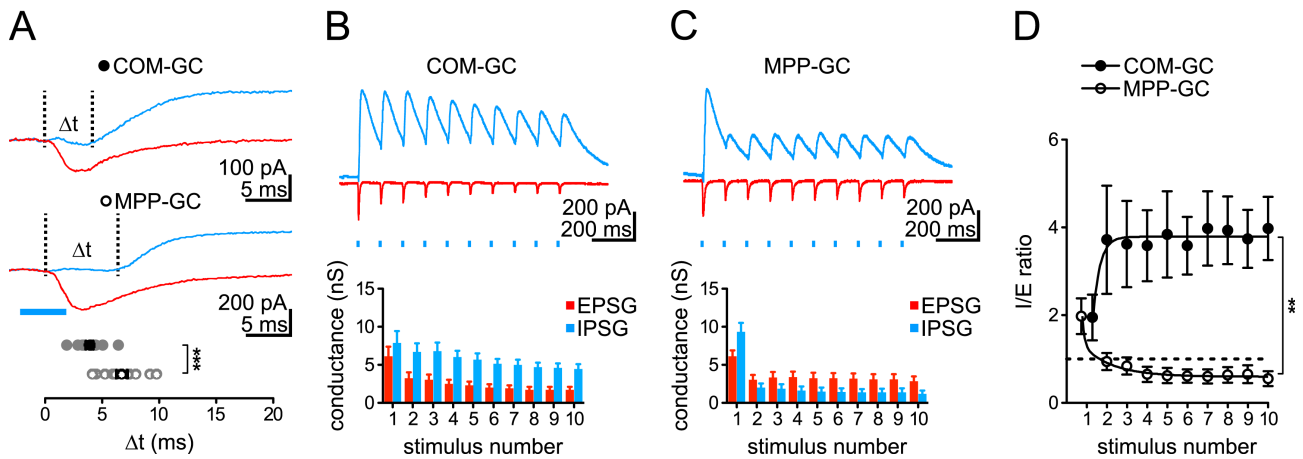


**Figure 11. Distinct I/E ratios at COM-GC and MPP-GC synapses during repetitive stimulation.**

(A) Synaptic delay ( $\Delta t$ ) between the light-evoked IPSC and EPSC at the COM (upper) or MPP (lower). The vertical dashed lines mark the onset of EPSC and IPSC. \*\*\*P < 0.001.

(B,C) Top traces: EPSCs (red,  $V_{\text{hold}} = -25$  mV) and IPSCs (blue,  $V_{\text{hold}} = 10$  mV) evoked by 10 Hz photostimulation of COM (G) or MPP (H). Bottom, summary of EPSCs and IPSCs during theta-frequency photostimulation of COM (B, n = 12) or MPP (C, n = 11). Photostimulation train was applied every 15 s.

(D) Summary of the I/E ratio versus the stimulus number during 10 Hz photostimulation of COM or MPP. Dashed lines, I/E ratio = 1; n = 12 for COM-GC; n = 11 for MPP-GC. \*\*P < 0.01. Data are expressed as mean  $\pm$  SEM.

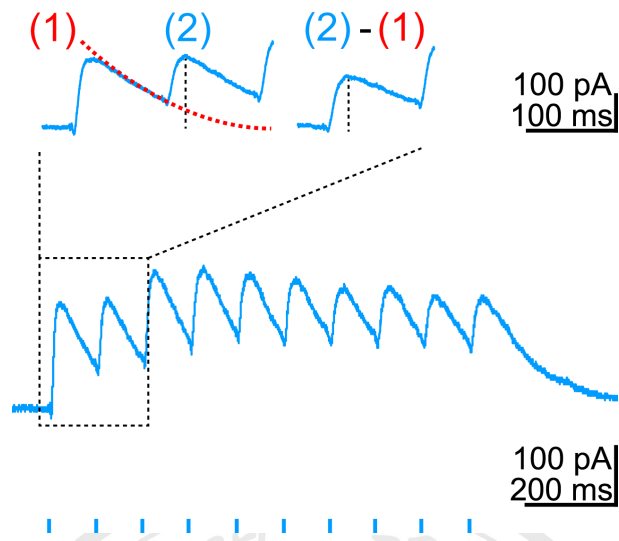


**Figure 12. Calculation of IPSC amplitudes during repeated photo-stimulation.**

The peak amplitude of each IPSC was calibrated by subtracting the decay (red dotted line) of previous IPSC. The red dotted line is the mono-exponential fit of the IPSC decay.

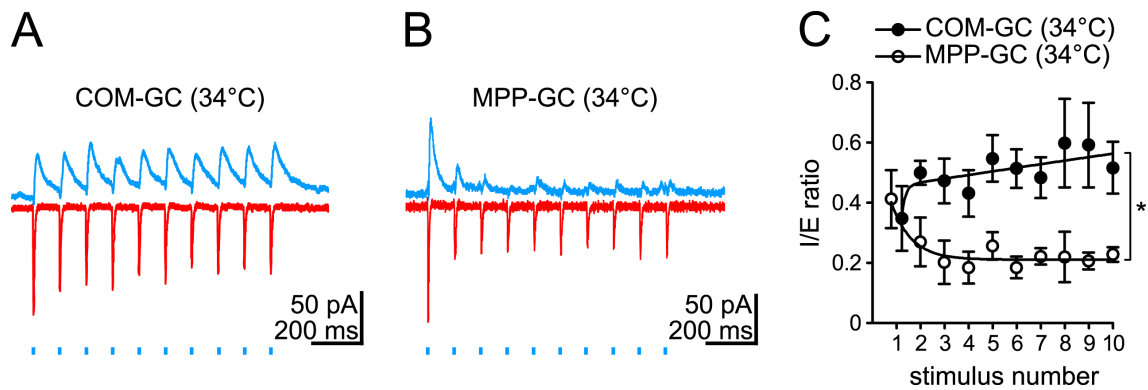


**Figure 13. Distinct I/E ratios at COM-GC and MPP-GC synapses during repetitive stimulation at physiological temperature.**

(A, B) Traces: EPSCs (red,  $V_{\text{hold}} = -30$  mV) and IPSCs (blue,  $V_{\text{hold}} = 12$  mV) evoked by 10 Hz photo-stimulation of COM (A) or MPP (B) at 34 °C. The blue bar indicates the light pulse.

(C) Summary of the I/E ratio versus stimulus number during 10 Hz photo-stimulation of COM (n = 4) or MPP (n = 4) at 34°C. \* $P < 0.05$ . Data are expressed as mean  $\pm$  SEM.

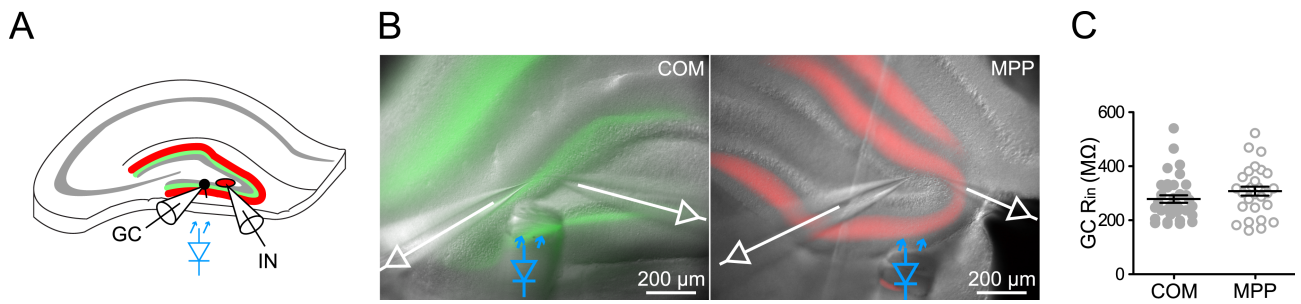


**Figure 14. Experimental configuration for comparison of COM- and MPP-mediated EPSCs Across Various IN Type.**

(A) Schematic diagram depicts the projections of COM (green) and MPP (red) and the area where dual whole-cell recordings were performed.

(B) Dual whole-cell recordings of an IN and a GC during photostimulation of COM (green, left) or MPP (red, right) afferents in coronal hippocampal slices.

(C) Scatter plot of  $R_{in}$  of all recorded GCs.

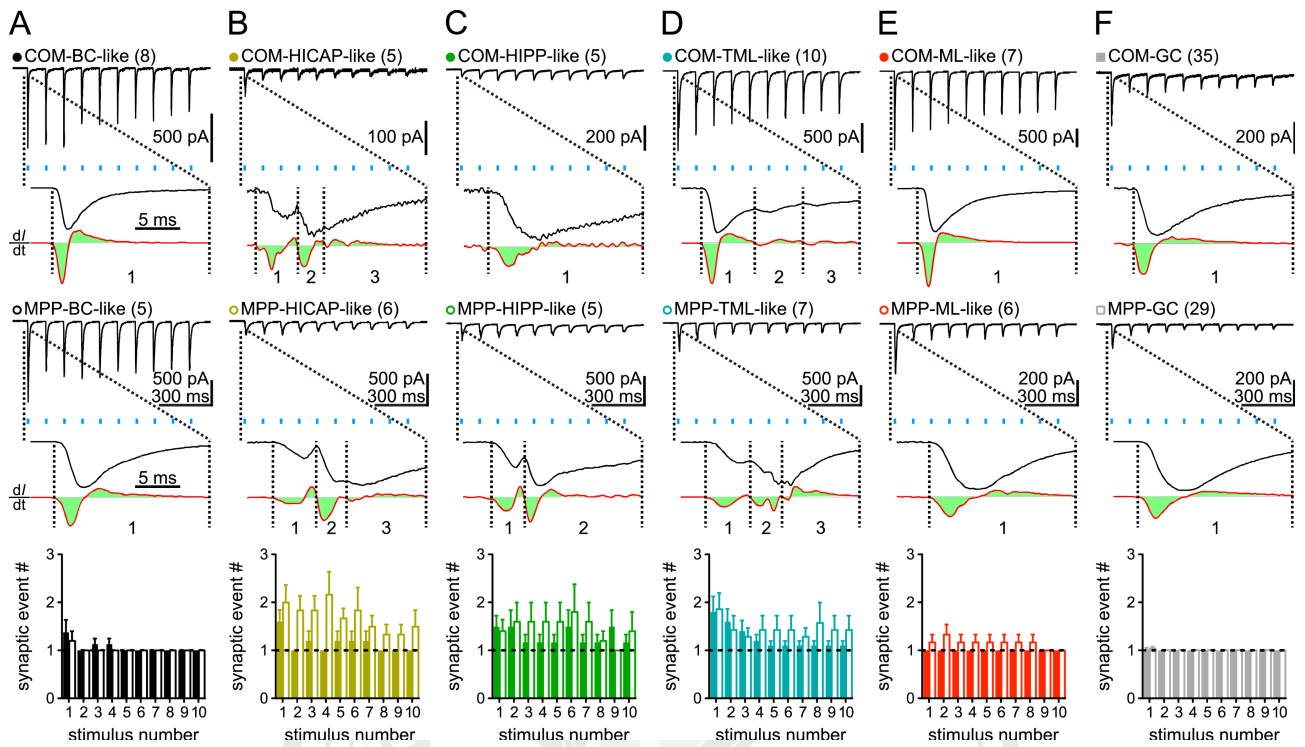


**Figure 15. Synaptic events during photo-stimulation of COM or MPP.**

(A–F) EPSCs evoked by 10 Hz photo-stimulation (blue) of COM and MPP in various IN subtypes and GCs. The EPSC traces following the first light pulse and their corresponding first derivatives (red traces) were shown at higher magnification. Synaptic events were indicated by numbers. Middle and bottom, summary plots of light-evoked EPSC event number across 10 Hz trains (normalized to EPSC<sub>1</sub>) versus stimulus number. Numbers of cells are given in parentheses. Data are expressed as mean  $\pm$  SEM.

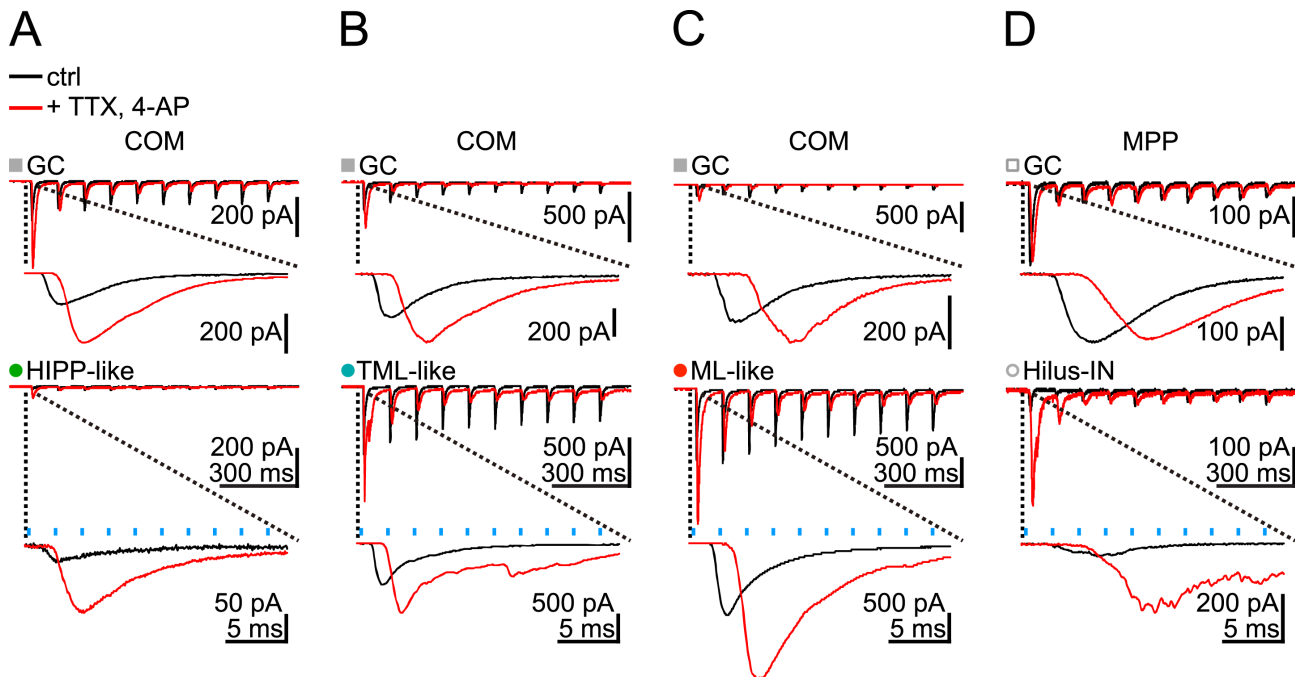


**Figure 16. Comparison of light-evoked EPSCs in GC and IN synapses before and after isolating monosynaptic responses by Na<sup>+</sup> and K<sup>+</sup> channel blockers.**

(A–D) EPSCs evoked by 10 Hz photo-stimulation (blue) of COM and MPP in GCs (top) and simultaneously recorded INs (bottom) before (ctrl, black traces) and after TTX (1  $\mu$ M) and 4-AP (1 mM) application (+TTX, 4-AP, red traces). The EPSC traces following the first light pulse were shown at higher magnification. Notice that the synaptic delays of EPSCs were shorter than those measured in the presence of TTX and 4-AP.

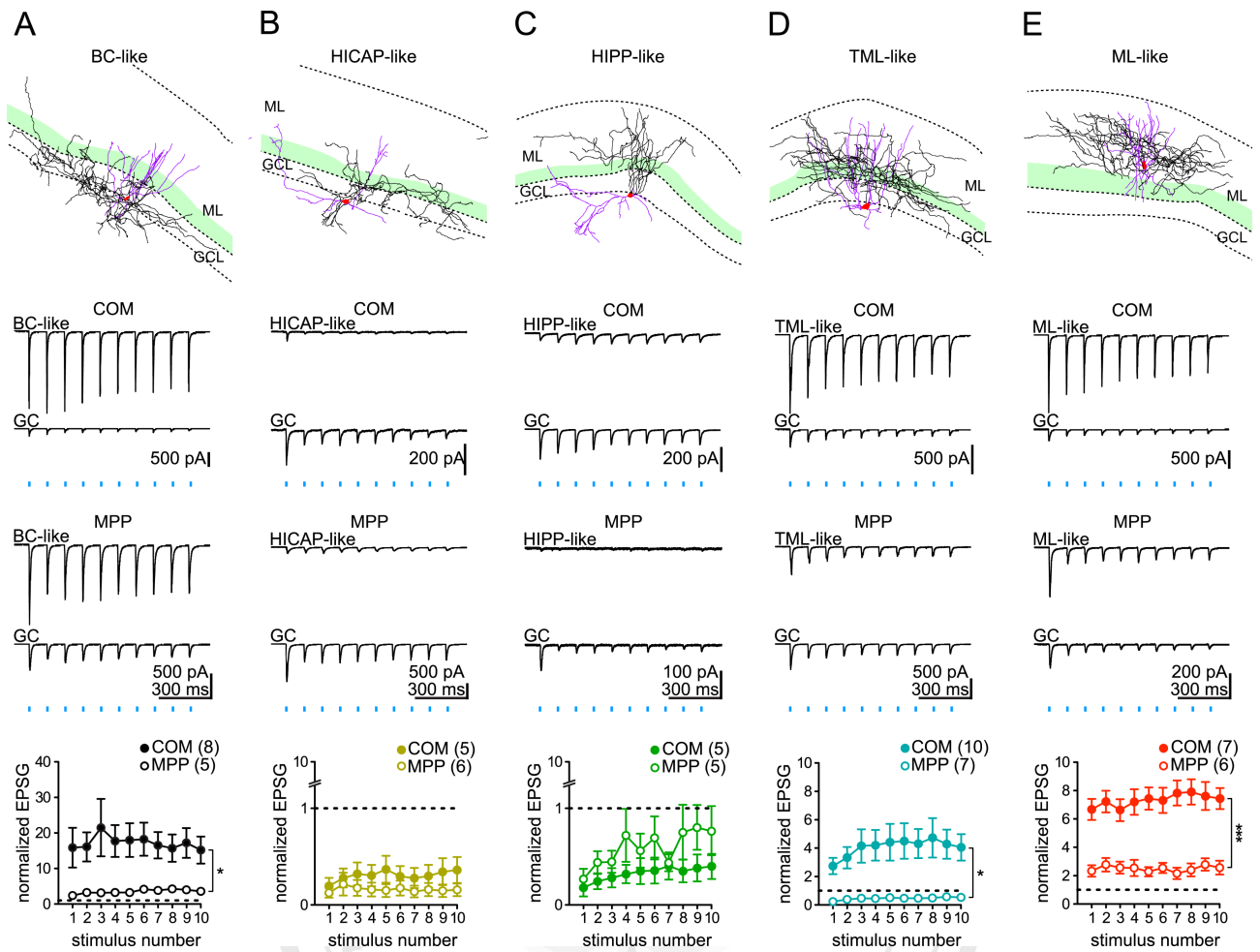


**Figure 17. Target cell-specific synaptic efficacy at COM- and MPP-IN synapses.**

(A–E) Comparison of light-evoked EPSCs between COM- and MPP-IN synapses. Top, exemplar reconstructions of recorded INs. Dendrites, soma, and axons are shown in magenta, red, and black, respectively. The IML (green zone) is outlined according to Chr2-eYFP expression of the same slice. Middle, averaged traces for each dual recording; 10 Hz photostimulation of either COM- (upper) or MPP- (lower) evoked EPSCs in an IN and a GC. EPSCs recorded in GCs are used to normalize the variability of Chr2 expression. Bottom, summary graphs show normalized EPSPs in each type of INs evoked by the COM and MPP. \* $P < 0.05$ ; \*\*\* $P < 0.001$ . Numbers of cells are given in parentheses. Data are expressed as mean  $\pm$  SEM.



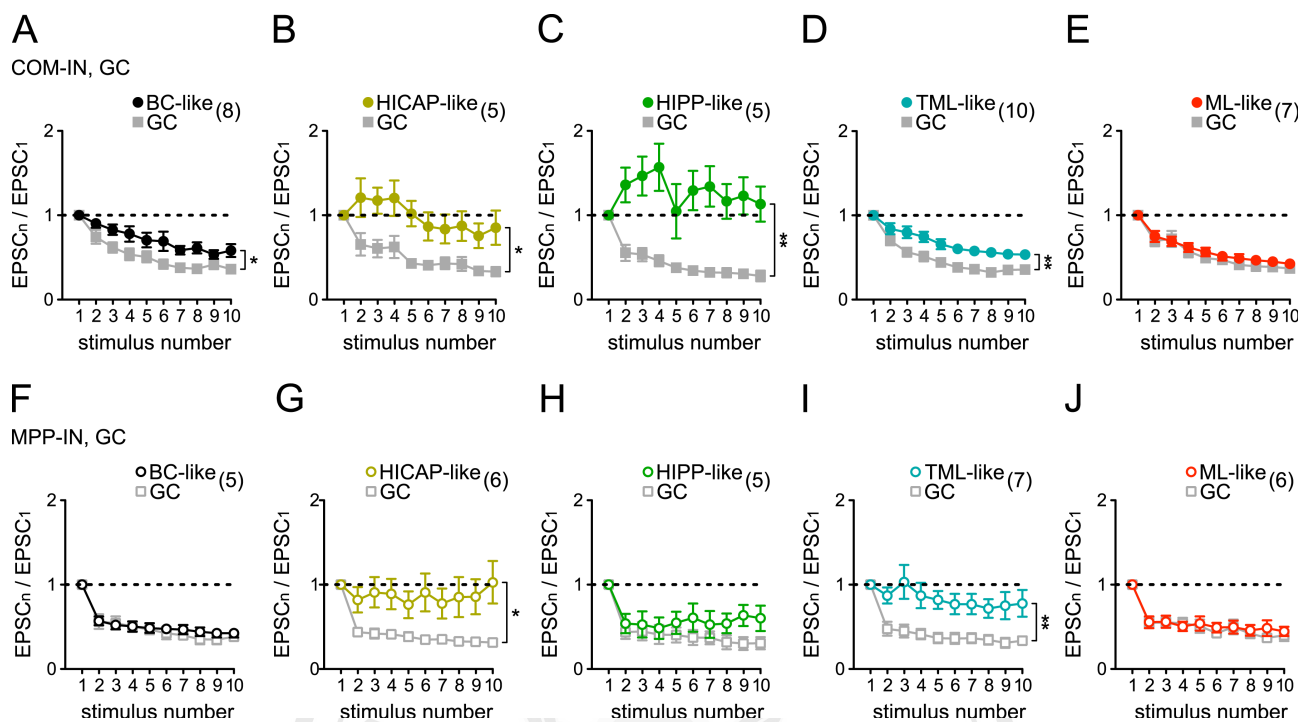


**Figure 18. Comparison of short-term dynamics of EPSCs between INs and simultaneously recorded GCs evoked by COM and MPP 10-Hz train photostimulation.**

(A–E) Summary plots of short-term dynamics of EPSCs in individual IN subtypes and simultaneously recorded GCs across 10-Hz train photo-stimulation of COM (normalized to  $EPSC_1$ ) versus stimulus number.

(F–J) Summary plots of short-term dynamics of EPSCs in each IN subtype and the simultaneously recorded GCs across 10 Hz train photo-stimulation of MPP (normalized to  $EPSC_1$ ) versus stimulus number. \* $P < 0.05$ ; \*\* $P < 0.01$ . Numbers of dual-recording pairs are given in parentheses. Data are expressed as mean  $\pm$  SEM.

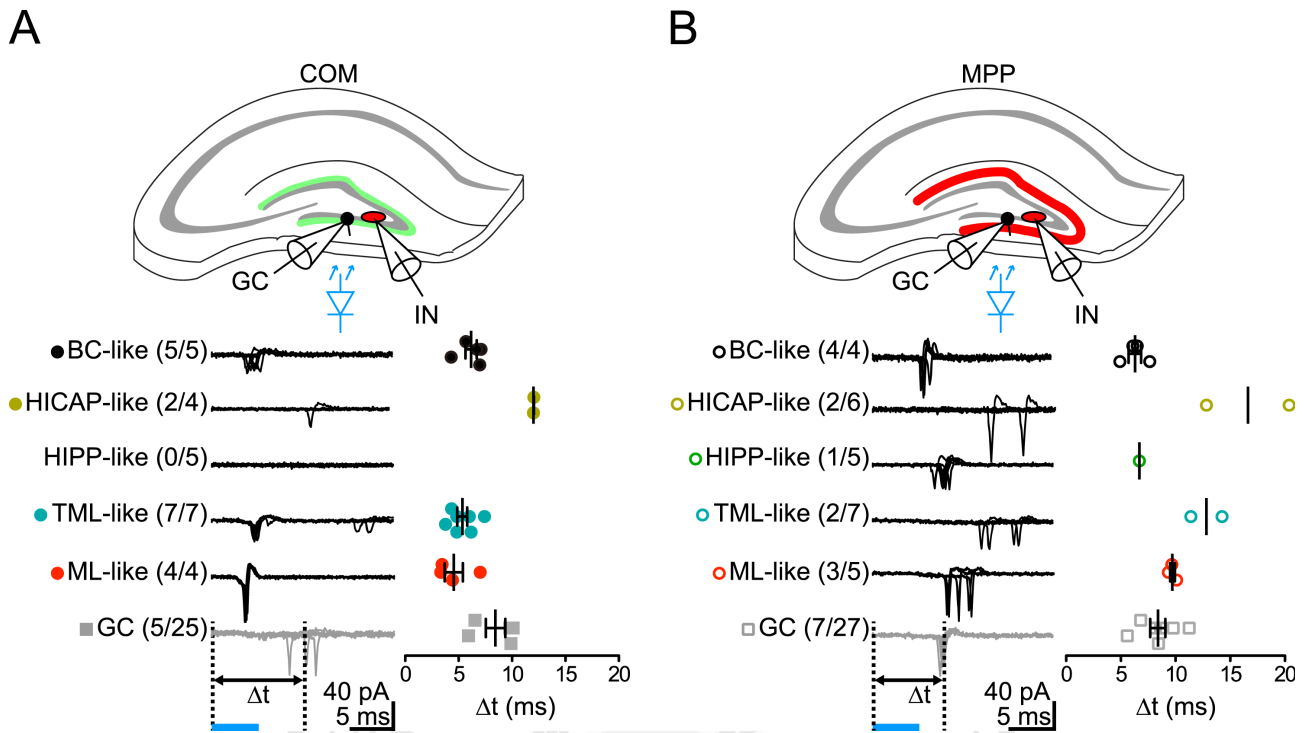


**Figure 19. EPSP-spike coupling in INs and GCs.**

(A,B) Upper, schematic diagram showing photostimulation of either COM (A, green) or MPP (B, red) and recording configurations. Dual recordings were simultaneously made from INs and GCs. Lower, spike delay ( $\Delta t$ ) in response to COM or MPP stimulation (blue bars). Left, example traces indicate extracellular action currents (6 superimposed sweeps) recorded from INs and GCs in the cell-attached, voltage-clamp mode. From top to bottom, traces from morphologically identified BC-, HICAP-, HIPP-, TML-, and ML-like cells and GCs. Right, averaged  $\Delta t$  for the COM (filled circles) and MPP (open circles). Numbers in parentheses represent recruited cell number/total recorded cell number.

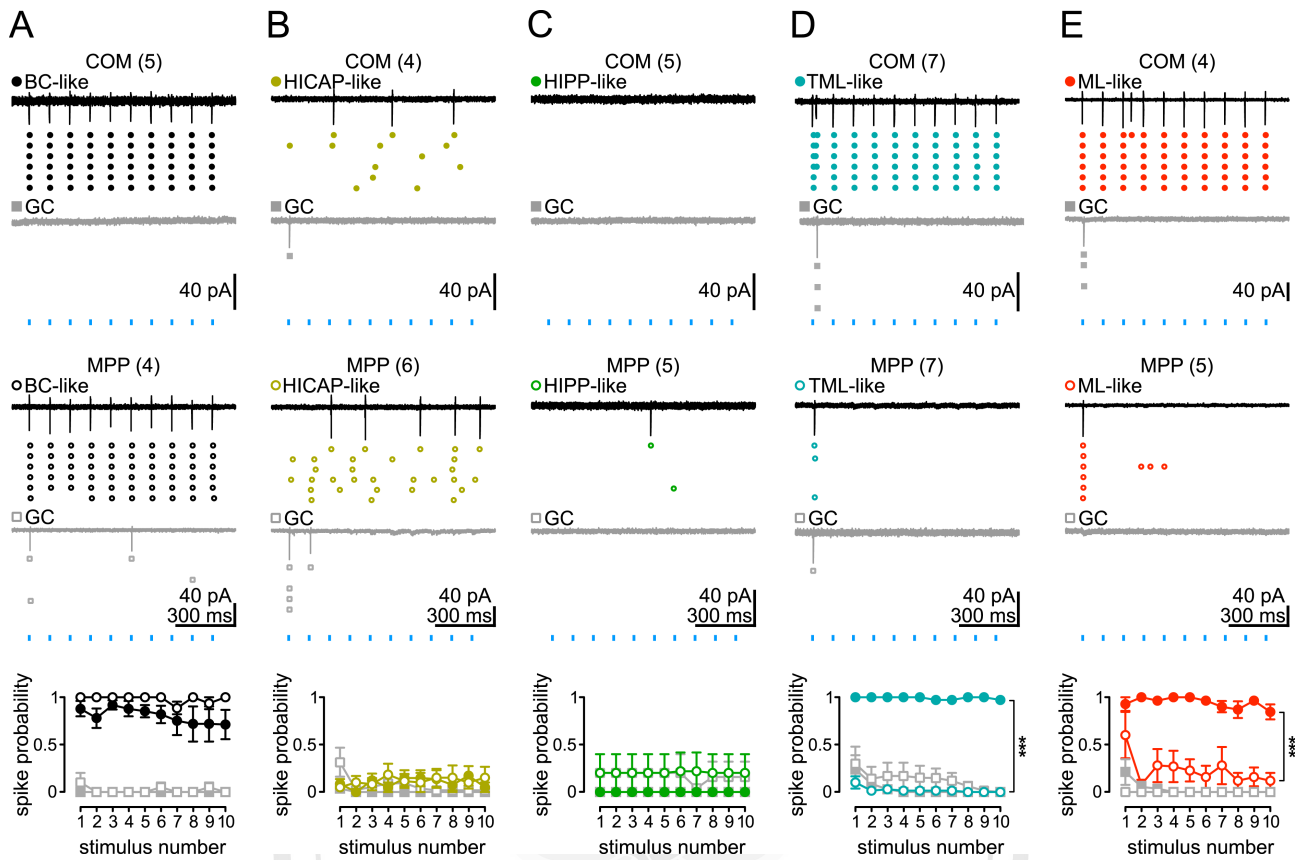


**Figure 20. Differential recruitment of INs by the COM and MPP.**

(A–E) Spike probabilities of INs and GCs in response to 10 Hz photostimulation of COM or MPP.

The light intensity that gave rise to saturated synaptic currents was applied here. Example traces indicate action currents recorded from INs and GCs. Spike raster plots below the traces show firing during 6 trials. Bottom, spike probabilities of INs and GCs. \*\*\* $P < 0.001$ ; numbers of cells are given in parentheses. Data are expressed as mean  $\pm$  SEM.

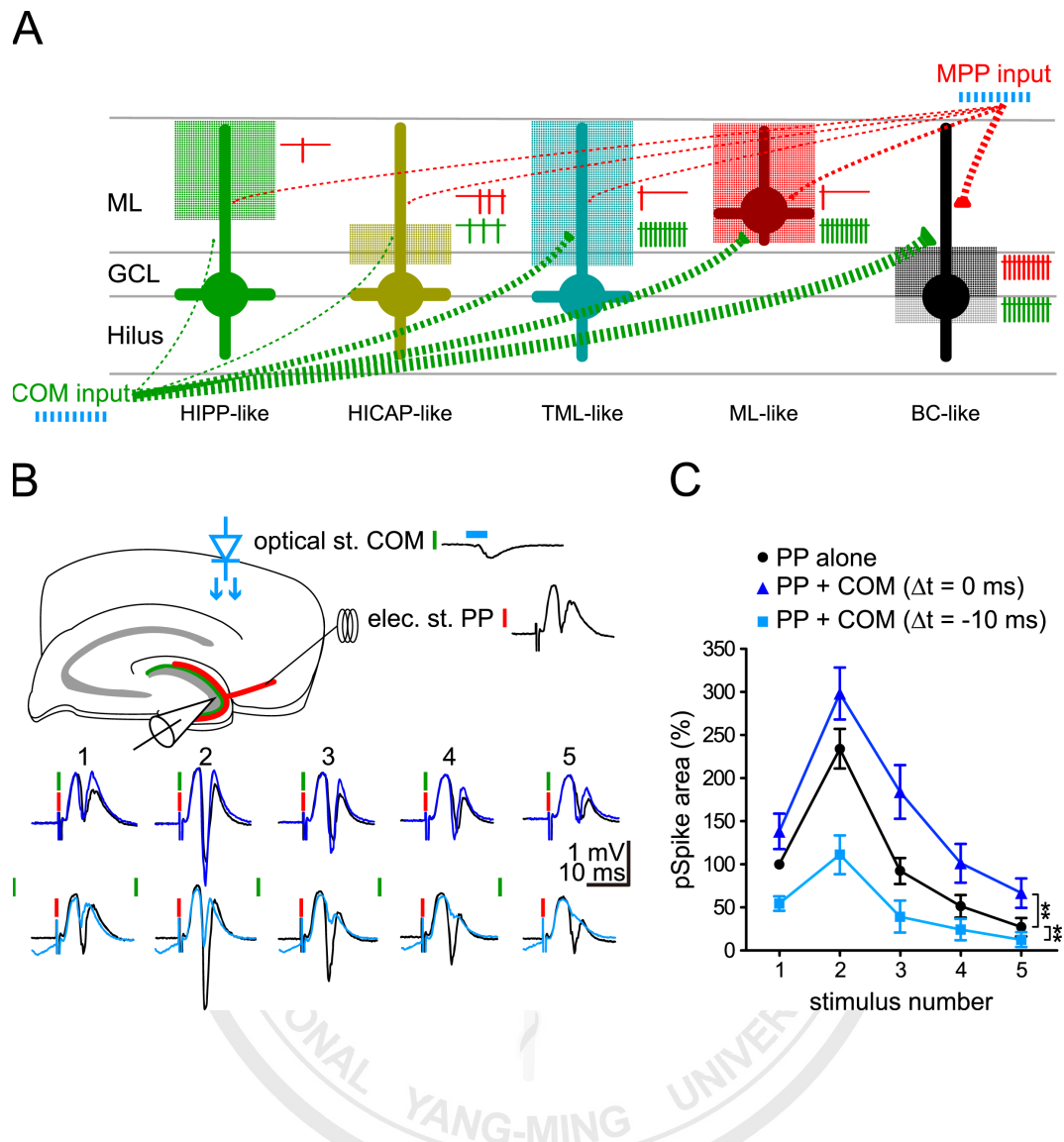


**Figure 21. Summary of COM- and MPP-mediated neurotransmission, IN recruitment, and impact on GC activities.**

(A) Summary diagram of 5 distinct IN classes in the DG based on the morphological classification scheme. Filled circles mark the cell body location. The cell bodies give rise to thick lines indicating the dendritic trees. The hatched boxes are the domains where the axon of each IN primarily arborizes. Green and red dashed lines indicate the COM and MPP projections, respectively. Efficacy of COM- and MPP inputs to different INs types is represented by the

dashed line thickness. Vertical ticks depict spikes in response to 10 Hz photostimulation (blue) of COM or MPP.

(B) Top, schematic of experiment configuration: a field recording electrode was placed in the GCL to monitor pSpikes. A stimulation electrode was placed in the subiculum to activate the PP (red); the axonal fibers of COM (green) expressing ChR2 were stimulated with blue light. Each vertical bar represents a single-stimulating pulse. Bottom, pSpike responses to the PP and COM stimulation. Black traces, PP stimulation alone. Blue traces, simultaneous activation of PP and COM ( $\Delta t = 0$  ms). Light blue traces, COM stimulation was delivered 10 ms before PP stimulation ( $\Delta t = -10$  ms).

(C) Summary of effect of COM activation on pSpike area, which reflects the number of GCs that spike synchronously to PP stimulation. The magnitude of pSpike area (normalized to the first pSpike area to PP alone) was plotted against the stimulation number. PP stimulation alone (PP alone) represents average from 10 recordings, and data points in the other 2 data sets represent average from 5 recordings.  $**P < 0.01$ . Data are expressed as mean  $\pm$  SEM.

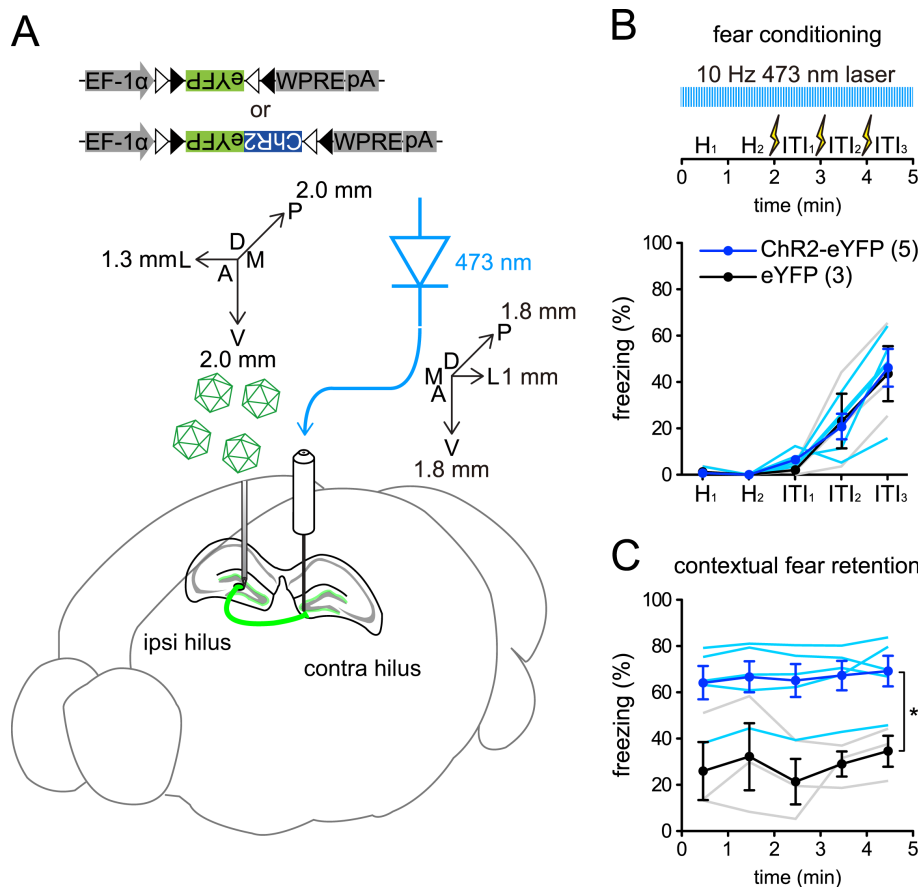


**Figure 22. Enhancement of contextual fear memory by COM activation.**

(A) Schematic diagram illustrates *Grik4-cre* mouse injected unilaterally with a viral vector AAV5-EF1 $\alpha$ -DIO-ChR2-eYFP or AAV5-EF1 $\alpha$ -eYFP into the hilar region of the dorsal hippocampus. An optical fiber was implanted into the contralateral DG for subsequent photostimulation (473 nm) of COM. Axis: L, lateral; V, ventral; M, medial; D, dorsal; A, anterior; P, posterior.

(B) Top, Experimental protocol of contextural fear conditioning on day 1. The light pulse (10-Hz stimulation train, 5 ms light pulse, 10 mW power measured from the fiber tip) was delivered through the optic fiber during the entire conditioning period. H: habituation session. ITI: inter-trial interval. Bottom, Plot of relative time spent in freezing versus the trial of fear conditioning.

ChR2-eYFP group: light blue line for individual data, blue line and circles for averaged data. eYFP group: gray line for individual data, black line and circles for averaged data. Number of experiments are given in parentheses. Data are expressed as mean  $\pm$  SEM.

(C) Plot of relative time spent in freezing versus the time during contextual fear retention test. Symbols and number of experiments are the same as in (B). \* $P < 0.05$ . Data are expressed as mean  $\pm$  SEM.



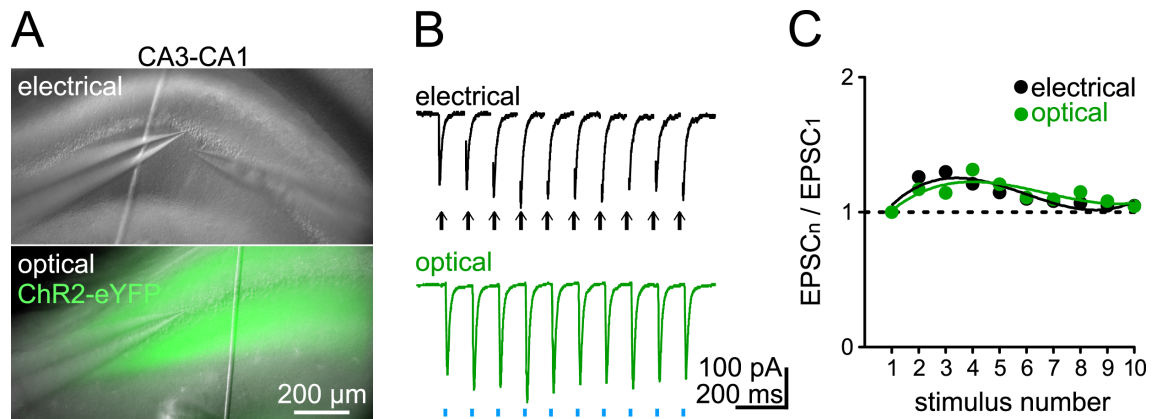


**Figure 23. Comparison of AAV5-ChR2 activation and electrical stimulation at CA3–CA1 synapses.**

(A) Upper, electrical stimulation of Schaffer collateral axons and recording of EPSCs from a CA1 pyramidal cell. Left pipette, recording electrode; right pipette, stimulation electrode. Lower, ChR2 expression in Schaffer collateral axons and recording of optically evoked EPSCs from a CA1 pyramidal cell.

(B) Example traces of electrically (upper) and optically (lower) evoked EPSCs.

(C) Plot of normalized EPSC amplitude versus stimulus number.



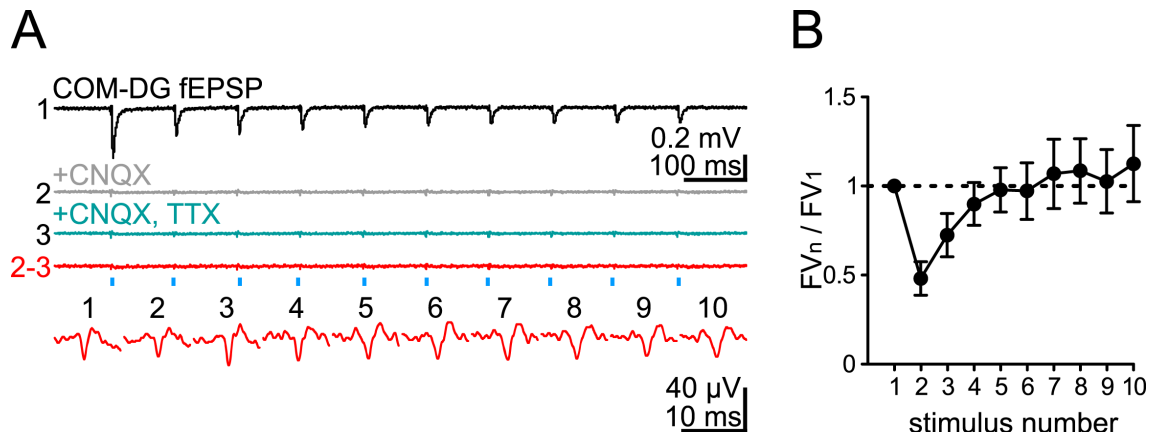


**Figure 24. Recording of COM-evoked fiber volley.**

(A) Example traces of light-evoked field EPSPs (fEPSPs, black; trace 1), after addition of CNQX (10  $\mu$ M, gray; trace 2) and after addition of CNQX (10  $\mu$ M) and TTX (1  $\mu$ M, cyan; trace 3), and subtracted trace (red; trace 2-3). Bottom trace, the TTX-sensitive fiber volleys (FVs), the enlargement of subtracted trace (red).

(B) Plot of normalized FV versus stimulus number.

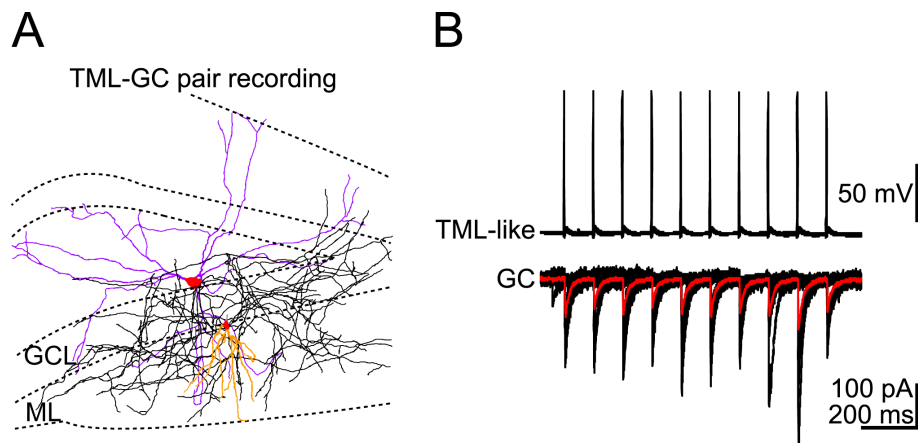


**Figure 25. TML-like IN output to GCs.**

- (A) An exemplar reconstruction of the recorded TML-like IN, in which dendrites, soma, and axons are shown in magenta, red, and black, respectively. The paired GC is shown, in which dendrites, soma, and axons are shown in orange, red and gray, respectively.
- (B) Paired recording from a TML-like IN-to-GC pair. Ten action potentials were evoked in the TML-like IN by injection of brief current pulses (2 ms, 10 Hz) every 20 s. Presynaptic INs were current clamped at  $-60$  mV, whereas postsynaptic GCs were voltage clamped at  $-80$  mV.

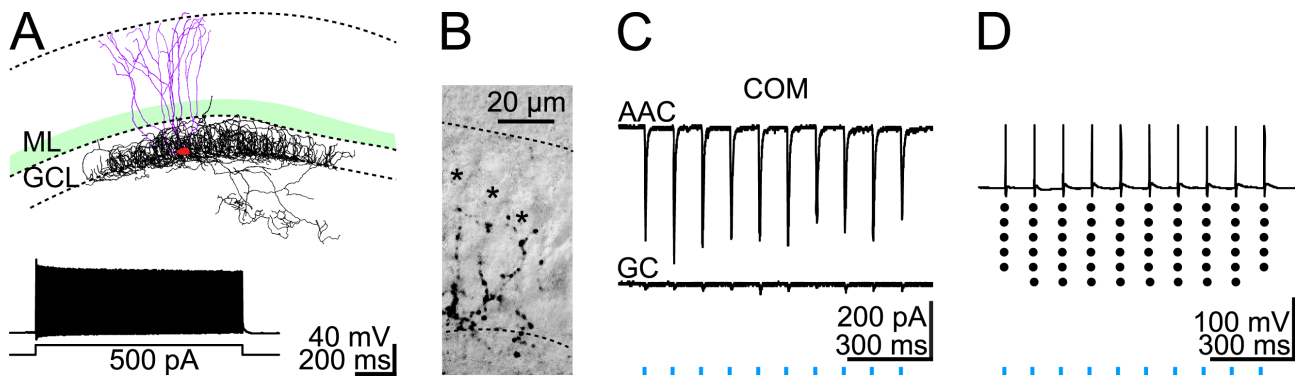


**Figure 26. Reconstruction of an AAC-like cell.**

- (A) Reconstruction of a biocytin-labeled AAC-like cell in the DG. The axon (black) of the labeled cell is mainly found in the GCL and the border between the GCL and hilus, where axon initial segments of GCs are localized.
- (B) High-power photomicrograph (an IR-DIC image and a single two-photon image are superimposed) shows axo-axonic cartridges (black) of the labeled AAC-like cell along the axon initial segment of three unstained GCs. Asterisks mark GC somata.
- (C) Upper, averaged traces from dual recording of an AAC-like cell and a GC; 10 Hz photostimulation of COM evoked EPSCs in the AAC-like cell and a GC.
- (D) Action potentials evoked in the AAC in response to 10 Hz photo-stimulation of COM. Spike raster plots below the traces show firing during six trials.

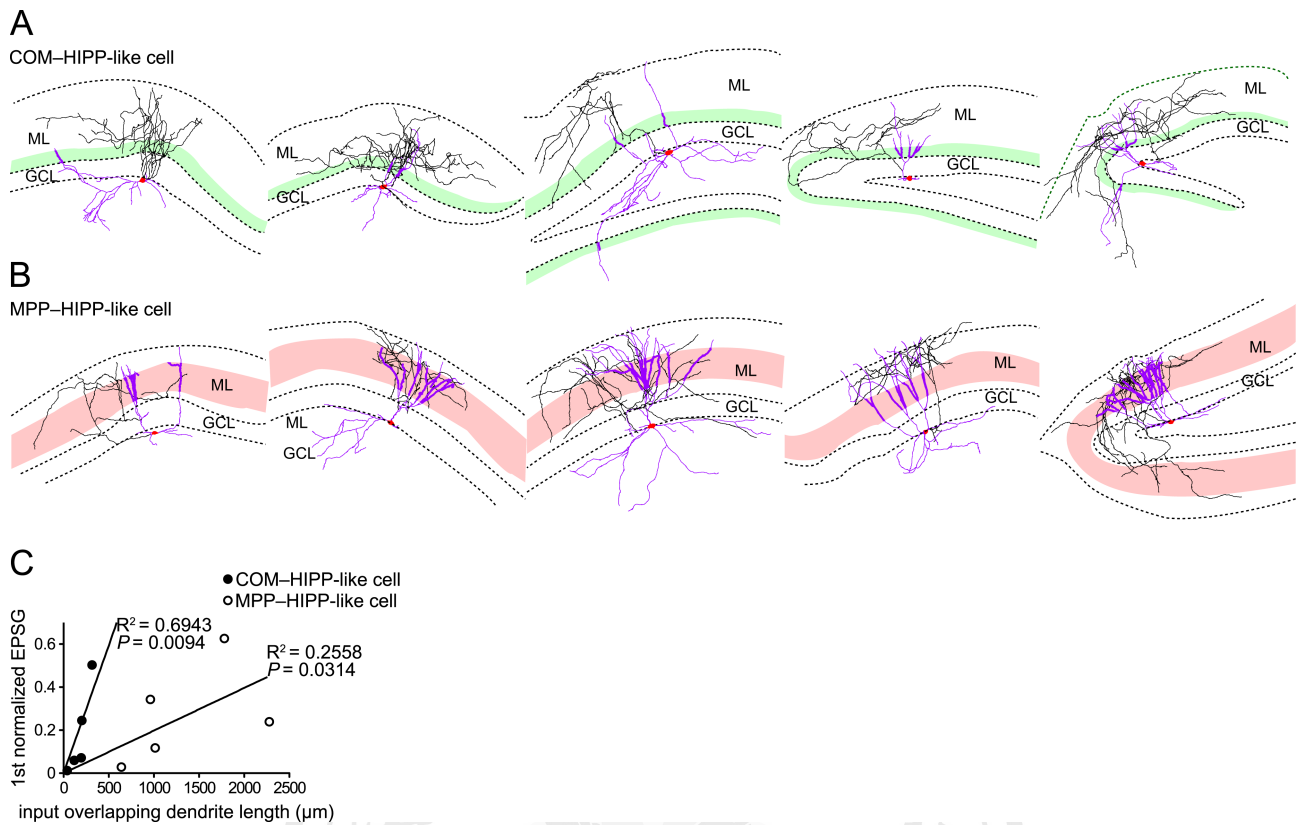


**Figure 27. Variability of HIPP cells and synaptic input efficacy.**

(A) Exemplar reconstructions of HIPP cells in COM-targeting slices. Dendrites, soma, and axons are shown in magenta, red, and black, respectively. The IML (green zone) is outlined according to ChR2-eYFP expression of the same slice.

(B) Exemplar reconstructions of HIPP cells in MPP-targeting slices. Dendrites, soma, and axons are shown in magenta, red, and black, respectively. The MML (red zone) is outlined according to ChR2-mCherry expression of the same slice.

(C) Plot of the first normalized EPSC in HIPP cells (normalized to GCs) versus dendrite length within the IML (green zone) or the MML (red zone). 10 Hz photostimulation of either COM (filled circles) or MPP (open circles) evoked EPSCs in an HIPP and a GC (see Figure 13).

**Table 1. Properties of EPSC and IPSC in GCs**

Input	Synaptic delay <sup>a</sup> (ms)	20–80% Rise time (ms)	Decay time constant (ms)
EPSC			
COM (13)	2.9 ± 0.1	1.0 ± 0.1	4.6 ± 0.1
MPP (12)	3.9 ± 0.2	1.8 ± 0.1	5.9 ± 0.4
IPSC			
COM (13)	6.8 ± 0.3	5.3 ± 0.2	96.7 ± 5.9
MPP (12)	10.6 ± 0.5	5.7 ± 0.5	92.8 ± 7.3

Note: Numbers of cells are given in parentheses.

<sup>a</sup> Synaptic delay was calculated as the time elapsed from the onset of photo-stimulation to the onset of first EPSC or IPSC.

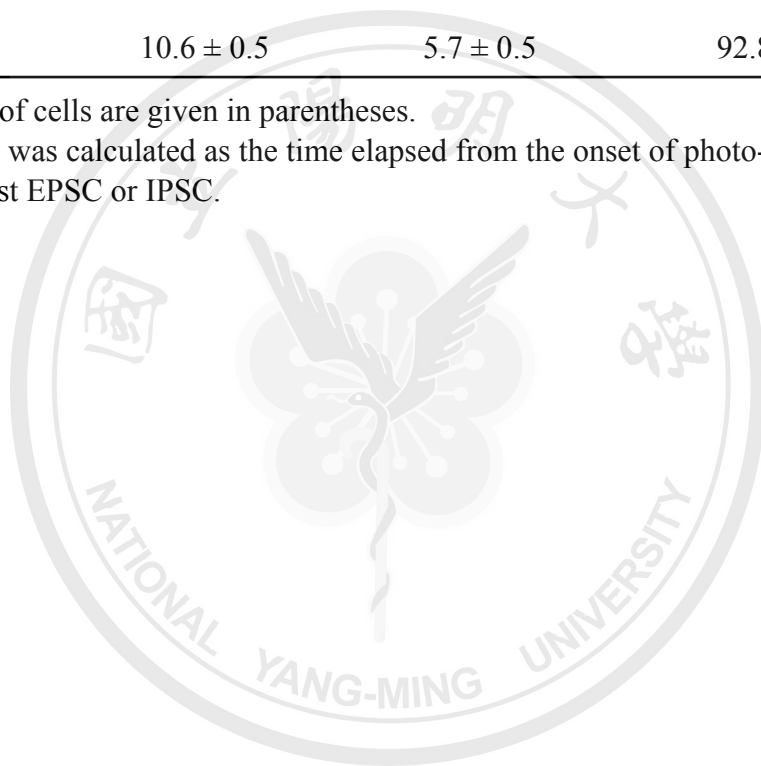


**Table 2. Properties of EPSC in DG INs**

Input	Synaptic delay <sup>a</sup> (ms)	20–80% Rise time <sup>b</sup> (ms)	Decay time constant <sup>c</sup> (ms)	Normalized conductance <sup>d</sup>
BC-like				
COM (8)	2.6 ± 0.1	0.4 ± 0.0	2.6 ± 0.3	14.8 ± 5.1
MPP (5)	4.3 ± 0.4	1.2 ± 0.2	5.5 ± 0.7	2.5 ± 0.6
HICAP-like				
COM (5)	2.9 ± 0.2	1.3 ± 0.3	6.7 ± 0.8	0.2 ± 0.1
MPP (6)	4.5 ± 1.1	1.8 ± 0.5	11.6 ± 0.8	0.1 ± 0.0
HIPP-like				
COM (5)	3.2 ± 0.2	1.0 ± 0.3	7.5 ± 1.6	0.2 ± 0.1
MPP (5)	5.2 ± 0.6	1.8 ± 0.3	8.9 ± 1.1	0.3 ± 0.1
TML-like				
COM (10)	2.9 ± 0.1	0.8 ± 0.1	6.9 ± 0.6	2.7 ± 0.6
MPP (7)	5.4 ± 1.3	1.8 ± 0.3	9.2 ± 1.8	0.3 ± 0.1
ML-like				
COM (7)	3.1 ± 0.2	0.8 ± 0.1	4.6 ± 0.4	6.6 ± 0.7
MPP (6)	4.1 ± 0.3	1.5 ± 0.1	6.6 ± 0.9	2.1 ± 0.4
GC				
COM (35)	3.1 ± 0.1	1.1 ± 0.1	5.7 ± 0.1	1.0 ± 0.0
MPP (29)	4.4 ± 0.2	2.1 ± 0.1	6.9 ± 0.2	1.0 ± 0.0

Note: Numbers of cells are given in parentheses.

<sup>a</sup> Synaptic delay was calculated as the time elapsed from the onset of photo-stimulation to the onset of first monosynaptic EPSC.

<sup>b</sup> 20–80% rise time was measured from the first monosynaptic EPSC.

<sup>c</sup> Decay time constant was measured from the synaptic events that only contain monosynaptic EPSCs.

<sup>d</sup> First monosynaptic EPSC of IN was normalized to that of GC.

## Curriculum Vitae

許璨庭 Hsu, Tsan-Ting

Phone: +886-919-190-827

e-mail: [tsanting@gmail.com](mailto:tsanting@gmail.com)

Address: 2F, No. 203, Sec. 2, Shuiyuan St. Tamsui Dist., New Taipei City 25149, Taiwan (R.O.C.)

---

### EDUCATION

2006 ~ 2015 **Ph.D. in Neuroscience.** Transfer from Master's to Doctoral Program without Completing Master's Requirements. Institute of Neuroscience, National Yang-Ming University, Taipei, Taiwan

2002 ~ 2006 **B.S. in Biology.** Department of Biology, National Changhua University of Education, Changhua, Taiwan

---

### RESEARCH INTERESTS

Functional connectome, Psychobiology, Gene therapy for neural disorder, Neuron-glia interaction

---

### PUBLICATIONS

**Hsu TT**, Lee CT, Tai MH, Lien CC. (2015) Differential recruitment of dentate gyrus interneuron types by commissural versus perforant pathways. *Cerebral Cortex* [Epub ahead of print].

Wu PY, Huang YY, Chen CC, **Hsu TT\***, Lin YC, Weng JY, Chien TC, Cheng IH, Lien CC. (2013) Acid-sensing ion channel-1a is not required for normal hippocampal LTP and spatial memory. *Journal of Neuroscience*. 33: 1828-1832. (\* First co-author)

Chu KC, Chiu CD, **Hsu TT**, Hsieh YM, Huang YY, Lien CC. (2010) Functional identification of an outwardly rectifying pH- and anesthetic-sensitive leak K<sup>+</sup> conductance in hippocampal astrocytes. *European Journal of Neuroscience*. 32: 725-735.

Weng JY, **Hsu TT**, Sun SH. (2008) Functional characterization of P2Y<sub>1</sub> versus P2X receptors in RBA-2 astrocytes: elucidate the roles of ATP release and protein kinase C. *Journal of Cellular Biochemistry*. 104:554-567

---

### CONFERENCE PRESENTATIONS

**Hsu TT**, Tai MH, Lien CC. (2014) Afferent-specific recruitment of interneurons in the dorsal hippocampal dentate gyrus. Poster session presented at the *44th Annual meeting of the Society for Neuroscience*, Washington, DC, USA

**Hsu TT**, Tai MH, Lien CC. (2012) Optogenetic control of neuronal activity in brain circuits. Poster session presented at the *2012 Annual Thesis Competition of National Yang-Ming University*.

**Hsu TT**, Lien CC. (2011) Control of neuronal firing by light. Poster session presented at the *2011 Annual Thesis Competition of National Yang-Ming University*.

**Hsu TT**, Weng JY, Sun SH (2007) Coactivation of P2Y<sub>1</sub> and P2X receptors is essential for Ca<sup>2+</sup> sustain in astrocytes: elucidate the role of protein kinase C and the involvement of endogenous ATP release. Poster session presented at the *37th Annual meeting of the Society for Neuroscience*, San Diego, CA, USA

---

### HONOR & AWARDS

Outstanding Award at the *2012 Annual Thesis Competition of National Yang-Ming University*

---

### PROFESSIONAL MEMBERSHIP

Student Member of the Society for Neuroscience (2007 ~ 2008, 2014 ~ Now)